

**PREPARATION OF POLYPYRROLE
NANOCOMPOSITES FOR HIGH-PERFORMANCE
SUPERCAPACITOR ELECTRODES**

JOHN KEVIN GAN ZI YI

**THESIS SUBMITTED IN FULFILLMENT OF THE
REQUIREMENTS FOR THE DEGREE OF
DOCTOR OF PHILOSOPHY**

**FACULTY OF SCIENCE
UNIVERSITY OF MALAYA
KUALA LUMPUR**

2016

UNIVERSITI MALAYA

ORIGINAL LITERARY WORK DECLARATION

Name of Candidate: **JOHN KEVIN GAN ZI YI**

Registration/Matric No: **SHC 120098**

Name of Degree: **DOCTOR OF PHILOSOPHY**

Title of ~~Project Paper/Research Report/Dissertation~~/Thesis (“this Work”):

PREPARATION OF POLYPYRROLE NANOCOMPOSITES FOR HIGH-PERFORMANCE SUPERCAPACITOR ELECTRODES

Field of Study: **EXPERIMENTAL PHYSICS**

I do solemnly and sincerely declare that:

- (1) I am the sole author/writer of this Work;
- (2) This Work is original;
- (3) Any use of any work in which copyright exists was done by way of fair dealing and for permitted purposes and any excerpt or extract from, or reference to or reproduction of any copyright work has been disclosed expressly and sufficiently and the title of the Work and its authorship have been acknowledged in this Work;
- (4) I do not have any actual knowledge nor do I ought reasonably to know that the making of this work constitutes an infringement of any copyright work;
- (5) I hereby assign all and every rights in the copyright to this Work to the University of Malaya (“UM”), who henceforth shall be owner of the copyright in this Work and that any reproduction or use in any form or by any means whatsoever is prohibited without the written consent of UM having been first had and obtained;
- (6) I am fully aware that if in the course of making this Work I have infringed any copyright whether intentionally or otherwise, I may be subject to legal action or any other action as may be determined by UM.

Candidate’s Signature:

Date:

Subscribed and solemnly declared before,

Witness’s Signature:

Date:

Name: **Dr. Huang Nay Ming**

Designation: **Senior Lecturer**

ABSTRACT

Electrode material is of great importance for the realization of high-performance supercapacitors. Hence, improving the electrochemical aspects of the electroactive materials will inevitably enhance the performance of supercapacitors. This work aims to harness the properties of interest of polypyrrole (PPy) through the synthesis of PPy-based nanocomposites. This research work was divided into four stages. The first study involves the synthesis and evaluation of the capacitance performance of polypyrrole/manganese oxide (PPy/MnO₂) nanocomposites. PPy/MnO₂ nanocomposites with compact sheet, fibrous-porous and granular morphologies were synthesized by simply tuning the pH of the solution. The optimum pH condition was found to be 4.0, producing highly porous PPy/MnO₂ nanocomposite that enabled the rapid intercalation/deintercalation of the electrolyte. As a result, a specific capacitance of up to 306 F g⁻¹ was obtained for the porous PPy/MnO₂ nanocomposite. The second part of this work was to improve the electrode wettability of the PPy electrode by the integration of chitosan biopolymer. The newly obtained hydrophilic properties of the polypyrrole/chitosan (PPy/CS) nanocomposites elicited an improvement in its specific capacitance. Hence, the nanocomposite PPy/CS displayed a specific capacitance of 403 F g⁻¹ as opposed to 273 F g⁻¹ for the pure PPy electrode calculated at 0.2 A g⁻¹. Contact angle measurement indicated an improvement in the hydrophilicity of PPy/CS nanocomposites. The increased surface wettability of the nanocomposite electrode effectively increased the ion-accessible surface and facilitated the electrolyte infiltration throughout the internal volume of the electrode. The third part of this work was to enhance the electronic conductivity of PPy with the incorporation of silver (Ag) particles. A hybrid silver nanoparticle/nanocluster-decorated polypyrrole demonstrated an enhanced specific capacitance of 414 F g⁻¹. The enhanced specific capacitance was mainly attributed to the unique architecture and hybrid nanostructures of Ag. The Ag

nanoparticles enhanced the electron hopping system of the PPy, effectively increasing the supercapacitive properties of the PPy. On the other hand, the Ag nanoclusters acted as spacers to prevent the restacking of PPy films, further extending the active sites for redox reactions, leading to improved specific capacitance. The final part of this study sought to combine the merits of the hydrophilic chitosan and highly conducting Ag with PPy. Experimental results showed that the ternary nanocomposite (Ag@PPy/CS) has a specific capacitance of 513 F g^{-1} at 0.2 A g^{-1} . The improved transportation of electrolyte ions and electrons by the incorporation of chitosan and Ag led to a pronounced enhancement in the supercapacitive property of PPy.

University of Malaysia

ABSTRAK

Bahan elektrod adalah amat mustahak untuk merealisasikan superkapasitor berprestasi tinggi. Justeru itu, peningkatan dalam aspek elektrokimia bagi bahan elektroaktif secara langsung akan meningkatkan prestasi superkapasitor. Kajian ini bertujuan untuk menggunakan ciri-ciri menarik polypyrrole (PPy) melalui penyediaan nanokomposit berasaskan PPy. Penyelidikan ini dibahagikan kepada empat peringkat. Kajian pertama melibatkan sintesis dan penilaian prestasi kapasitan daripada nanokomposit polypyrrole/mangan oksida (PPy/MnO₂). Nanokomposit PPy/MnO₂ dengan morfologi yang padat, berliang dan bergranul telah disintesis dengan pengubahsuaian nilai pH larutan. Didapati nilai pH 4.0 adalah pH yang optima, dimana ia dapat menghasilkan PPy/MnO₂ nanokomposit yang berliang tinggi, membolehkan interkalasi/deinterkalasi elektrolit yang pesat. Sedemikian itu, kapasitan tentu sehingga 306 F g⁻¹ telah diperolehi bagi nanokomposit PPy/MnO₂ yang berliang tinggi. Bahagian kedua kajian ini adalah untuk meningkatkan ciri hidrofilik elektrod PPy dengan pengintegrasian biopolimer kitosan. Sifat hidrofilik baru polypyrrole/kitosan (PPy/CS) ini menyebabkan peningkatan kepada kapasitan tentu. Justeru itu, nanokomposit PPy/CS memaparkan kapasitan tentu sebanyak 403 F g⁻¹ berbanding dengan 273 F g⁻¹ untuk elektrod PPy pada 0.2 A g⁻¹. Penilaian sudut sentuh menunjukkan peningkatan sifat hidrofilik nanokomposit PPy/CS. Peningkatan sifat hidrofilik menyebabkan permukaan nanokomposit elektrod lebih mudah untuk diakses ion dan mempermudah penyusupan elektrolit ke dalam elektrod. Bahagian ketiga kajian ini adalah untuk meningkatkan kekonduksian elektronik PPy dengan penambahan zarah Argentum (Ag). PPy yang dihiasi dengan kacukan nanozarah/nanokelompok Ag telah menunjukkan kapasitan tentu yang bernilai 414 F g⁻¹. Peningkatan kapasitan tentu adalah disebabkan oleh keunikan seni bina dan kacukan nanostruktur Ag. Nanozarah Ag menambahbaikkan sistem pelompatan elektron dalam PPy, ini mengakibatkan peningkatan sifat kapasitan

PPy. Selain daripada itu, nanokelompok Ag bertindak sebagai peruang untuk mencegah pertindihan semula filem PPy, seterusnya memperluaskan lagi tapak aktif untuk tindak balas redoks, membawakan kepada peningkatan kapasitan tentu. Bahagian akhir kajian ini bertujuan untuk menggabungkan kelebihan kitosan yang berhidrofilik dan Ag yang berkonduksian tinggi dengan PPy. Keputusan eksperimen menunjukkan bahawa nanokomposit (Ag@PPy/CS) ini memiliki kapasitan tentu setinggi 513 F g^{-1} pada 0.2 A g^{-1} . Peningkatan dalam segi pengangkutan ion elektrolit dan elektron terhasil dari gabungan kitosan dan Ag yang membawa kepada peningkatan ketara kepada kapasitan tentu PPy.

University of Malaya

ACKNOWLEDGMENTS

First and foremost, praises and thanks to the God, for His showers of blessings and strength given unto me.

I would like to express my sincere appreciation to my supervisor, Dr. Huang Nay Ming, who not only supervised but also encouraged and guided me throughout the whole duration of my research with much patience and kindness.

My special thanks are also extended to Dr. Pandikumar and Dr. Lim Yee Seng for their valuable assistance, kind advice and sharing of invaluable hands-on skills in the laboratory. Also, I would like to thank my colleagues, for creating a wonderful working environment and their selfless assistance.

To my beloved family, I cannot express enough thanks for their endless support, boundless love, encouragement and understanding throughout my PhD studies.

TABLE OF CONTENTS

Original Literary Work Declaration.....	ii
Abstract.....	iii
Abstrak.....	v
Acknowledgments.....	vii
Table of Contents.....	viii
List of Figures.....	xiii
List of Tables.....	xviii
List of Abbreviations.....	xix
List of Symbols.....	xx
CHAPTER 1: INTRODUCTION.....	1
1.1 Research Background.....	1
1.2 Energy Storage Devices.....	2
1.3 Scope of Research.....	3
1.4 Research Objectives.....	4
1.5 Outline of Thesis.....	4
CHAPTER 2: LITERATURE REVIEW.....	7
2.1 Historical Overview of Capacitors.....	7
2.2 Working Principle of Supercapacitors.....	8
2.2.1 The charge storage mechanism of EDLC.....	9
2.2.2 The charge storage mechanism of Pseudocapacitors.....	12
2.3 Principles and Methods of Experimental Evaluation.....	13
2.3.1 Cyclic Voltammetry (CV).....	15
2.3.2 Galvanostatic charge/discharge (GCD).....	17
2.3.3 Electrochemical Impedance Spectroscopy (EIS).....	19

2.4	Electrode Materials for Supercapacitors	20
2.4.1	Carbon-based Materials as EDLC	21
2.4.2	Transition Metal Oxides	25
2.4.2.1	Ruthenium oxide	25
2.4.2.2	Manganese oxides	26
2.4.3	Electrically Conducting Polymers	30
2.4.3.1	Polypyrrole (PPy)	32
2.4.3.2	PPy and PPy/carbon-based composites for supercapacitors	33
2.4.3.3	PPy/MnO ₂ composites for supercapacitors	35
2.4.3.4	PPy/Chitosan composites	40
2.5	Modifications of Electrode Material	41
2.6	Electrolytes for Supercapacitors	43
2.6.1	Aqueous Electrolyte	43
2.6.2	Organic Electrolyte	44
2.6.3	Ionic Liquid Electrolyte	45
2.7	Applications for Supercapacitors	46
2.7.1	Transportation	46
2.7.2	Stationary Electrical Energy Storage	47
2.7.3	Portable Power Systems	48
	CHAPTER 3: MATERIALS AND METHODOLOGY	49
3.1	Materials	49
3.2	Synthesis method	50
3.2.1	Synthesis of PPy/MnO ₂ nanocomposites	50
3.2.2	Synthesis of PPy/CS composite electrodes	50
3.2.3	Synthesis of Ag@PPy nanocomposites	51
3.2.4	Synthesis of Ag@PPy/CS composite electrode	51

3.3	Characterization techniques	52
3.3.1	X-ray diffraction (XRD)	52
3.3.2	Fourier transform infrared spectroscopy (FT-IR)	52
3.3.3	Raman spectroscopy	53
3.3.4	X-ray photoelectron spectroscopy	53
3.3.5	Surface area analysis	54
3.3.6	Contact Angle Measurement	54
3.3.7	Electron Microscopy	55
3.4	Evaluation of Electrochemical Properties	55
3.4.1	Cyclic Voltammetry (CV)	56
3.4.2	Galvanostatic charge/discharge	56
3.4.3	Electrochemical impedance spectroscopy	56

CHAPTER 4: EFFECT OF pH ON MORPHOLOGY AND SUPERCAPACITIVE PROPERTIES OF POLYPYRROLE/MANGANESE OXIDE NANOCOMPOSITE

4.1	Introduction	57
4.2	Results and Discussion	59
4.2.1	FTIR and Raman analysis	59
4.2.2	X-ray diffraction analysis	61
4.2.3	Morphological studies	62
4.2.4	Surface area analysis	64
4.2.5	XPS analysis	65
4.2.6	Electrochemical characterization of PPy/MnO ₂ nanocomposite	66
4.2.7	Supercapacitor device performance of porous PPy/MnO ₂ nanocomposite	70
4.3	Conclusion	74

**CHAPTER 5: EXCEPTIONAL ELECTROCHEMICAL PERFORMANCE OF
HYDROPHILIC POLYPYRROLE/CHITOSAN NANOCOMPOSITE
ELECTRODE FOR SUPERCAPACITORS..... 76**

5.1 Introduction 76

5.2 Results and Discussion..... 79

 5.2.1 Synthesis and formation mechanism 79

 5.2.2 FTIR analysis 81

 5.2.3 Morphological studies of PPy/CS nanocomposite electrodes 82

 5.2.4 Surface wettability studies of PPy/CS nanocomposite electrodes 83

 5.2.5 Electrochemical characterization of PPy/CS nanocomposite electrodes 85

 5.2.6 Supercapacitor device performance of PPy/CS nanocomposite electrode ... 87

5.3 Conclusion 93

**CHAPTER 6: HYBRID SILVER NANOPARTICLE/NANOCLUSTER-
DECORATED POLYPYRROLE FOR HIGH-PERFORMANCE
SUPERCAPACITORS 94**

6.1 Introduction 94

6.2 Results and Discussion..... 97

 6.2.1 Synthesis and formation mechanism 97

 6.2.2 FTIR and Raman analysis 98

 6.2.3 Morphological studies of Ag@PPy nanocomposite 99

 6.2.4 XPS analysis of hybrid Ag@PPy nanocomposite 103

 6.2.5 Electrochemical characterizations of Ag@PPy nanocomposite 104

 6.2.6 Supercapacitor device performance of hybrid Ag@PPy nanocomposite ... 108

6.3 Conclusion 111

**CHAPTER 7: BOOSTING THE SUPERCAPACITIVE PROPERTIES OF
POLYPYRROLE WITH CHITOSAN AND HYBRID SILVER
NANOPARTICLE/NANOCLUSTER..... 113**

7.1 Introduction 113

7.2 Results and Discussion..... 115

 7.2.1 Synthesis and formation mechanism 115

 7.2.2 FTIR and XPS analysis 116

 7.2.3 X-ray diffraction analysis 118

 7.2.4 Morphological studies..... 119

 7.2.5 Surface wettability studies 124

 7.2.6 Electrochemical characterization 125

 7.2.7 Supercapacitor device performance 128

7.3 Conclusion 132

**CHAPTER 8: CONCLUSION AND FUTURE WORK
RECOMMENDATIONS133**

8.1 Conclusion 133

8.2 Future work recommendations 135

References 137

List of Publications and Papers Presented 153

LIST OF FIGURES

Figure 1.1: Ragone plot of specific energy and power of various energy storage devices (G. Yu et al., 2013).....	3
Figure 2.1: Models of electrical double layer at a positively charged surface: (a) the Helmholtz model, (b) the Gouy-Chapman model, and (c) the Stern model showing the IHP and OHP. d is the double layer distance described by Helmholtz model. ψ_0 and ψ are the potentials at the electrode surface and the electrode /electrolyte interface, respectively (Zhang & Zhao, 2009).	10
Figure 2.2: (a) Two-electrode configuration (Stoller & Ruoff, 2010) and (b) three-electrode configuration.....	14
Figure 2.3: Cyclic voltammetry of PANI/MWCNT using (a) three-electrode (b) two-electrode configuration (Khomenko et al., 2005)	15
Figure 2.4: CV of (a) MC30HT and (b) MC60HT at various scan rates (Wang et al., 2012a).....	17
Figure 2.5: GCD curve of an electrode.	18
Figure 2.6: Nyquist plot of EIS of an electrode	20
Figure 2.7: Evolution of 2D carbon (graphene) into different building blocks of materials; buckyball, CNTs and graphite (Geim & Novoselov, 2007).....	24
Figure 2.8: Schematic illustration of the dip coating process for the synthesis of sponge@RGO@MnO ₂ (Ge et al., 2013).....	29
Figure 2.9: Chemical structures of some most common ECPs in their neutral states. (a) PANi, (b) PPy, (c) PTh, and (d) PEDOT	31

Figure 2.10: (a) Schematic illustration of the formation and (b) schematic charge storage advantage of the PPy/MnO ₂ coaxial nanotubes (Yao et al., 2013).....	36
Figure 2.11: Mechanism of regenerative brake system employed in Mazda® (http://www.mazda.com/).	47
Figure 4.1: (a) FTIR and (b) Raman spectra of PPy/MnO ₂ nanocomposite.....	60
Figure 4.2: X-ray diffraction patterns of PPy/MnO ₂ nanocomposite and sample holder.	61
Figure 4.3: FESEM images of PPy/MnO ₂ nanocomposites synthesized at various pH values of (a) 1.0, (b) 2.0, (c) 4.0, (d) 5.0, and (e) 7.8, and (f) elemental mapping of PPy/MnO ₂ nanocomposite at pH 4.0.	63
Figure 4.4: (a) N ₂ adsorption/desorption isotherm and (b) pore size distribution curve of the PPy/MnO ₂ nanocomposite prepared at pH 1.0, 4.0 and 7.8.....	65
Figure 4.5: XPS spectra of MnO ₂ /PPy nanocomposite at (a) Mn 2p and (b) O 1s core level spectra.....	66
Figure 4.6: (a) CV curves at 10 mV s ⁻¹ obtained for PPy/MnO ₂ nanocomposites prepared under different pH conditions and (b) specific capacitance values for different pH conditions calculated at current density of 0.2 A g ⁻¹	68
Figure 4.7: CV curves at various scan rates and (b) GCD curves at various current densities for porous PPy/MnO ₂ nanocomposite (pH 4.0).	69
Figure 4.8: Nyquist plots of EIS for PPy/MnO ₂ nanocomposites prepared at pH 1.0 (compact sheet), 4.0 (porous), and 7.8 (granular). Inset is a magnified portion of the high-frequency region.	70
Figure 4.9: (a) CV curves at various scan rates, (b) galvanostatic charge/discharge curves at various current densities, and (c) Ragone plot of the symmetric supercapacitor device.	71

Figure 4.10: Dependence of specific capacitance values on current density for the symmetric supercapacitor device.	73
Figure 4.11: Cycling stability of the fabricated symmetric supercapacitor device.....	74
Figure 5.1: Mechanism for the formation of PPy/CS nanocomposite electrode.	80
Figure 5.2: FTIR of CS, PPy and PPy/CS.	82
Figure 5.3: FESEM images of (a) pure PPy; PPy/CS nanocomposite electrodes with CS contents of (b) 0.5, (c) 0.75, (d) 1.0 wt%, and (e) elemental mapping of the PPy/CS-0.75 nanocomposite electrode.....	83
Figure 5.4: Digital images of water droplets on the surfaces of the as-prepared electrodes.....	84
Figure 5.5: (a) CV curves at 25 mV s^{-1} , (b) GCD curves at 0.2 A g^{-1} , (c) dependence of specific capacitance on current density for PPy and PPy/CS nanocomposite electrode, and (d) CV curves of PPy/CS nanocomposite electrode as a function of scan rate.....	86
Figure 5.6: Specific capacitance values for different CS content calculated at current density of 0.2 A g^{-1}	87
Figure 5.7: Nyquist plots of EIS for the as-fabricated symmetric supercapacitors of PPy and PPy/CS nanocomposite electrodes at 0.50, 0.75 and 1.0 wt% chitosan.....	89
Figure 5.8: (a) CV curves at various scan rates, (b) GCD curves at various current densities of the PPy/CS symmetric supercapacitor, and (c) comparison of the dependence of specific capacitance on current density of the PPy and PPy/CS symmetric supercapacitor.....	91
Figure 5.9: (a) Ragone plots, and (b) cycling stability plots for the symmetric supercapacitors of PPy and PPy/CS.....	92
Figure 6.1: Physical appearance of the reaction mixture after stirring for 5 min prior to electrodeposition.	98
Figure 6.2: (a) FTIR and (b) Raman spectra of PPy and Ag@PPy.	99

Figure 6.3: FESEM images of (a) pure PPy, inset showing PPy at lower magnification; Ag@PPy nanocomposites with AgNO ₃ concentrations of (b) 0.01 M, (c) 0.05 M, (d) 0.10 M, and (e) elemental mapping of the 0.05M-Ag@PPy nanocomposite.	101
Figure 6.4: Schematic representation of the evolution of different Ag@PPy nanocomposites.	102
Figure 6.5: HRTEM images of (a) Ag nanoclusters and (b) Ag nanoparticles.	102
Figure 6.6: XPS spectra of Ag@PPy nanocomposite at (a) N 1s and (b) Ag 3d core level spectra.	103
Figure 6.7: CV curves at 10 mV s ⁻¹ , (b) GCD curves at 0.2 A g ⁻¹ , and (c) dependence of specific capacitance on current density for PPy and hybrid Ag@PPy nanocomposite electrode.	106
Figure 6.8: CV curves at various scan rates for (a) PPy, and (b) hybrid Ag@PPy nanocomposite electrode.	107
Figure 6.9: Specific capacitance values for different AgNO ₃ concentrations calculated at current density of 0.2 A g ⁻¹	108
Figure 6.10: (a) CV at various scan rates and (b) GCD at various current densities of the as-fabricated symmetric supercapacitor of Ag@PPy nanocomposite.	109
Figure 6.11: Nyquist plots of EIS for the symmetric supercapacitors of PPy and hybrid Ag@PPy nanocomposites. Inset is a magnified portion of the high-frequency region.	110
Figure 6.12: (a) Ragone plot, and (b) cycling stability of the symmetric supercapacitors of PPy and hybrid Ag@PPy nanocomposite.	111
Figure 7.1: Physical appearance of the reaction mixture after stirring for 5 min prior to electrodeposition.	118
Figure 7.2: (a) FTIR of CS, PPy, Ag@PPy, PPy/CS and Ag@PPy/CS (b) XPS spectra of Ag@PPy and Ag@PPy/CS nanocomposite electrodes at Ag 3d core level spectra.	121

Figure 7.3: FESEM images of (a) PPy, (b) PPy/CS, (c) Ag@PPy, (d) Ag@PPy/CS nanocomposite electrodes, and (e) elemental mapping of the Ag@PPy/CS nanocomposite electrode. Insets of (c) and (d) show the lower magnification images of the respective nanocomposites.....	121
Figure 7.4: HRTEM images of (a) Ag nanoclusters, (b) Ag nanoparticles from Ag@PPy and (c) Ag nanoclusters and (d) Ag nanoparticles from Ag@PPy/CS.....	123
Figure 7.5: Digital images of water droplets on the surfaces of the as-prepared electrodes.....	125
Figure 7.6: (a) CV curves at 10 mV s^{-1} and (b) GCD curves at 0.2 A g^{-1} of the as-synthesized electrodes.....	127
Figure 7.7: (a) CV curves at 10 mV s^{-1} , (b) CV curves of Ag@PPy/CS symmetric supercapacitor at various scan rates, (c) GCD curves at 0.2 A g^{-1} , and (d) comparison of the dependence of specific capacitance on the current density of the symmetric supercapacitors.....	129
Figure 7.8: Nyquist plots of EIS for the as-fabricated symmetric supercapacitors.	130
Figure 7.9: (a) Ragone plots, and (b) cycling stability plots for the symmetric supercapacitors.....	132

LIST OF TABLES

Table 2.1: Summary of a selection of PPy and PPy/carbon-based composites for supercapacitors. Specific capacitance values are reported from three-electrode configuration unless otherwise stated.	33
Table 2.2: Specific capacitance of a selection of PPy/MnO ₂ composites reported in the literature. Specific capacitance values are reported from three-electrode configuration unless otherwise stated.	39
Table 3.1 Materials and chemicals used in this thesis.....	49
Table 4.1: BET specific surface areas (S_{BET}), total pore volumes, and average pore sizes of PPy/MnO ₂ nanocomposites.	65
Table 5.1: The ESR and R_{ct} values of the symmetric supercapacitors of PPy and PPy/CS nanocomposites obtained from Nyquist plot.	89
Table 7.1: Electrochemical data for Ag@PPy and Ag@PPy/CS nanocomposite electrodes.....	127
Table 7.2: The ESR and R_{ct} values of the symmetric supercapacitors extracted from the Nyquist plots.	131

LIST OF ABBREVIATIONS

AC	Activated carbon
Ag	Silver
AgNO ₃	Silver nitrate
Ag@PPy	Silver/polypyrrole
Ag@PPy/CS	Silver/polypyrrole/chitosan
BET	Brunauer–Emmett–Teller
BJH	Barret-Joyner-Halenda
CNT	Carbon nanotubes
CS	Chitosan
CV	Cyclic voltammetry
DI	Deionized
ECP	Electrically conducting polymer
EDLC	Electrical double layer capacitance
EES	Electrochemical energy storage
EIS	Electrochemical impedance spectroscopy
ESR	Equivalent series resistance
FeCl ₃	Iron (III) chloride
FESEM	Field emission scanning electron microscopy
FTIR	Fourier transform infrared spectroscopy
GCD	Galvanostatic charge discharge
H ₂ SO ₄	Sulfuric acid
HRTEM	High resolution transmission electron microscopy
IHP	Inner Helmholtz plane
KMnO ₄	Potassium permanganate (VII)
MnO ₂	Manganese (IV) oxide
Na ₂ SO ₄	Sodium sulfate
NapTS	Sodium p-toluenesulfonate
OHP	Outer Helmholtz plane
PANi	Polyaniline
PEDOT	Poly(3,4-ethylenedioxythiophene)
PPy	Polypyrrole
PPy/CS	Polypyrrole/chitosan
PPy/MnO ₂	Polypyrrole/manganese oxide
PTh	Polythiophene
RuO ₂	Ruthenium oxide
SCE	Saturated calomel electrode
XPS	X-ray photoelectron spectroscopy
XRD	X-ray diffraction

LIST OF SYMBOLS

C	Capacitance
C_{diff}	Diffuse region double layer capacitance
C_{dl}	Double layer capacitance
C_{H}	Helmholtz type inner region capacitance
I	Current
m	Mass
Q	Charge
R_{ct}	Charge transfer resistance
S_{BET}	Specific surface area
T	Time
V	Voltage
v	Scan rate
wt%	Weight percentage
Z'	Real impedance
Z''	Imaginary impedance

University of Malaya

CHAPTER 1

INTRODUCTION

1.1 Research Background

According to The World Energy Outlook 2014, global energy demands will grow by 37% by 2040 (World Energy Outlook, 2014). However, nearly 80% of today's world energy is supplied by fossil fuels, including oil, gas and coal. These non-renewable fossil fuels produce exhaust in the form of CO₂ and are projected to rise to 45 billion metric tons in 2040, contributing largely to global warming (Energy Information Administration, 2013).

Limited resources of fossil fuels and the destructive climate change have been driving the world towards clean and renewable energy development. The utilization of natural energy sources such as wind, hydro and solar energy has become increasingly important to reduce the dependence on fossil fuels for global energy demands. However, the lack of continuous availability is a major drawback for these renewable sources, as most renewable energy resources depend on the climate (Baños et al., 2011). Solar energy devices are unable to generate electricity during the night but may generate surplus amounts of energy during the day. A rational approach is to develop energy storage devices that can store large amount of the harvested energy. The fast-growing development for clean and sustainable energy has to be in unison with the development of energy storage devices. Therefore, there has been an increasing and urgent demand for a variety of environmental friendly and reliable energy storage devices for a wide range of applications.

1.2 Energy Storage Devices

Efficient electrochemical energy storage (EES) systems are critically needed with the increased usage of transportation industry, consumable electronic devices, and industrial electronic devices. EES are vital to promote the reliability and the effective use of the entire power system (generation, transmission and distribution) by releasing energy when in high demand and storing energy when in excess. EES systems to meet these needs requirements include batteries, fuel cells, supercapacitors and conventional capacitors.

The performance of energy storage devices based on the power and energy density can be expressed by Ragone plot as shown in **Figure 1.1**. As seen from the Ragone plot, supercapacitors are considered high power systems whilst batteries and fuel cells are considered to be high energy systems. It can be noted that no single energy device can match all power and energy region.

Supercapacitors, also known as electrochemical capacitors or ultracapacitors, have attracted great attention due to their superior fast charging and discharging process, long cycle life, and environmental friendliness. Supercapacitors are excellent candidate to meet the ever increasing power demands of energy storage systems in the twenty-first century. They bridge the performance gap between conventional capacitors and batteries; offering higher energy density as compared to conventional capacitors and higher power density than batteries. One of the main challenges in the development of supercapacitors continues to be the enhancement of their energy densities, as they are still relatively lower than batteries and fuel cells. Thus, tremendous amount of efforts have been devoted to construct higher performance supercapacitors with higher energy densities while maintaining its desirable high power densities.

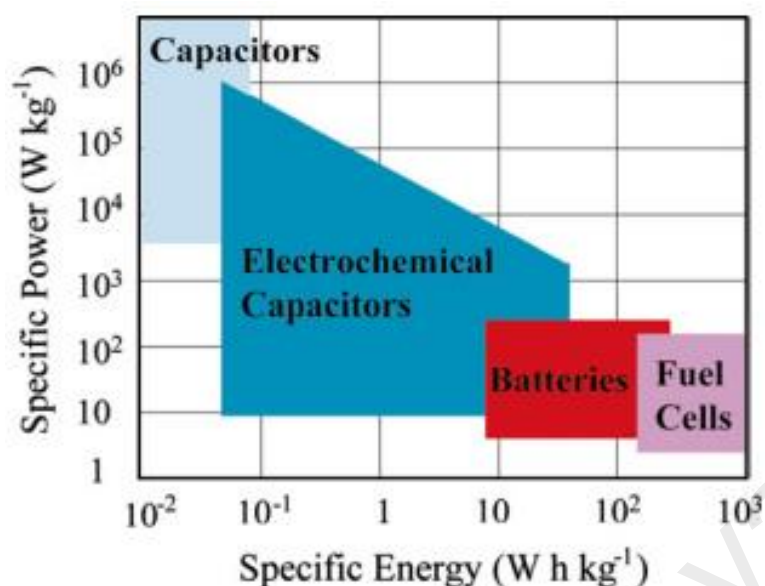


Figure 1.1: Ragone plot of specific energy and power of various energy storage devices (G. Yu et al., 2013)

1.3 Scope of Research

As the title of this thesis suggests, the aim of this thesis is on designing and preparing novel polypyrrole-based materials with enhanced electrochemical performance as well as good cycling stability. The motivation behind this doctoral work is to prepare polypyrrole nanocomposite electrodes through simple and cost-effective methodologies. This doctoral work also focuses on the integration of polypyrrole with materials that are not commonly used in supercapacitors applications such as silver and chitosan, giving rise to novel materials with interesting features for high-performance supercapacitor applications. There is also an effort to understand the relationship between the as-prepared materials and their enhanced supercapacitor performance, which could provide guidelines for supercapacitor designs in the future.

1.4 Research Objectives

- 1) To develop a facile and cost-effective method for the preparation of polypyrrole-based nanocomposite materials consisting of polypyrrole for high-performance supercapacitor electrodes.
- 2) To investigate and evaluate the supercapacitive properties of the as-prepared polypyrrole nanocomposites.
- 3) Optimizing the synthesis parameters that affect the electrochemical properties.
- 4) Understanding the relationship between the new polypyrrole-based nanocomposites and their supercapacitance performances.
- 5) Laboratory scale fabrication of symmetric supercapacitors using the developed PPy-based electrodes in order to access the potential performance in a real device.

1.5 Outline of Thesis

The structure of this thesis can be summarized as follows.

Chapter 1 begins with a brief discussion on the world energy crisis and the rationale of developing energy storage systems. Then, the motivation and research objectives of this study using polypyrrole based nanocomposite materials were discussed.

Chapter 2 serves to provide a comprehensive literature review on the energy storage principles of supercapacitors and the commonly used techniques for evaluating the electrochemical properties of supercapacitors. The latter part of chapter 2 is devoted to discuss the electrode materials used for supercapacitors followed by current applications of supercapacitors.

Chapter 3 presents the synthesis of PPy based nanocomposite via different methods and their characterization techniques. Instrumental analyses, including Fourier transform infrared spectroscopy (FTIR), Raman spectroscopy, X-ray diffraction (XRD), X-ray photoelectron spectroscopy (XPS), field-emission scanning electron microscopy (FESEM), high resolution transmission electron microscopy (HRTEM) and surface area analysis.

Chapter 4 discusses the synthesis and characterization of polypyrrole/manganese oxide (PPy/MnO₂) nanocomposite with emphasis on the effect of pH on the morphology and electrochemical performance of the nanocomposite.

Chapter 5 focuses on the experimental setup of the preparation and characterization of hydrophilic polypyrrole/chitosan (PPy/CS) nanocomposite electrodes *via* a one-step electrodeposition. The addition of chitosan successfully increased the surface wettability of the electrode. Also, the specific capacitances of the PPy/CS electrodes are optimized based on the amount of chitosan used in the synthesis.

Chapter 6 describes a novel method to synthesize silver-decorated polypyrrole (Ag@PPy). The formation of silver nanoparticles and nanoclusters with respect to the concentration of silver nitrate was investigated. The plausible mechanism of silver nanoclusters and nanoparticles on the PPy film was postulated.

Chapter 7 presents the fabrication of a new ternary nanocomposite consisting of PPy, chitosan and silver (Ag@PPy/CS) as a promising electrode for supercapacitor. The merits of silver and chitosan in the nanocomposite were investigated. The benefits of both silver and chitosan brought about enhanced supercapacitive properties of PPy.

Chapter 8 concludes the thesis with major findings in terms of improving the specific capacitance of PPy-based supercapacitors and also the formation of new PPy nanocomposites. Possible future research recommended for the enhancement of supercapacitor performances are proposed at the end of this chapter.

University of Malaysia

CHAPTER 2

LITERATURE REVIEW

2.1 Historical Overview of Capacitors

The discovery of electrical charge storage on surfaces was attributed to the rubbing of amber in ancient times. Leyden jar was the first instrument to make usage of such charge storage, invented independently by Pieter van Musschenbroek of Kamin and Dean Kliest at Leyden in the mid-eighteenth century (Conway, 1999).

A typical design of the Leyden jar consisted of a glass vial, containing acidic electrolyte as a conductor and which was contacted by an immersed metal electrode. The glass medium is used as a dielectric between the conducting metal coating on the inner and outer surfaces. The outer and inner surfaces store equal but opposite charge and this double layer charging occurs due to the presence of the acidic electrolyte. Charging of the Leyden jars were usually carried out using electrostatic generators such as the Hawkesbee machine.

In the early twentieth century, an improved version of the Leyden jar called the electrophorus was invented by Volta. An ebonite (a hard plastic) is used as the dielectric material instead of glass and sandwiched between two metal electrodes. The first patented electrochemical capacitor based on carbon material in an aqueous electrolyte that utilized the interfacial double-layer effect to store electrical energy, was attributed to Becker and his employer General Electric in 1957 (Becker, 1957). In 1966, supercapacitors became available on the market sold by SOHIO Corporation using double layer capacitance of high surface area carbon materials and tetraalkylammonium salt as a non-aqueous electrolyte to provide higher operating voltage (3.4 – 4.0 V) and larger specific energy storage (Donald, 1970).

Conway and co-workers developed a different type of capacitor based on pseudocapacitance in 1975 through the efforts at the Continental Group and the Hooker Corporation based on transition metal oxides such as RuO_2 . These pseudocapacitors relied on an electrochemical reaction for charge storage similar to batteries; however, they were able to mimic the response behavior of traditional capacitors with high degree of reversibility (Conway, 1999). The major types of supercapacitors and their charge storage mechanisms are presented later in this chapter.

2.2 Working Principle of Supercapacitors

Supercapacitors can be classified into two categories based on their capacitive behavior: the electric double layer capacitors (EDLC) and pseudocapacitors. EDLC store their charges by non-Faradaic charge accumulation at the electrode/electrolyte interface while pseudocapacitors rely on the fast and reversible surface redox processes that take place between the electrode and electrolyte. Depending on the nature of the electrode material, supercapacitors can sometimes store energy using both mechanisms, simultaneously. However, the charge storage mechanisms of EDLC and pseudocapacitors will be discussed separately in this chapter, in order to give a better and clearer understanding.

2.2.1 The charge storage mechanism of EDLC

The fundamental charge storage process of EDLC is by an electrostatic way, as the negative and positive electric charges residing on the plates of a capacitor are separated by a vacuum or a dielectric material. This process is also known as non-Faradaic electrical energy storage. A few models were proposed to describe the electric double layer that occurs at the interfaces between the electrode and the electrolyte.

The concept of a double layer was first introduced by von Helmholtz to describe the distribution of the opposite charges at the interface of colloidal particles. As illustrated in **Figure 2.1a**, the Helmholtz double layer model consists of two layers of opposite charges separated by a small distance having atomic dimensions, similar to that of a two-plate conventional capacitors. This Helmholtz model was later adapted to the case of electrode interfaces, where on the solid material, a controllable surface density of excess negative or positive charge is balanced by the counterions at the electrode/electrolyte interface within an atomic distance from the electrode surface. However, some time after the Helmholtz was proposed, it became realized that the electrolyte ions in the double layer would not remain static in a compact array as shown in the model, but instead will be subjected to the effects of thermal fluctuation of the electrolyte ions.

By taking into account the effects of thermal fluctuation and the continuous distribution of the electrolyte ions, Gouy and Chapman modified Helmholtz's representation of a double layer and is commonly referred as the "diffuse" double-layer model. Instead of static charges, the counterions conjugate to the electrode were envisaged as a 3-dimensional diffusely distributed population of anions and cations of the electrolyte as shown in **Figure 2.1b**. In this model, the ions were assumed to be point charges with the electrolyte having a net charge density equal and opposite to the

electrode surface. However, the Gouy-Chapman model leads to overestimation of the double layer capacitance since the capacitance of two separated arrays of charges increases inversely with their separation distance.

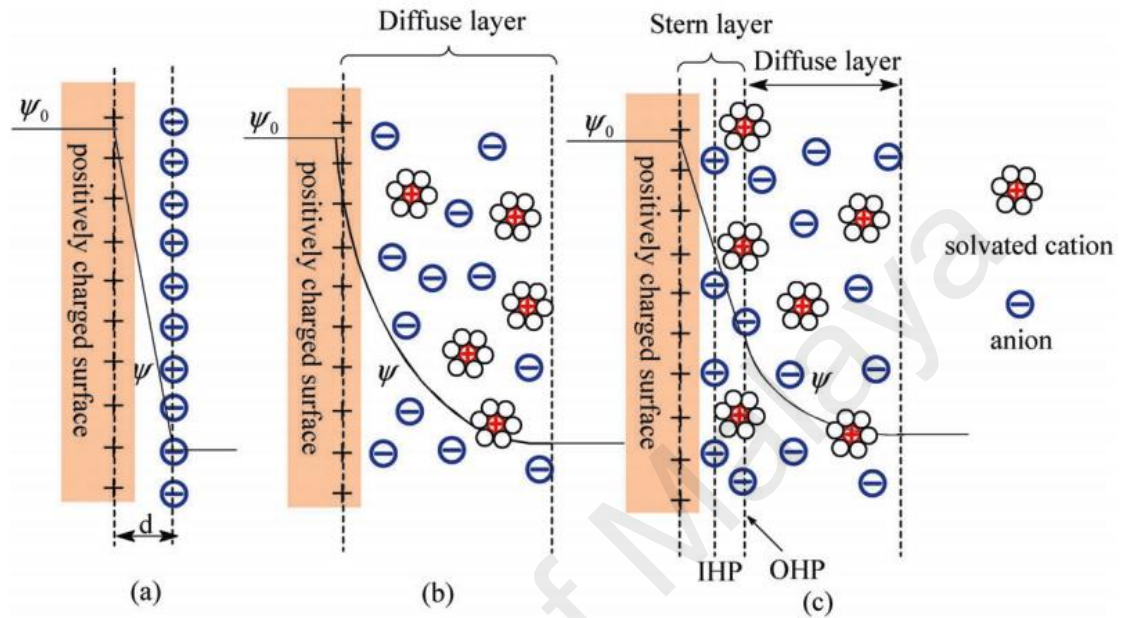


Figure 2.1: Models of electrical double layer at a positively charged surface: (a) the Helmholtz model, (b) the Gouy-Chapman model, and (c) the Stern model showing the IHP and OHP. d is the double layer distance described by Helmholtz model. ψ_0 and ψ are the potentials at the electrode surface and the electrode /electrolyte interface, respectively (Zhang & Zhao, 2009).

In 1924, Stern (Conway, 1999) overcame the overestimation of the double layer capacitance of the diffuse layer model. Stern combined the Helmholtz model with Gouy-Chapman model that take into account the two regions of ion distribution – the inner region called the compact layer or Stern layer and the layer beyond the inner layer called the diffuse layer. The stern layer is analogous to the adsorption process according to Langmuir’s adsorption isotherm, where the ions are strongly adsorbed by the electrode, thus the name compact layer. The inner Helmholtz plane (IHP) located in the stern layer refers to the distance of the closest approach of specifically adsorbed ions (ions that are in direct contact to the electrode). The outer Helmholtz plane (OHP)

marks the end of the inner region and beginning of the diffuse layer as shown in **Figure 2.1c**. The OHP refers to the non-specifically adsorbed ions is also what the Gouy and Chapman model defines.

In this model, the ions were recognized as having finite sizes, including the annular thickness of the hydration shell. Hence, the geometrical limit to the compact region of the adsorption layer at the electrode can be determined easily. The overall capacitance in the electric double layer (C_{dl}) can be represented as the combination of the capacitances from the two regions, the inner region resembles to a Helmholtz type of compact double layer capacitance (C_H) and the diffuse region capacitance (C_{diff}). Thus C_{dl} can be expressed by the following equation:

$$\frac{1}{C_{dl}} = \frac{1}{C_H} + \frac{1}{C_{diff}} \quad \text{Equation 2.1}$$

The capacitance of two separated layers of charges increases inversely as their separation distance as presented by the Gouy-Chapman model. This leads to large capacitance values since the limit of infinitesimally small ions closely approaches the electrode surface. This overestimation of the double layer capacitance is automatically avoided by the introduction of a distance of closest approach of finite-sized ions and thus geometrically defining a compact Helmholtz inner region. The Stern model of double layer remained as a good basis for general interpretation of the electrode/electrolyte interface phenomena until the detailed work of Grahame in the 1947 on the double layer capacitance.

2.2.2 The charge storage mechanism of Pseudocapacitors

Apart from the EDL capacitance in which the charges are stored electrostatically (i.e., non-Faradaically), complement to this type of capacitance is the so-called “pseudocapacitance”. The term “pseudocapacitance” is used to describe the behavior of electrode materials that have the electrochemical signature of a capacitive electrode but in which the charge storage originates from a completely different reaction mechanism (Brousse et al., 2015).

Pseudocapacitance involves the passage of charge across the double layer that is Faradaic in origin whilst capacitance of EDL comes from the charge separation in the double layer formed at the interface between the solid electrode material and the liquid electrolyte. Pseudocapacitance arises for thermodynamic reasons between the extent of charge acceptance (Δq) and the change of potential (ΔV) (Conway, 1999). The following derivative is equivalent to the capacitance.

$$C = \frac{d(\Delta q)}{d(\Delta V)} \quad \text{Equation 2.2}$$

Generally, there are two types of electrochemical processes that contribute to pseudocapacitance which include the redox reaction at the transition metal oxide’s surface with ions from the electrolyte, and the doping and dedoping of active conducting polymer material in the electrode. The former process is based primarily on surface mechanism and hence it is highly dependent on the surface area of the electrode material. The latter process involving the conducting polymer material is more of a bulk process and much less dependent on its surface area although a relatively high surface area is useful in the distribution of electrolyte ions to and from the electrodes in a cell (Burke, 2000). In all cases, the electrodes must have high electronic conductivity to distribute and collect the electron current.

It is now known that the about 1-5% of the capacitance of carbon-based double layer capacitors is contributed by pseudocapacitance due to the Faradaic reactions of the oxygen-functionalities on the surface (depending on the conditions of preparation of the carbon material). On the other hand, pseudocapacitors will always exhibit some electrostatic double layer capacitance component of about 5-10%, in some case even higher, depending on the surface area of the pseudocapacitor electrode. This non-Faradaic contribution is proportional to their electrochemically accessible interfacial surface area (Conway, 1999).

2.3 Principles and Methods of Experimental Evaluation

During the course of development, the design of supercapacitors and measurement of their capacitances are essential to evaluate the performance and applicability and suitability of electrode materials. Currently, two types of electrode configuration are generally employed to evaluate the supercapacitive properties of an electrode material, namely, two-electrode configuration and three-electrode configuration.

A typical two-electrode cell assembly is displayed in **Figure 2.2a**. The electrodes are isolated from electrical contact by a porous separator. The separator and electrodes are impregnated with an electrolyte, which allows ionic current to flow between the electrodes while preventing electronic current from discharging the cell. The drawback of this simple experiment setup is that it does not provide the characterization of the material over a given operating potential, and rather it describes the overall behavior of a cell. Hence, two-electrode cells are recommended for the evaluation of cell performance approaching to the actual supercapacitors (Inagaki et al., 2010).

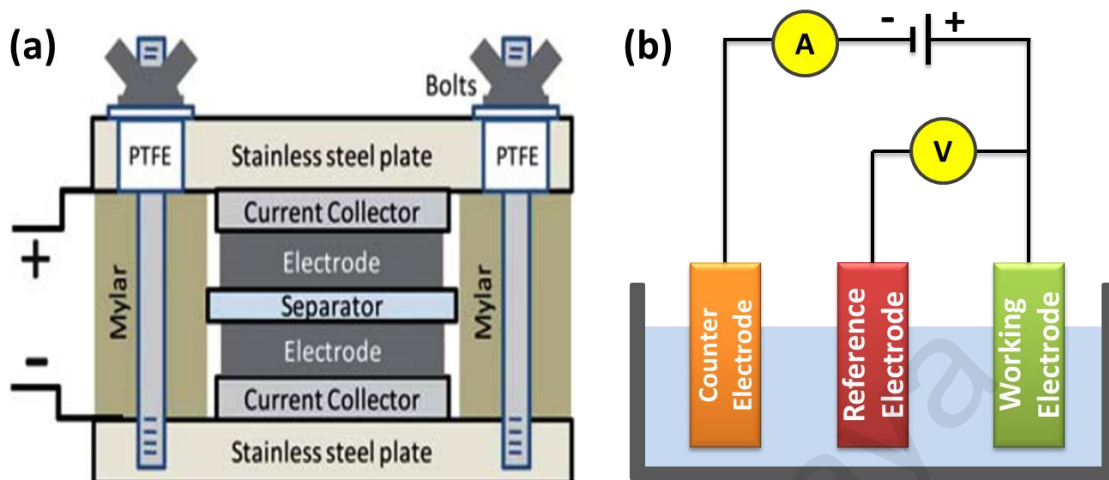


Figure 2.2: (a) Two-electrode configuration (Stoller & Ruoff, 2010) and (b) three-electrode configuration

A three-electrode configuration composed of a working electrode, a reference electrode and a counter electrode as shown in **Figure 2.2b**. The working electrode contains the active material being analyzed and the applied voltage potential is referenced to a standard reference electrode. The counter electrode, also called an auxiliary electrode, is usually a platinum wire. Commonly used reference electrodes are silver/silver chloride (Ag/AgCl) and saturated calomel electrode (SCE). This type of configuration is valuable for the investigation of the material's intrinsic electrochemistry properties such as Faradaic reactions and diffusion. Many of these vital electrochemical properties can only be seen when the electrode material is being tested using the three-electrode configuration. As shown in **Figure 2.3**, the CV of a three-electrode cell using PANI/MWCNT as the electrode material clearly indicated the oxidation and reduction peaks at certain potentials, however this is not observed when the same electrode material was assembled in a two-electrode configuration (symmetric capacitor). This isolation allows assessment of the electroactive behavior of a single

electrode material over many different potential windows to properly ascertain its applicable usage. This is especially useful for evaluating the performance of a novel supercapacitor electrode.

Electrochemical techniques such as cyclic voltammetry (CV), galvanostatic charge/discharge (GCD) and electrochemical impedance spectroscopy (EIS) is used to characterize and evaluate the electrochemical performance of electrode materials.

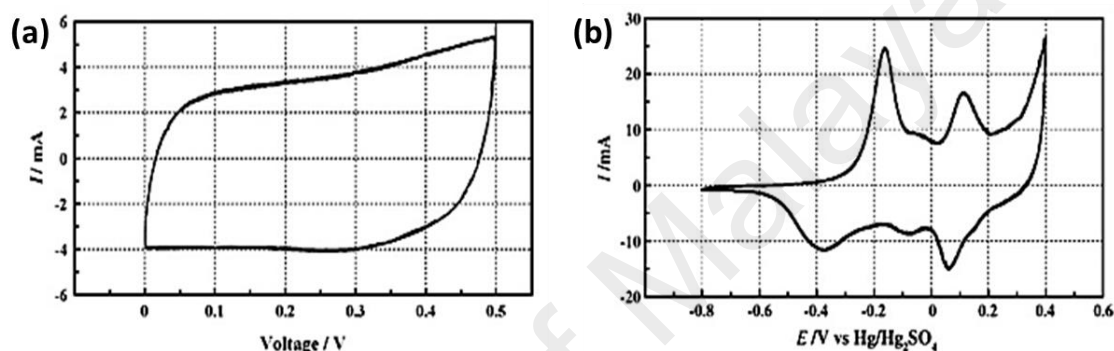


Figure 2.3: Cyclic voltammetry of PANI/MWCNT using (a) three-electrode (b) two-electrode configuration (Khomenko et al., 2005)

2.3.1 Cyclic Voltammetry (CV)

Cyclic voltammetry is a type of potentiodynamic electrochemical measurement and it can be used as a diagnostic tool in analyzing the potential of an electrode material. As the name suggest, the potential is cycled between two pre-determined voltages linearly versus time (i.e., scan rate). After the set potential is reached in a CV experiment, the working electrode's potential is swept in the reverse direction to return to the initial potential. These forward and reverse sweeps may be repeated as many times as desired. A cyclic voltammogram is displayed when the response current of working electrode is plotted versus the applied potential.

The specific capacitance can be estimated using the voltammetric charge integrated from the CV curve according to the following equation (Patil et al., 2013; Wang & Zhitomirsky, 2011):

$$C = \frac{Q}{2m\Delta V} = \frac{1}{2m\Delta V\nu} \int i(V) dV \quad \text{Equation 2.3}$$

C is the specific capacitance in F g^{-1} , m is the mass of the active material in the electrode, ΔV is the potential window and Q is the total charge that can be obtained by the dividing the integrated area of a CV curve with the scan rate, ν .

The CV of most supercapacitors will show some deviations from the rectangular shape. The rectangular shapes of the CV becomes more distorted at higher scan rates due to the lesser charge mobilization per unit time of the electrolyte into the interior surfaces of the active material, resulting in less utilization of the electrode material compare to low scan rates. Furthermore, when an electrode material has poor electrical conductivity, the rectangular CV curve will be distorted even more dramatically (Zhang & Zhao, 2012). **Figure 2.4** compares the degree of distortion at high scan rates. This indicates MC30HT has better capacitive behavior and rate capability than MC60HT (Wang et al., 2012a). The degree of distortion may provide valuable information about the intrinsic resistance and the applicability of an electrode material.

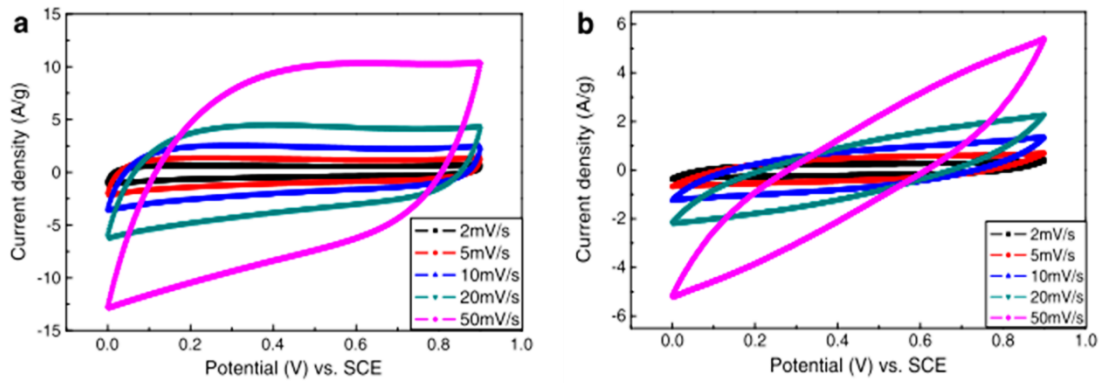


Figure 2.4: CV of (a) MC30HT and (b) MC60HT at various scan rates (Wang et al., 2012a).

2.3.2 Galvanostatic charge/discharge (GCD)

GCD, also known as chronopotentiometry, is used to measure the rate of change of potential at an electrode measured at a constant current in which the electrode is charged to a set potential and subsequently discharging. This experimental procedure has been proven extremely useful as the specific capacitance, energy and power density can be accurately calculated.

The specific capacitance of the electrode (C) can be calculated from the discharge portion of the GCD curve by employing the equation (Long et al., 2015):

$$C = \frac{I\Delta t}{m\Delta V} \quad \text{Equation 2.4}$$

in which I is the discharge current, Δt is the discharge time, m is the mass of the active material in the electrode and ΔV is the voltage after IR drop. The IR drop is a drop in the voltage at the initial portion of the discharge curve that exhibits a sudden drop due to the internal resistance of the electrode as shown in **Figure 2.5**.

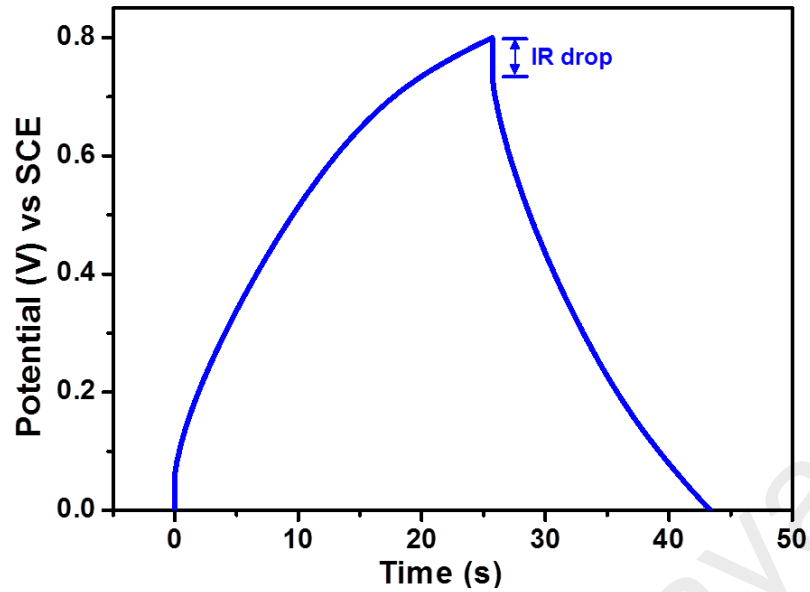


Figure 2.5: GCD curve of an electrode.

Energy density and power density are two crucial parameters to evaluate the capacitive performance of an electrode. The energy density reflects the amount of energy stored to perform work, whereas the power density exhibits how quickly the energy can be supplied. The energy density, E (W h kg^{-1}), and power density, P (W kg^{-1}), can also be calculated from the discharge curve by the following equations (Yan et al., 2012):

$$E = \frac{1}{2} C \Delta V^2 \quad \text{Equation 2.5}$$

$$P = \frac{E}{\Delta t} \quad \text{Equation 2.6}$$

2.3.3 Electrochemical Impedance Spectroscopy (EIS)

Electrochemical impedance spectroscopy is a powerful tool to evaluate the electrochemical system of a supercapacitor and it's useful for research and development of new electrode materials. It can accurately measure error-free kinetic and mechanistic information using a variety of techniques and output formats. During an impedance measurement, a frequency response analyzer is used to impose a small amplitude of potential in a range of fixed frequency (generally from 100 kHz to 10 mHz). The used of the small amplitude is to ensure minimal perturbation of the electrochemical test system, reducing errors caused by the measurement technique.

This method is especially valuable because it enables the equivalent series resistance (ESR) of the electrode materials and the charge transfer resistance (R_{ct}) of the system to be separately evaluated. The Nyquist plot is used as to evaluate the phase relation between the imaginary phase (Z'') and the real phase (Z') of the impedances as shown in **Figure 2.6**.

The first intercept of the semicircle at the real axis in the high frequency region represents the ESR, which is attributed to the resistance of the electrolyte; the contact resistance between the electrolyte, current collector, and active material; and the intrinsic resistance of the active material itself (Ju et al., 2008). The R_{ct} can be estimated from the diameter of the semicircle. The charge transfer resistance is the resistance between the electrode and the aqueous electrolyte, i.e., the electrode/electrolyte interface. The key benefit of Nyquist plot is the convenience of observing the effects of the ohmic resistance of an electrode material. The slope in the lower frequency region relates to the capacitive behavior and the ionic diffusion of an electrode. A steeper slope that is nearly perpendicular to the real axis (Z') indicates good capacitive behavior and ionic diffusion, all of which are ideal characteristics of a good electrode for

supercapacitor applications (Yen et al., 2014). It is worth noting that the understanding and analysis of the Nyquist plot of EIS is based on a case-by-case basis, notably for pseudocapacitive materials with a complex kinetics of electrode process because a perfect semicircle is not obtained usually (Wu, 2014).

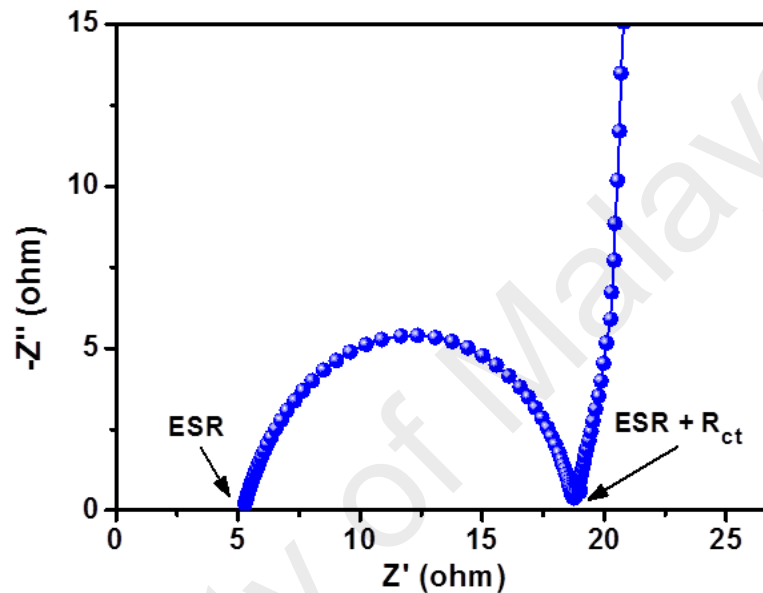


Figure 2.6: Nyquist plot of EIS of an electrode

2.4 Electrode Materials for Supercapacitors

The discussions in the earlier sections have shown the performance of a supercapacitor device is highly dependent on the electrode material from which it is constructed. In addition, the types of electrolyte systems also have crucial effects on the performance of the supercapacitors. Carbon-based materials are widely used as the electrode material for EDLC whereas pseudocapacitors in general consist of metal oxides and electrically conducting polymer.

The common materials used as EDLC and the use of different electrolyte systems will be discussed briefly in the following section. On the other hand, pseudocapacitor materials will be introduced afterwards in a more detailed manner, considering their relevance to the current work.

2.4.1 Carbon-based Materials as EDLC

Early researches on supercapacitors mainly involved carbon-based materials that exhibited electrical double layer type of capacitance. The reasons for the popularity of carbon-based materials as supercapacitors electrodes include low cost, its availability, high temperature stability, good corrosion resistance, and established electrode production technologies (Frackowiak, 2007; Inagaki et al., 2010).

Carbon-based materials are the most widely used commercial electrode material for supercapacitors and they come in various forms such as activated carbon (AC), mesoporous carbon, carbon aerogel, carbon nanotubes and graphene. These materials exhibited high double layer capacitance by storing charges electrostatically due to their high specific surface area (Frackowiak, 2007).

Activated carbon (AC) can be easily obtained through the pyrolysis of various carbonaceous source such as coal (Lozano-Castelló et al., 2003), soy beans (Long et al., 2015), watermelons (Wu et al., 2013), durian shells (Ong et al., 2012), coconut shells (Mi et al., 2012), oil palm kernel shells (Misnon et al., 2015) and also from synthetic polymers such as polyacrylonitrile (Ra et al., 2009), polyaniline (Yan et al., 2010) and polypyrrole (Wei et al., 2012). The pore size of these carbon materials can be more or less controllable depending on the type of precursor and activation processes such as temperature, time and type of activating agent may significantly affect the

microporosity of the resultant carbons (Frackowiak, 2007). Two types of activation process are generally employed to make ACs. Physical activation refers to the treatment of a carbon precursor under high temperature (up to 1200 °C) in the presence of oxidizing gasses such as steam, CO₂ and air. Chemical activation involves an activating agent like potassium hydroxide (Yan et al., 2010), phosphoric acid (Kim, 2004) and zinc chloride (Ozdemir et al., 2014) to create the highly porous structure.

ACs are characterized by extremely large surface areas which range from 500 – 3000 m² g⁻¹ which can positively contribute to the charge storage of an EDLC. However, disproportion between the specific capacitance of the AC and specific surface area is also commonly observed due to the various types of pore sizes produced by the activation process that are namely, micropores (< 2 nm), mesopores (2 – 50 nm) and macropores (> 50 nm). For instance, an AC with a surface area of about 3000 m² g⁻¹ displayed a relatively small specific capacitance of less than 10 μF cm⁻², which is smaller than the theoretical EDL capacitance (15 – 25 μF cm⁻²) (Conway, 1999). The reason behind the disproportion is due to the fact that not all pores are electrochemically accessible to electrolyte ions and therefore are not effective in charge accumulation (Kierzek et al., 2004).

Micropores less than 2 nm which contributed to high specific surface area may not be accessible to electrolyte within a short time frame as they posed increased length for ion diffusion, limiting the ability to form a double layer. However, these micropores can become accessible to electrolyte if a low current loading is applied as more time is given for the electrolyte to travel into the smaller pores. On the other hand, the surface area arising from mesopores within the size range of 3 nm to tens of nanometers allow faster and more efficient charging/discharging as compared to micropores, hence, are more suitable for high power supercapacitor applications because the charges can be stored and removed faster, giving rise to higher power, although less energy can be

stored (Zhang et al., 2009). These imply that specific surface area is not the sole parameter for evaluating the performance of EDLCs, other aspects of the electrode such as pore size distribution, pore size and connectivity, electrical conductivity and surface functionalities may significantly influence an electrode's electrochemical performance. Other different forms of carbon worth mentioning are carbon nanotubes (CNTs) and graphene. Both materials have been widely studied as electrode material for supercapacitors.

Carbon nanotubes (CNTs) can be conceptualized as seamless hollow tubes rolled up from two-dimensional (2D) graphene sheets with diameters in the nanometer range and lengths usually on the micron scale. They have proven themselves promising electrode materials in energy storage due to their unique properties, such as structure (one-dimensional geometry), high surface area, high electrical conductivity, as well as light weight (Bordjiba et al., 2008; Zhang et al., 2008). The advantages of using CNTs is that they form a more open porous structure due to the central hollow canal that enables easy access of ions from electrolyte. However, because the pristine CNTs mainly possess electric double-layer capacitance and they usually have lower surface area ($< 500 \text{ m}^2 \text{ g}^{-1}$) in comparison to ACs (Zhang & Zhao, 2009), their specific capacitance is only up to 80 F g^{-1} (Meng et al., 2009). So they are usually modified before use as electrode (Cherusseri & Kar, 2015; Li et al., 2004).

Graphene, another allotrope of carbon, is a single layer of carbon atoms arranged into a 2D honeycomb lattice. Graphene has attracted the interest of researchers because of its fascinating properties that includes: high theoretical surface area that reaches up to $2630 \text{ m}^2 \text{ g}^{-1}$ for a single graphene sheet, exceptional high thermal conductivity, superior mechanical strength, high electron mobility at room temperature ($2.5 \times 10^5 \text{ cm}^2 \text{ V}^{-1} \text{ s}^{-1}$), as well as its high electrical conductivity (10^6 S cm^{-1}) making it an attractive candidate for use as EDLC (Allen et al., 2010; Chang & Wu, 2013; Stoller

et al., 2008). Graphene is a 2D building material for carbon materials of all other dimensionalities. It can be wrapped up into 0D buckyballs, rolled into 1D carbon nanotubes or stacked into 3D graphite as shown in **Figure 2.7**.

In summary, carbon-based materials with high surface area and suitable porous structure are good candidates as electrode materials for double layer supercapacitors, however, these materials generally have lower specific capacitance values compared to pseudocapacitor electrode materials (Li et al., 2011). Therefore, other than being used directly as electrode material, carbon-based materials are widely used to form composite with pseudocapacitors to improve the electrochemical properties of the electrode.

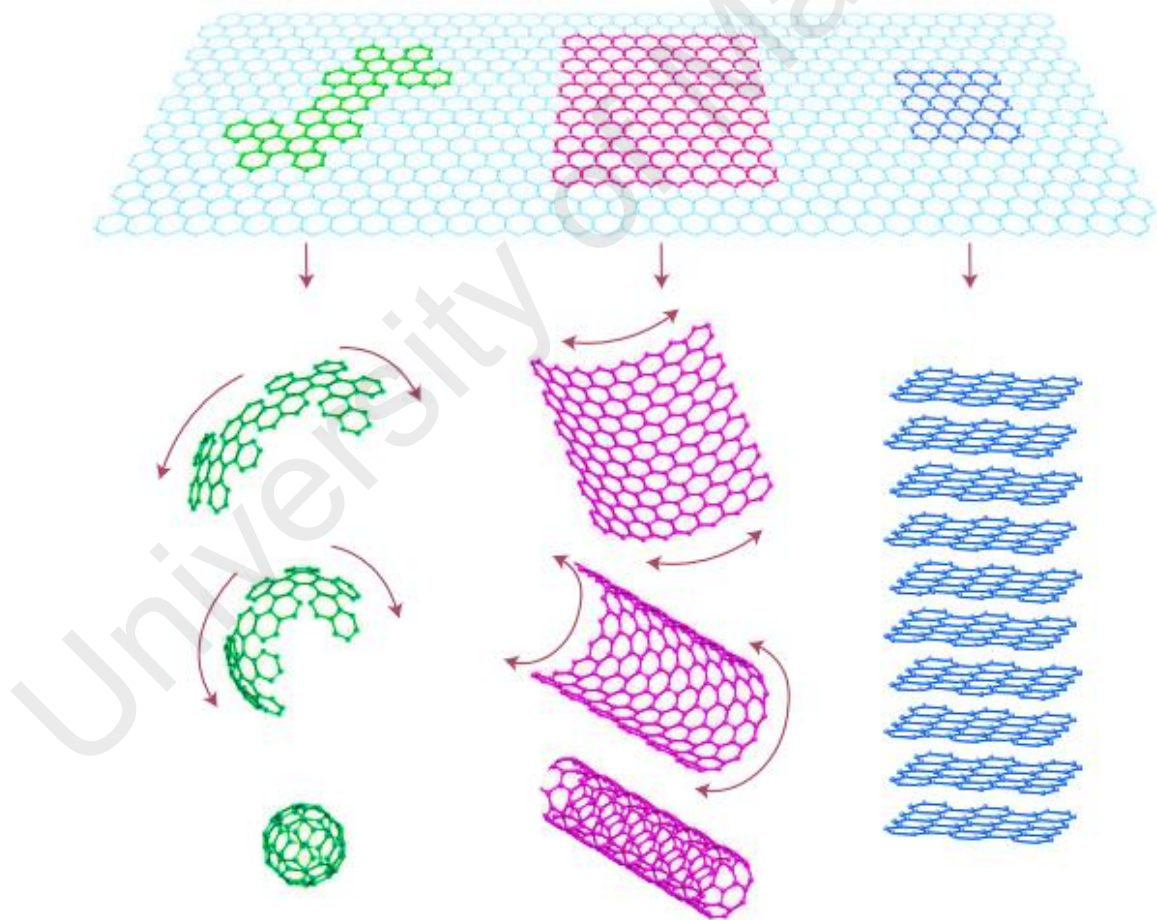


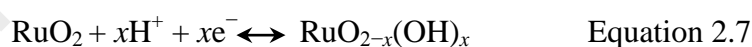
Figure 2.7: Evolution of 2D carbon (graphene) into different building blocks of materials; buckyball, CNTs and graphite (Geim & Novoselov, 2007).

2.4.2 Transition Metal Oxides

A number of transition metal oxides with various oxidation states represent a type of attractive materials for supercapacitors owing to the outstanding structural flexibility and the high specific capacitance. The energy storage of transition metal oxides are predominantly based on the reversible Faradaic reaction on the surface of the oxides in addition to some electric double-layer storage. Ruthenium oxide, manganese oxides, nickel oxide and cobalt oxide have been investigated as electrode material for supercapacitor applications.

2.4.2.1 Ruthenium oxide

Ruthenium oxide (RuO_2) is one of the promising materials for pseudocapacitors. It can achieve a high specific capacitance ($> 700 \text{ F g}^{-1}$) in acidic electrolyte due to its intrinsic high electrical conductivity, low ESR, fast and reversible electron transfer (Hu et al., 2007; Pusawale et al., 2013). The electro-adsorption of protons on the surface of RuO_2 according to the **Equation 2.7**, where Ru oxidation states can change from (II) up to (IV):



RuO_2 has a broad potential window of about 1.2 V that is achieved through the continuous proton insertion or de-insertions (Simon & Gogotsi, 2008). However, the drawback of RuO_2 is its high production cost expensive, toxic in nature, and requires a strongly acidic electrolyte (Chang et al., 2008). These drawbacks have caused researchers to search for cheaper and “greener” alternatives electrode materials.

2.4.2.2 Manganese oxides

Manganese oxides (MnO_x) has drawn the attention of researchers because of its great abundance in nature, low cost, high theoretical specific capacitance, environmental friendliness, and satisfactory capacitance performance in mild electrolytes, which have made it a promising electrode material for pseudocapacitors (Wei et al., 2011; Zhang & Chen, 2009). The pioneering work on the pseudocapacitive behavior of manganese oxides were reported in 1999 by Lee and Goodenough. The manganese oxide was prepared by a co-precipitation method using potassium permanganate and manganese acetate (Lee & Goodenough, 1999). The synthesized manganese oxide was found to have a surface area of $303 \text{ m}^2 \text{ g}^{-1}$ and displayed a specific capacitance of about 200 F g^{-1} . This study paves the way to use manganese oxides as electrode materials for supercapacitor applications and received much attention since then. The Faradaic reactions of manganese oxide can occur on the surface and in the bulk of the electrode. The surface redox reaction involves the surface adsorption of electrolyte cations ($\text{C}^+ = \text{H}^+, \text{Li}^+, \text{Na}^+, \text{and } \text{K}^+$) on the manganese oxide (Toupin et al., 2004):



On the other hand, Faradaic reactions the takes place in the bulk of the electrode rely on intercalation and deintercalation of electrolyte cations (Bahloul et al., 2013):



As a transition metal, manganese can have various oxidation states and has a variety of stable oxides (MnO , Mn_3O_4 , Mn_2O_3 , MnO_2) (Wei et al., 2011). Structural parameters such as morphology, porosity and textures, defect chemistry and particle size play a crucial role in determining and optimizing the electrochemical performances

of manganese oxides. Therefore, a variety of preparation methods have been developed to synthesize manganese oxides as supercapacitor electrodes.

Various morphologies of have been explored through a variety of synthesis methods to improve the specific capacitance of MnO_2 . Microwave-assisted reflux synthesis was used to synthesis MnO_2 nanoparticles and MnO_2 urchin-like nanostructures (Zhang et al., 2013). MnO_2 nanoparticles were obtained when synthesized in neutral conditions, but when the experimental was carried out in acidic conditions, MnO_2 urchin-like nanostructures with a diameter of 1-2 μm were obtained instead. The specific capacitances for MnO_2 nanoparticles and urchin-like nanostructures were 311 and 163 F g^{-1} , respectively. Cactus-like porous MnO_2 have been prepared by Dai et al. by using sodium dodecyl sulfate (SDS) as surfactant in the hydrothermal process (Dai et al., 2015). The SDS acted as a morphology controlling agent to produce porous MnO_2 with cactus-like structure, producing a surface area of 321.9 $\text{m}^2 \text{g}^{-1}$ and specific capacitance of 188 F g^{-1} . The porous morphologies are able to enhance the electrochemical performance of MnO_2 by providing high surface area and providing shorter ions paths and faster charge transfer kinetics.

The main challenge posed by using MnO_2 as the electrode material for supercapacitors is the MnO_2 loading, due to poor electrical conductivity of MnO_2 . As a result, the specific capacitance decreases when thicker films or higher loading of MnO_2 are prepared. For example, thin films of MnO_2 were prepared by sol-gel method (Pang et al., 2000). The film thickness and calcination temperature affect the specific capacitances of the thin films. The specific capacitances of the thin films dropped from 700 to 200 F g^{-1} when the film thickness increased from tens of nanometers to several micrometers, indicating only a thin layer of MnO_2 was involved in the capacitive reaction process. Zhi et al. showed that when the manganese oxide loading is low, higher specific capacitance can be achieved (Zhi et al., 2012). The calculated specific

capacitance of MnO₂ shell on the carbon nanofiber substrate reached 900 F g⁻¹ at 39% of oxide loading but when the entire mass of electrode is considered together, the specific capacitance at the same oxide loading was only ~225 F g⁻¹. This was due to the fact that when the oxide coating is too thick, it will cause part of the material to be electrochemically inactive, jeopardizing the charge transport. Wang et al. also showed similar findings about the relationship between mass loading and specific capacitance. When the MnO₂ loading was increased from 0.33 to 3.41 mg cm⁻², the specific capacitance decreased linearly from 539 to 188 F g⁻¹ (Wang et al., 2011).

The enhancement of the electrical conductivity and charge storage capability of MnO₂ have also been extensively studied. CNTs are widely used to form composites with MnO₂ due to its high surface area, high electrical conductivity and open porous structure for enhanced electrolyte accessibility. MnO₂/CNT was formed when the CNT film electrode is immersed in ethanol (as a reducing agent) while KMnO₄ solution was added dropwise to form a thin layer of MnO₂ (Li & Wei, 2012). The hybrid electrode delivered a specific capacitance of 150 F g⁻¹. KMnO₄ can also be reduced to MnO₂ on CNT under acidic solution, without the use of any reducing agent as showed by Wang et al. This facile synthesis method to prepare MnO₂/CNT showed a specific capacitance of 162 F g⁻¹ and excellent charge/discharge property with 90% capacitance retention after 2000 cycles (Wang et al., 2011).

Similarly, graphene is also commonly used for making MnO₂ composites due to its high surface area and conductivity. For example, graphene decorated with flower-like MnO₂ nanostructures showed remarkable chemical stability and electrical conductivity. The MnO₂ nanoflowers were coated onto the graphene electrodes via electrodeposition and gave a specific capacitance of 328 F g⁻¹ (Cheng et al., 2011). Ge et al. fabricated MnO₂/graphene nanostructured sponges by a series of dip coating steps (Ge et al., 2013). The sponges were firstly dipped into the graphene oxide solution and

then immersed into hydroiodic acid to reduce the graphene oxide. Then MnO_2 were deposited onto the sponges by dipping into a solution of manganese acetate followed by KMnO_4 solution as shown in **Figure 2.8**. The sponge@RGO@ MnO_2 composite achieved a high specific capacitance of 450 F g^{-1} due the synergetic combination of EDLC and pseudocapacitive MnO_2 combined with the porous sponge framework.

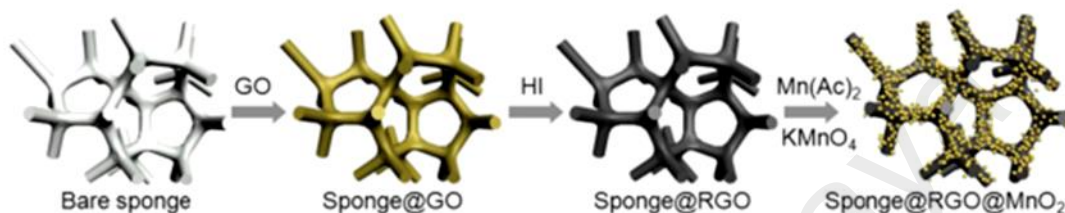


Figure 2.8: Schematic illustration of the dip coating process for the synthesis of sponge@RGO@ MnO_2 (Ge et al., 2013).

In short, MnO_2 are attractive candidates for supercapacitors applications. However, the high specific capacitance values ($> 400 \text{ F g}^{-1}$) are mostly based on extremely thin films and/or low oxide loading of MnO_2 , which can easily lead to an overstatement of a material's performance (Wang et al., 2011). When very minute amounts of materials are used, the overall capacitances contributed by other cell components such as the electrode support surface, collector and other conducting surface might become significant and overshadow the capacitance contributed by the active material (Stoller & Ruoff, 2010).

2.4.3 Electrically Conducting Polymers

The discovery of “metal-like” electrically conducting polymers (ECPs) has given rise to the field of electrochemical polymer science and they appear as a potent choice as electrode material for pseudocapacitance. The energy density and capacitance of ECPs is higher than that of EDLC composed of carbon materials because conducting polymers can store charge not just in the electrical double layer but predominantly through the fast Faradaic redox reactions. ECPs have several advantages over transition metal oxides; which also come from a family of pseudocapacitors. ECPs offer fast charge-discharge kinetics, relatively low cost compared to metal oxides and have good intrinsic electrical conductivity (Patil et al., 2013; Ryu et al., 2002). Due to their unique and interesting properties, a large number of recent publications have reported on the synthesis and electrochemical properties of ECPs and their derivatives. However the main drawback of ECPs is their poor stability during cycling when used as bulk materials, and therefore limited cycle life. The conducting polymers films undergo swelling, shrinking, cracking or breaking during the doping/dedoping process of continuous charge-discharge processes and as a consequence, gradually aggravate their conducting properties. (Frackowiak et al., 2006; Simon & Gogotsi, 2008)

The ECPs that are commonly used as pseudocapacitors are polyaniline (PANi), polypyrrole (PPy) and polythiophene (PTh) and poly(3,4-ethylenedioxythiophene) (PEDOT). The general structure of all ECPs consist of a regularly alternating single (C-C) and double (C=C) bonds, forming a region of overlapping p-orbitals, bridging the adjacent single bonds. This will allow a delocalization of π -electrons across all the adjacent aligned p-orbitals, giving rise to a π -conjugated backbone throughout the polymer chains. The π -conjugated backbone is responsible for the generation and propagation of charge carriers, making the polymers intrinsically conducting. **Figure 2.9** shows the chemical structures of the above mentioned ECPs.

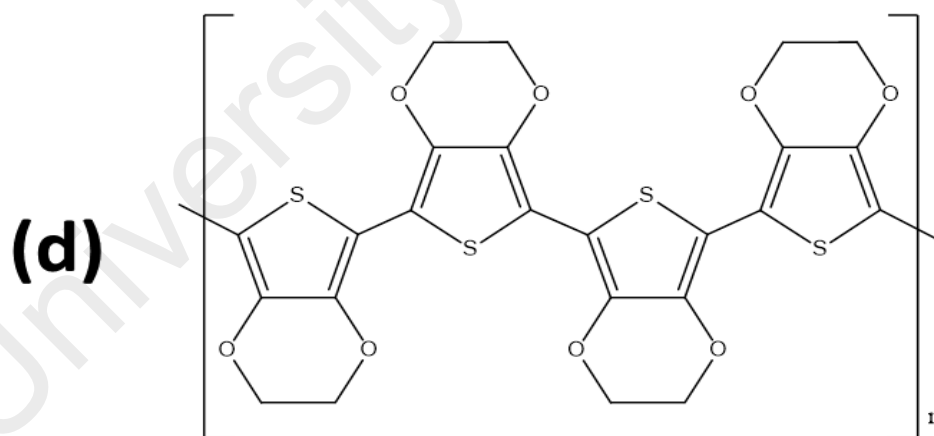
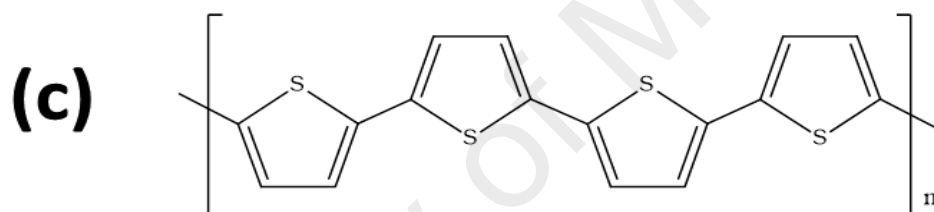
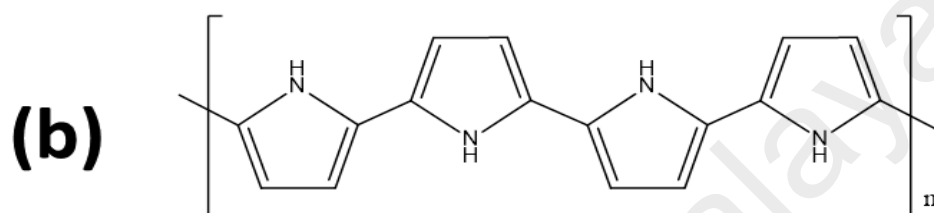
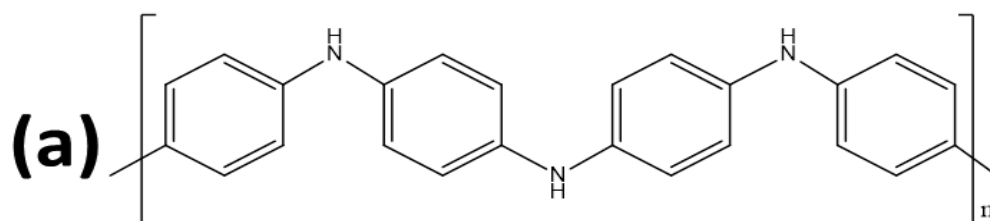


Figure 2.9: Chemical structures of some most common ECPs in their neutral states. (a) PANi, (b) PPy, (c) PTh, and (d) PEDOT

2.4.3.1 Polypyrrole (PPy)

Among the available ECPs, PPy is one of the most promising materials for pseudocapacitors due to its greater degree of flexibility in preparation processes, light weight, low cost and high electrical conductivity than most other commercially available ECPs (Hepowit et al., 2012). Moreover, the oxidation potential is lower for pyrrole (0.8V) than other heterocyclic monomers. In fact, PPy is one of the few ECPs that can be synthesized in aqueous solutions. The preparation of PANi requires acidic aqueous media while PTh must be grown from organic solvents. These made PPy stood out from the rest of the other ECPs (Ansari, 2006).

There are two commonly used polymerization techniques, chemical polymerization and electrochemical polymerization. The main advantage of chemical synthesis of PPy is the ease of mass production, but the PPy product is always present in powder form. The powdered sample requires the use of insulating binder in the fabrication of electrode that would disrupt the electron transport of the electrode and subsequently affecting the overall performance of the electrode (Ghosh et al., 2011; Wang et al., 2011). Electrochemical polymerization is generally preferred because it gives cleaner polymers unlike chemical polymerization where unreacted reactants and residues are often mixed together with the polymer. Furthermore, electrochemical polymerization provides a better control of film thickness and morphology. The films formed from electrochemical polymerization are generally deposited onto a supporting electrode surface by anodic oxidation of the corresponding monomer in the presence of an electrolyte solution. This method is also a useful technique to eliminate the use of binders where the PPy can be directly grown on the freestanding substrate. Three electrochemical polymerization techniques are generally employed including potentiostatic (constant potential), galvanostatic (constant current) and potentiodynamic (cyclic voltammetry) methods (Sadki et al., 2000).

2.4.3.2 PPy and PPy/carbon-based composites for supercapacitors

To increase the electrochemical performance of PPy, different morphologies of PPy have been synthesized using either chemical or electrochemical synthesis methods. Morphologies such as PPy clusters, nanobricks and porous films have been made with various chemical and electrochemical methods.

Besides employing solely PPy as the electrode material for supercapacitors, many literatures also reported on compositing PPy with carbon materials that may synergistically enhance the performance of the PPy. Carbon materials such as carbon fibers, carbon aerogel, CNT, and graphene have proven to increase the specific capacitance by increasing the surface area and stability of the composite. The performance of PPy and PPy/carbon composites are summarized in **Table 2.1**.

Table 2.1: Summary of a selection of PPy and PPy/carbon-based composites for supercapacitors. Specific capacitance values are reported from three-electrode configuration unless otherwise stated.

Material	Description	Specific capacitance (F g^{-1})
PPy nanobricks (Dubal et al., 2011)	PPy nanobricks were synthesized by potentiostatic electrodeposition at 0.9 V with aqueous bath containing pyrrole and KNO_3 .	476 (CV at 5 mV s^{-1} , electrolyte: 0.5 M H_2SO_4 .)
PPy films (Muthulakshmi et al., 2006)	PPy films were fabricated by galvanostatic electrodeposition with current density of 0.36 mA cm^{-2} for 300 s.	354 (CV at 1 mV s^{-1} , electrolyte: 1 M KCl)

PPy clusters (Dubal et al., 2012)	Porous clusters of PPy were prepared under potentiodynamic electrodeposition from 0 to 1.2 V under different scan rate to give different porous morphologies. Nanobelts, nanobricks and nanosheets have been synthesized under scan rates of 50, 100 and 200 5 mV s ⁻¹ , respectively.	586 (CV at 2 mV s ⁻¹ , electrolyte: 0.5 M H ₂ SO ₄)
PPy films (Du et al., 2013)	Highly stable PPy films fabricated by unipolar pulse electropolymerization method. The short on-time pulse and low temperature showed PPy films with reduced chain defects.	406 (CV at 5 mV s ⁻¹ , electrolyte: 1 M KCl)
PPy/vapor grown carbon fibers (Kim et al., 2006)	PPy layers were deposited on vapor grown carbon fibers. The thickness of the deposited PPy layers is controlled by the concentrations of pyrrole used.	588 (CV at 30 mV s ⁻¹ , electrolyte: 6 M KOH)
PPy/carbon aerogel (An et al., 2010)	PPy/carbon aerogel composite was prepared by chemical oxidation polymerization through ultrasound irradiation using sodium dodecyl sulfate as the surfactant.	433 (CV at 1 mV s ⁻¹ , electrolyte: 6 M KOH)
PPy/CNT (Li & Zhitomirsky, 2013)	Pyrocatechol violet dye was used as an anionic dopant and to increase the adhesion of PPy/CNT films on Ni substrates.	390 (CV at 2 mV s ⁻¹ , electrolyte: 0.5 M Na ₂ SO ₄)

PPy/ graphene (Lim et al., 2013)	One-step electrochemical for the synthesis of PPy/graphene composite from electrolyte solution containing pyrrole, graphene oxide and sodium p-toluenesulfonate. The synergistic effect between PPy and graphene enhanced the electrochemical performance of the nanocomposite.	300 (CV at 10 mV s^{-1} , electrolyte: 1 M Na_2SO_4)
---	---	--

2.4.3.3 PPy/MnO₂ composites for supercapacitors

Another common option to increase the performance of PPy is by the incorporation of transition metal oxides. As discussed earlier, MnO₂ is transition metal oxide that can also exhibit pseudocapacitance; hence, the composites of PPy and MnO₂ are expected to have higher capacitances values than its constituents PPy and MnO₂ alone as proven in many studies. PPy/MnO₂ composites will be discussed more in detail in the following review compared to previously discussed PPy/carbon composites given their relevance to this thesis.

PPy/MnO₂ composites for supercapacitors electrodes have evoked great interest of researchers worldwide. The combination of both classes of pseudocapacitors certainly has their advantages. The composites take advantage of the high electrical conductivity of PPy and the high energy storage capacity of MnO₂. With the elegant synergy between both materials, remarkable electrochemical performances can be realized.

Core/shell structures of PPy/MnO₂ have been synthesized by few researchers without the use of surfactant or additional oxidant (Wang et al., 2014; Yao et al., 2013). The MnO₂ nanotubes were firstly synthesized via hydrothermal method, followed by *in situ* polymerization of pyrrole monomers. The MnO₂ nanotubes acted as both template and oxidant to initiate the polymerization of pyrrole monomers. The core/shell structure consists of PPy as the shell and MnO₂ nanotubes as the core as shown in **Figure 2.10**. The PPy/MnO₂ reported by Yao et al., exhibited a specific capacitance of 380 F g⁻¹ and good capacitance retention of 90% of its initial capacitance after 1000 charge/discharge cycles while Wang et al. reported a maximum of specific capacitance of 337 F g⁻¹, and retained 88.8% of its initial capacitance in 1000 charge/discharge cycles as well. In both cases, the PPy/MnO₂ coaxial composites showed an enhancement of specific capacitance from the lone MnO₂ nanotubes and PPy. The synergistic effect between MnO₂ and PPy could inhibit the dissolution of MnO₂ and PPy, and consequently improve the electrochemical reversibility and stability of the composite electrode.

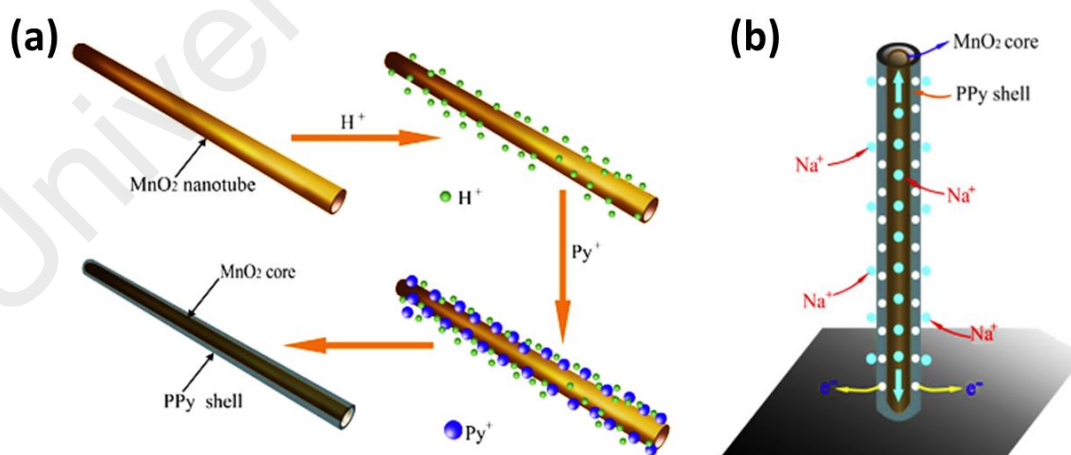


Figure 2.10: (a) Schematic illustration of the formation and (b) schematic charge storage advantage of the PPy/MnO₂ coaxial nanotubes (Yao et al., 2013).

Li et al. also prepared core/shell structures of PPy/MnO₂ but with PPy nanotubes acting as the core, in contrast to the above studies where MnO₂ nanotubes were employed as the core. PPy nanotubes were synthesized using methyl orange/FeCl₃ complex as a reactive self-degraded soft-template and oxidant. The embedment of MnO₂ nanoparticles onto the walls and pore channels of the PPy nanotubes forms the shell. The MnO₂ nanoparticles on the PPy nanotubes lead to more active sites that are susceptible to redox reaction to give a high specific capacitance of 328 F g⁻¹ at a current density of 3 mA cm⁻².

PPy-covered MnO₂ composites have also been explored, whereby MnO₂ nanoparticles are wrapped with PPy. Bahloul et al. first synthesized MnO₂ nanoparticles by hydrothermal method. The as-synthesized MnO₂ powders were pressed on a graphite current collector and was used as the working electrode for the electropolymerization of PPy (Bahloul et al., 2013). Specific capacitances of 74 and 142 F g⁻¹ were obtained for MnO₂ and PPy/MnO₂, respectively. However, this composite electrode only retained about 51% of its capacitance value after 500 cycles of charging/discharging, the low capacitance retention could be either due to the detachment of the electropolymerized PPy away from the MnO₂ or the weak adhesion of the PPy/MnO₂ on the graphite current collector. Zhang et al. also produced PPy/MnO₂ from similar routes except that the wrapping of PPy on MnO₂ was carried by chemical polymerization method. The MnO₂ was dispersed into a solution of pyrrole monomer with the molar ratio of 1:3 followed by the addition of FeCl₃ (oxidant) to obtain the composites. The calculated specific capacitance the PPy/MnO₂ composite is 353 F g⁻¹ and retained 91.2% of its initial capacitance after 100 charging/discharging cycles (Zhang et al., 2013).

Up to now, the discussions of PPy/MnO₂ composites still requires a two-step process. Researchers are always opting for easier synthesis methods with fewer procedures that offer excellent potential for large-scale material production. Zang & Li

have demonstrated a facile, one-step, and *in situ* co-precipitation approach to synthesizing ultrafine β -MnO₂/PPy nanorod composite (Zang & Li, 2011). KMnO₄ acted as an oxidizing agent to oxidize the pyrrole monomers to PPy; at the same time the Mn⁷⁺ ions from KMnO₄ was reduced to Mn⁴⁺ ions in the form of MnO₂. Although β -MnO₂ has been regarded as the undesirable candidate for supercapacitor applications, the β -MnO₂/PPy nanocomposite still exhibited fairly high specific capacitance of 340 F g⁻¹. The key is the size of the ultrafine β -MnO₂ particles (< 10 nm in diameter) that behaves differently at the nanoscale level. The ultrafine β -MnO₂ particles were achieved with the aid of PPy, which sheathed the β -MnO₂ crystal, effectively prevented it from further growing.

Sharma et al. have also fabricated PPy/MnO₂ nanocomposites via a one-step electrodeposition under constant current (Sharma et al., 2008a). The nanocomposites were formed from a deposition bath containing MnSO₄, H₂SO₄ and pyrrole monomer. The electrodeposition process involves the simultaneously process of the electropolymerization of PPy and the anodic oxidative deposition of Mn²⁺ to Mn⁴⁺ (MnO₂). The porous PPy matrix provides high surface area for the dispersion of MnO₂ nanoparticles. On the other hand, the MnO₂ nanoparticles nucleated over the polymer chains enhanced the conductivity and stability of the nanocomposite material by interlinking the PPy polymer chains. The PPy/MnO₂ nanocomposite thin film electrodes show significant improvement with specific capacitance of 620 F g⁻¹ in comparison with its constituents PPy (250 F g⁻¹) and MnO₂ (255 F g⁻¹). The PPy/MnO₂ was also made into supercapacitor device (two-electrode configuration) and gave a specific capacitance of 180 F g⁻¹ and retained 90% of its initial capacitance after 5000 charging/discharging cycles.

Table 2.2: Specific capacitance of a selection of PPy/MnO₂ composites reported in the literature. Specific capacitance values are reported from three-electrode configuration unless otherwise stated.

Reference	Comments	Specific capacitance (F g ⁻¹)	Electrolyte
(Yao et al., 2013)	Coaxial nanotubes, MnO ₂ nanotubes as core and PPy as shell. Surface morphologies can be varied by altering the concentrations of H ₂ SO ₄ .	380 (CV at 1 mV s ⁻¹)	1 M Na ₂ SO ₄
(Wang et al., 2014)	Coaxial nanotubes, MnO ₂ nanotubes as core and PPy as shell.	337 (GCD at 0.5 A g ⁻¹)	2 M KCl
(Li et al., 2010)	Coaxial nanotubes, with PPy nanotubes as core and MnO ₂ nanoparticles as shell. Methyl orange/FeCl ₃ complex acted as a reactive self-degraded soft-template and oxidant.	328 (GCD at 3 mA cm ⁻²)	1 M KCl
(Bahloul et al., 2013)	MnO ₂ nanoparticles wrapped with PPy. PPy was electropolymerized at 0.9 V vs SCE.	142 (GCD at 2 mA cm ⁻²)	1 M Na ₂ SO ₄
(Zhang et al., 2013)	MnO ₂ nanoparticles wrapped with PPy. PPy was formed via chemical polymerization using FeCl ₃ as oxidant.	353 (GCD at 8 mA cm ⁻²)	0.5 M Na ₂ SO ₄
(Zang & Li, 2011)	One-step, <i>in situ</i> synthesis of ultrafine β-MnO ₂ /PPy nanorod composite. The insoluble PPy hinder the further	340 (GCD at 0.2 A g ⁻¹)	1 M Na ₂ SO ₄

	crystal growth of β -MnO ₂ .		
(Sharma et al., 2008a)	One-step electrodeposition of PPy/MnO ₂ . PPy was used as support for MnO ₂ to grow whilst MnO ₂ improved the chain structure and stability of the PPy.	620 (CV at 5 mV s ⁻¹) 180 (GCD at 2 mA cm ⁻² , two-electrode setup)	0.5 M Na ₂ SO ₄

2.4.3.4 PPy/Chitosan composites

At the moment, no previous works done on PPy/CS composite for supercapacitor applications. The closest work to supercapacitor applications have been conducted by Yalçinkaya *et al.* where they reported the electrochemical synthesis of PPy/CS composite with improved thermal stability. Electrochemical measurements including CV have shown that the PPy/CS composite is very stable and extremely electroactive. However, this study was limited to the synthesis and characterization of the PPy/CS composite without any application studies (Yalçinkaya et al., 2010).

There have been many reported works on PPy/CS for various applications which worth mentioning. PPy/CS composite fibers were fabricated by Liu *et al.* through the polymerization of pyrrole on CS fibers, in which CS fibers were pre-synthesized *via* wet spinning method (Liu et al., 2015). An interesting work done by Qi *et al.* show that the PPy/CS conductive composite supported cell adhesion, spreading, and significantly enhanced the proliferation of olfactory ensheathing cells with or without electrical stimulation. These findings highlight the possibility of enhancing nerve regeneration in

conductive scaffolds (Qi et al., 2013). Lee *et al.* have reported the formation of suspensible PPy/CS membranes in diluted acetic acid solutions produced by the chemical polymerization of pyrrole in CS solution using ammonium persulfate as the oxidation. The antioxidant properties of these membranes were found renewable by means of electrochemical cycling (Lee et al., 2013).

2.5 Modifications of Electrode Material

Increasing the electrical conductivity of electrode materials is often desirable to boost the electrochemical performances. Combining pseudocapacitor materials with carbon-based materials such as CNT and graphene can contribute to the double layer capacitance and at the same time improves the electrical conductivity of the electrode materials as discussed previously. Alternatively, silver (Ag) metal is also used to boost the electrical conductivity of electrode materials. The introduction of highly conductive Ag into various electrode materials does not only enhances the conductivity, but also the thermal, optical, mechanical properties resulting in a new class of important materials suitable for various applications (Dhibar & Das, 2014).

MnO₂ nanowire/Ag nanocomposites were prepared Dao et al. The Ag nanoparticles were acquired on the MnO₂ nanowires by reducing Ag⁺ with sodium borohydrate (Dai et al., 2014). The role of Ag nanoparticles improved the electrical conductivity and also the structural stability of the nanocomposite. As a result, high specific capacitance of 396 F g⁻¹ was measured with 95.2% of capacitance retention over 2000 charge/discharge cycles. Zhi et al. had synthesized a highly conductive ordered mesoporous carbon (OMC) based electrode decorated by 3D graphene and 1D Ag nanowire (Zhi et al., 2014). The novel architecture of Ag/Graphene/OMC exhibited ultra high electrical conductivity up to 741 S cm⁻¹. The material was assembled into a

symmetric supercapacitor (two-electrode configuration) and yielded a specific capacitance of 213 F g^{-1} , which is higher than that of graphene/OMC (139 F g^{-1}) and pristine OMC (36 F g^{-1}). The exceptionally high electrical conductivity served as a highway for electron transfer resulting in good electrochemical performance of the material.

Ag nanoparticles-decorated PANi/CNT was fabricated via a typical *in situ* chemical polymerization (Dhibar & Das, 2014). The nanocomposite showed increased electrical conductivity and a specific capacitance of 528 F g^{-1} . The nanocomposite also showed better thermal stability up to $350 \text{ }^\circ\text{C}$. Patil et al. synthesized PPy/polyacrylic acid (PAA)/Ag composite for supercapacitor application (Patil et al., 2013). The PPy/PAA/Ag thin films were obtained by immersing the stainless steel substrates into a solution mixture of PPy, PAA and silver nitrate. The highest capacitance of 226 F g^{-1} was obtained for the PPy/PAA/Ag composite electrode.

The hydrophilic nature of an electrode material is extremely important as the interaction between the electrolyte and electrode material is the basis for charge storage either electrostatically (non-Faradaic) or pseudocapacitively (Faradaic). There have been a number of studies dedicated to study the correlation between the hydrophilicity of an electrode material and its electrochemical properties. Erdenedelger et al. functionalized graphene with amino acid to make graphene/PANi composites. The embedment of PANi particles on the modified graphene is prepared efficiently in an aqueous system due to the better dispersibility of the functionalized graphene (Erdenedelger et al., 2014). The composite displayed improved electrochemical performance of 290 F g^{-1} owing to the effective ion accessibility in an aqueous electrolyte. Superwetting monolithic carbon has been synthesized by treatment with 5 M nitric acid (HNO_3) and concentrated H_2SO_4 . It was found that monolithic carbon treated with HNO_3 and H_2SO_4 yield specific capacitances of 320 and 404 F g^{-1} ,

respectively, while that of untreated monolithic carbon was only 282 F g^{-1} . The H_2SO_4 treated sample had shown remarkable ability to improve protons conduction. The better electron exchange between the acidic electrolyte and carbon electrode material was due to the increment of proton mobility on the hydrophilic surface (Wang et al., 2012). The hydrophilic electrode surface can also enhance the redox reaction activity of metal oxide electrodes. Nickel oxide (NiO) thin films were electrodeposited onto stainless steel substrate. The NiO films surface with very fine elongated particles showed hydrophilic character due to the strong cohesive force between the water droplet and oxide of the NiO (Navale et al., 2015). The supercapacitive performance of the NiO electrode demonstrated a specific capacitance as high as 458 F g^{-1} .

2.6 Electrolytes for Supercapacitors

Electrolytes play a crucial role in determining the performance of supercapacitors. The electrochemical and physical properties of the electrolytes are the key factors of determining the equivalent series resistance (ESR) and the power output of supercapacitor cells (Lust et al., 2004). In addition, the operating voltage of an electrolyte is restricted by the decomposition potential of the electrolyte, which is important for determining the energy density of the supercapacitor. Common electrolyte systems for supercapacitors are separated into three types, aqueous, organic and ionic liquid electrolytes.

2.6.1 Aqueous Electrolyte

Aqueous electrolytes are popular due to their relatively high conductivity, low viscosity even in concentrated solutions, non-flammability and environmental friendliness. Acidic electrolytes such as H_2SO_4 are used extensively for porous carbon materials to achieve higher capacitance due to the participation of protons in the

pseudo-capacitive reactions for quinone groups on the surface. Similarly, alkaline electrolytes such as KOH will be involved in the Faradaic reactions with the pyrone functionalities on the surface of carbon materials (Andreas & Conway, 2006). Lee et al. showed that the specific capacitance values of reduced graphene oxide (RGO) tested in acidic and alkaline electrolytes were nearly the same (Lee et al., 2013). The specific capacitance of RGO in 1 M H₂SO₄ was calculated to be 193 F g⁻¹ whilst that in 1 M KOH was calculated to be 207 F g⁻¹.

However, acidic electrolytes cannot be used for manganese oxides (MnO_x) based materials due to the dissolution of MnO_x in acidic solutions (Cuentas-Gallegos & Gómez-Romero, 2005). Neutral electrolytes such as potassium chloride, sodium chloride and sodium sulfate are commonly used for MnO_x based electrode materials. In comparison, as electrically conducting polymers (ECPs) do not present the dissolution problems, or the pH dependent conductivity (except for PANi); there is more flexibility in terms of aqueous electrolyte choice for ECP systems.

The main drawback of aqueous electrolytes is their relatively narrow operating potential range, and consequently a lower energy storage density, which is limited by the potential window for the decomposition of water, i.e., 1.23 V. Hence, to avoid the decomposition of an electrolyte, an operating voltage of 0.8 – 1.0 V is often employed, resulting in low energy density.

2.6.2 Organic Electrolyte

Organic electrolytes have the merits of allowing supercapacitors to operate in the voltage range above 2 V due to the larger decomposition potential. Therefore, much higher energy density can be achieved for a given capacitance value. Non-aqueous

solvents such as acetonitrile and propylene carbonate are generally used to dissolve salts such as tetraalkylammonium and lithium perchlorate to produce organic electrolytes (Burke, 2007).

In general, the capacitance of activated carbons (ACs) is higher in aqueous electrolytes ($100 - 300 \text{ F g}^{-1}$) than that in organic electrolytes ($< 150 \text{ F g}^{-1}$), due to the larger size of the organic molecules. Moreover, the presence of moisture on the surface of the electrodes is responsible for the aging of the supercapacitor electrodes whenever organic electrolytes are used (Zhang & Zhao, 2009). The utilization of organic electrolytes also suffers from a number of issues such as incorporation of toxic and flammable organic solvents into supercapacitors and higher cost of electrolyte salts (Wei et al., 2012). Also, the purity of organic solvents can be an issue as slight water contamination (above 5 ppm) reduces the stability of voltage window significantly and accelerates the self-discharge process (Ricketts & Ton-That, 2000; Wang et al., 2012). As a result, strict controls in preparation process of these organic solvents are required. However, organic electrolytes are still being used in commercial supercapacitors because of the higher operating voltages, which offer a higher energy density (Zhang & Zhao, 2009).

2.6.3 Ionic Liquid Electrolyte

Ionic liquid electrolytes, also known as ionic liquids, are low melting point organic salts that exist as solvent free molten salt at room temperature. Since these electrolytes do not contain volatile organic compounds but only salts, they have high electrochemical stability that can operate up to 3 V (Frackowiak, 2007; Zhang & Zhao, 2009). Therefore, high energy density supercapacitors are achievable with the used of ionic electrolytes. Other attractive features of ionic electrolytes are high thermal

stability, non-flammability and very low vapor pressure. The disadvantages posed by utilization of ionic liquids are similar to that of using organic electrolyte; as they are usually less conducting and more viscous than aqueous electrolytes, which significantly hinders their penetration into the electrode structure and aggravates charge propagation (Fic et al., 2012).

2.7 Applications for Supercapacitors

2.7.1 Transportation

One vital application of supercapacitors is in regenerative brake systems that are often used in hybrid electric vehicles. Energy storage in transportation involves not only the propulsion (starting and stopping) of vehicles, but also secondary power requirements such as cruising power requirements of vehicles (Douglas & Pillay, 2005). In conventional brake system, brake pads produce friction with the brake rotor to slow or stop the vehicle, turning kinetic energy to heat. However, with the regenerative brake system, the vehicle's electric motor will enter a reverse mode upon braking, causing it to run backwards, and thus slowing the car's wheel. While running backwards, the motor will act as an electric generator, producing electricity which is transferred to the capacitor for storage. The electric energy stored is used to propel the vehicle or motor assistance mode, increasing the fuel efficiency of vehicles. **Figure 2.11** shows the mechanism of the regenerative brake system used by Mazda®, labelled as 'i-ELOOP' (intelligent energy loop) (<http://www.mazda.com/>). In real-world driving conditions with frequent acceleration and braking, the 'i-ELOOP' is able to improve fuel economy by approximately 10%.

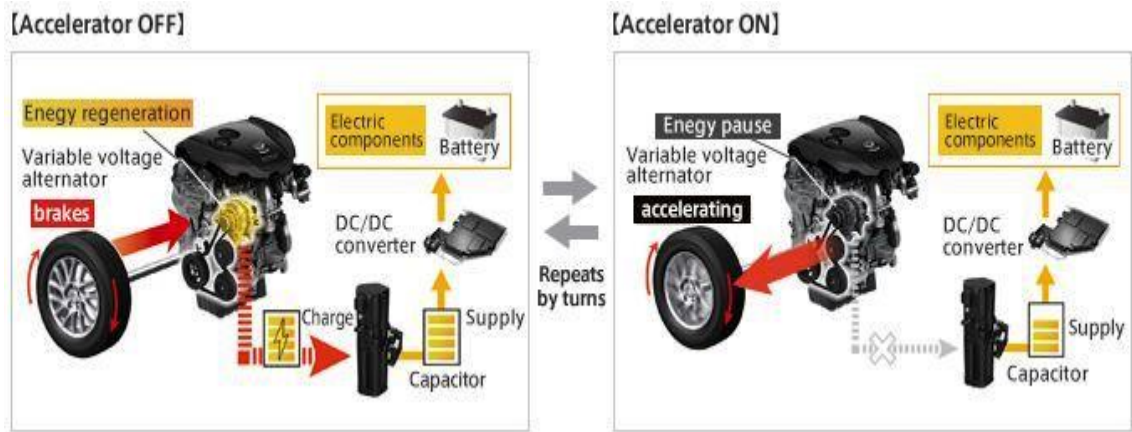


Figure 2.11: Mechanism of regenerative brake system employed in Mazda® (<http://www.mazda.com/>).

2.7.2 Stationary Electrical Energy Storage

Supercapacitors are useful as energy storage systems in microgrids and power grids. A power grid is an interconnected network consisting of generating stations that produce electrical power, high-voltage transmission lines and distribution lines to consumers whereas a microgrid is a small-scale power grid that can operate independently or in conjunction with the area's main power grid. Supercapacitors are useful in ensuring grid stability by absorbing the energy and releasing it at the right time to prevent dropouts, especially when the power generation are from intermittent renewable energy sources. As an increased amount of intermittent renewable energy such as solar and wind penetrates the grid, the output becomes increasingly unstable. It is very important to increase the reliability and efficiency of using these renewable energy sources. By using supercapacitors, the power quality problem in distributed power generation (e.g. voltage fluctuation) can effectively be solved (Cheng et al., 2006). Maxwell Technologies® provides supercapacitors to address this exact issue that are capable to fill in short-term power intermittencies and provide ramp rate control for longer intermittencies.

2.7.3 Portable Power Systems

Supercapacitors have also been used as energy backup supplies in consumer appliances. The supercapacitors are still able to provide energy to the system in the case of power outages, where there is a brief interruption in power supply. The use of supercapacitors is better than batteries because they can deliver much higher voltage in a limited amount of time. Moreover, supercapacitors have longer lifetime as compared to batteries. This means that supercapacitors do not need to be replaced regularly, effectively reducing the cost of appliances (Lai et al., 1992). Since then, energy backup systems for consumer electronic products are one of the biggest markets for supercapacitors.

Batteries are generally poor at power delivery whereas supercapacitors suffer from low energy density to sustain peak load for long periods of time. Hence, by combining supercapacitors and batteries, their drawbacks are minimized. The use of supercapacitors in parallel with batteries will smooth out the severe load demand of batteries by meeting the peak power requirements, whilst the batteries supply the average load (Kuperman & Aharon, 2011). The decreased of pulsed current drawn from the battery results in an extended battery lifetime. This combination is particularly useful in portable power tools where peak current demand is high. Applications of supercapacitor can easily be found in satellite TV (TV-channel setting and clock time), car audio systems (radio station memory), coffee machines (programmed functions), programmable pocket calculators, camera flash and toys, etc. (Goodenough et al., 2007).

CHAPTER 3

MATERIALS AND METHODOLOGY

3.1 Materials

Materials and chemicals used in this thesis are summarized in **Table 3.1**

Table 3.1 Materials and chemicals used in this thesis

Materials/Chemicals	Formula	Purity (%)	Supplier
Pyrrole	C ₄ H ₅ N	99	Acros Organics
Potassium permanganate	KMnO ₄	99.9	R&M Chemicals
Silver nitrate	AgNO ₃	99.9	Bendosen
Chitosan (Molecular weight: 100,000 – 300,000)	(C ₆ H ₁₁ NO ₄) _n	-	Acros Organics
Sodium p-toluenesulfonate	NapTS	98	Merck
Acetic acid – glacial	CH ₃ COOH	99.8	System
Sodium sulfate	Na ₂ SO ₄	99.5	Merck
Sulfuric acid	H ₂ SO ₄	95 – 98	System
Nickel foam	-	-	American Elements
Graphite sheet	-	-	Latech

3.2 Synthesis method

3.2.1 Synthesis of PPy/MnO₂ nanocomposites

The PPy/MnO₂ nanocomposites were prepared by the in-situ reaction between pyrrole and KMnO₄ in different pH solutions. First, pyrrole monomer (0.21 mL) was dissolved in 20 mL of 0.15 M NapTS. The pH of the solution was adjusted using H₂SO₄ to the desired pH value. Then, 10 mL of 0.03 M KMnO₄ solution was added to the above solution to obtain the final concentrations of 0.1 M pyrrole, 0.1 M NapTS and 0.01 M KMnO₄. The mixture was stirred vigorously for 60 min under ambient conditions. Finally, the PPy/MnO₂ nanocomposite was centrifuged, washed with deionized (DI) water, and dried in an oven at 60 °C.

3.2.2 Synthesis of PPy/CS composite electrodes

The PPy/CS electrodes were prepared by electrochemical polymerization. Briefly, different amounts of CS powder were dissolved in 20 mL of 1% acetic acid to obtain the CS solutions. Then, 10 mL of 0.3 M of pyrrole and NapTS in 1% acetic acid were added into the CS solution, to make up a deposition solution that consisted of 0.1 M of pyrrole, 0.1 M of NapTS and different amounts of CS content (0.5, 0.625, 0.75, 0.875, 1.0 wt%). A piece of graphite sheet (2 x 1 cm) was immersed into the deposition solution and the PPy/CS was deposited at a constant bias of +0.8 V. All potentials were referenced to a saturated calomel electrode (SCE) and a platinum wire was used as the auxiliary electrode. The deposition was stopped when the accumulated charge reaches 4 C and the sample-coated electrodes were rinsed with water to ensure removal of unbound materials. The mass of the deposited material was in the range of 2.0-2.4 mg. The as-prepared electrodes were denoted as PPy/CS-*x*, where *x* depicts the weight

percentage of the CS used in the deposition solution. When only PPy/CS is mentioned, it is prepared at 0.75 wt%.

3.2.3 Synthesis of Ag@PPy nanocomposites

The Ag@PPy nanocomposites were prepared by the *in-situ* reaction between pyrrole and AgNO₃ followed by electrochemical polymerization from an aqueous solution placed in a one-compartment cell. The deposition solution that contained 0.1 M pyrrole, 0.1 M NapTS and 0.05 M AgNO₃, was stirred vigorously for 5 min to allow the redox reaction between the pyrrole and Ag⁺. A piece of graphite sheet (1 x 1 cm) was then immersed into the deposition solution and the Ag@PPy was deposited at a constant potential of +0.8 V. All the potentials were referenced to a saturated calomel electrode (SCE) and a platinum wire was used as the auxiliary electrode. The deposition was stopped when the accumulated charge reaches 4 C with a mass loading of ~2.3 mg. The as-prepared electrodes were denoted as *x*M-Ag@PPy, where *x* depicts the concentration of the AgNO₃ used. When only Ag@PPy is mentioned, it is prepared at 0.05 M.

3.2.4 Synthesis of Ag@PPy/CS composite electrode

The Ag@PPy/CS nanocomposite electrode was electrochemically deposited from an aqueous solution placed in a one-compartment cell. The deposition solution contained 0.1 M NapTS, 0.1 M pyrrole, 0.05 M AgNO₃ and 0.75 wt% CS. Prior to electrodeposition, the deposition solution was stirred for 5 min to allow the redox reaction between the pyrrole and Ag⁺. A piece of graphite sheet (2 x 1 cm) was used as the substrate for the deposition of Ag@PPy/CS. Electrodeposition was carried out at a potential of +0.8 V until the total accumulated charge reaches 4 C. All potentials were

referenced to a saturated calomel electrode (SCE) and a platinum wire was used as the auxiliary electrode. Then, the as-synthesized electrodes were rinsed with water to ensure removal of unbound materials. For comparison, PPy, Ag@PPy and PPy/CS electrodes were also prepared. The mass of the deposited material was in the range of 2.0-2.4 mg

3.3 Characterization techniques

3.3.1 X-ray diffraction (XRD)

X-ray diffraction (XRD) takes advantages of the coherent scattering of x-ray of crystalline materials to acquire a wide range of crystallographic information. The samples in this work were analysed using XRD (Siemens D5000) with monochromatic Cu K α radiation ($\lambda = 1.5406 \text{ \AA}$) operated at 40 kV and 40 mA with a scanning speed of 0.02 degrees s^{-1} , scanning from 5-80°. The atomic structure was analysed using the PANanalytical X'pert Highscore software.

3.3.2 Fourier transform infrared spectroscopy (FT-IR)

A FT-IR is a technique employed to identify the types of chemical bonds (functional groups) in a molecule by producing an infrared absorption spectrum. In infrared spectroscopy, infrared radiation is passed through a sample and some of the infrared spectrum is absorbed by the chemical bonds and some of it is transmitted. The resulting spectrum represents the molecular absorption and transmission, creating a molecular fingerprint of the sample. In this work, infrared absorption spectrum was recorded on a Perkin-Elmer FTIR spectroscopy 1725x.

3.3.3 Raman spectroscopy

Raman spectroscopy is a spectroscopic technique that relies on the inelastic scattering (Raman scattering) of monochromatic light (from laser source) interacting with a sample. Photons from the laser light are absorbed and then re-emitted by a sample. The reemitted photons are shifted up or down (Raman shift) in comparison with the original monochromatic frequency thus providing useful information about vibrational, rotational and other low frequency transition in the molecules. Raman is commonly employed in assessing molecular motion and fingerprint of species. In this thesis, Raman spectra were recorded using a Renishaw inVia Raman microscope with green laser excitation (514 nm). The measurements were scanned from in the range of 800 –2000 cm^{-1} . The peaks obtained from the spectrum will give the information about the molecular structure of the sample.

3.3.4 X-ray photoelectron spectroscopy

X-ray photoelectron spectroscopy (XPS) is used to measure the elemental composition, chemical stoichiometry, chemical state and electronic state on the element that presence in the samples. X-ray is used as the light source for the excitement of the electrons that bond in the inner core-level orbitals. The bonding energy of the photoelectrons will provide the information of material where the electron is escaped. In this study, XPS measurements were performed using synchrotron radiation from beamline no. 3.2 at the Synchrotron Light Research Institute, Thailand.

3.3.5 Surface area analysis

The surface area is measured by N₂ adsorption analysis, in which the sample is exposed to N₂ gas of different pressures at a given temperature. The increment of pressure results in increased amount of N₂ molecules adsorbed on the surface of the sample to obtain an adsorption isotherm. When the pressure is systematically decreased to induce desorption of the adsorbed N₂ molecules, a desorption isotherm is obtained. The analysis of the adsorption and desorption isotherms in combination with some physical models yields information about the pore structure of the sample such as surface area, pore volume, pore size and surface nature. The N₂ sorption/desorption was carried out at a Micromeritics TrisStar II 3020 analyzer. The sample was degassed at 130 °C for 5 h in vacuum before the measurement. Specific surface area was determined by using the Brunauer-Emmett-Teller (BET) model. The pore volume and pore size distributions were obtained using the Barrett-Joyner-Halenda (BJH) method.

3.3.6 Contact Angle Measurement

The contact angle is a quantitative measure of wetting of a solid by a liquid. The contact angle is defined as the angle formed by a liquid at the three-phase boundary where a liquid, gas and solid intersect. In this thesis the liquid used is water and the contact angles were measured on a goniometer (Dataphysics, OCA, 15EC). The droplet volume was controlled constantly at 1 µL for each drop. A low contact angle values indicate that the liquid spreaded on the solid surface whilst high contact angle values show poor spreading. It is said that the liquid wets the surface if the contact angle is below 90°, zero contact angle indicates complete wetting. The surface is said to be non-wetting with the liquid if the contact angle is greater than 90°.

3.3.7 Electron Microscopy

The morphologies of the prepared samples were examined using a field emission scanning electron microscopy (FESEM, FEI Quanta SEM Model 400F). High resolution transmission electron microscopy (HRTEM) was carried out using JEOL JEM2100-F.

3.4 Evaluation of Electrochemical Properties

Electrochemical measurements of the sample including cyclic voltammetry (CV), galvanostatic charge/discharge (GCD) and electrochemical impedance spectroscopy (EIS) were measured using Gamry Reference 600 at room temperature. Electrochemical measurements were firstly conducted with a three-electrode setup, in which a saturated calomel electrode (SCE) was used as reference electrode, platinum wire as counter electrode and the synthesized nanocomposite as working electrode, respectively. For two-electrode setups, symmetric supercapacitors were built using a Teflon Swagelok® construction with two equal as-synthesized nanocomposite electrodes. A filter paper soaked in electrolyte was used as separator.

1.0 M sulphuric acid (H_2SO_4) was used as the electrolyte for the electrochemical measurements of PPy/CS, Ag@PPy and Ag@PPy/CS. As for the electrochemical measurements of PPy/ MnO_2 , 0.5 M sodium sulphate (Na_2SO_4) was used as the electrolyte instead of H_2SO_4 as acidic electrolytes would cause the dissolution of MnO_2 .

3.4.1 Cyclic Voltammetry (CV)

Cyclic voltammetry (CV) is a useful technique to determine the potential of the electrode being studied. The experimental procedure involves potential cycling between two pre-determined voltage at a constant sweep rate and the current response is recorded. The cycling is repeated using different sweep rate to access the electrode material under high as well as low scan rates. The scan rates were varied from 5 to 100 mV s^{-1} .

3.4.2 Galvanostatic charge/discharge

The specific capacitances of the samples were calculated galvanostatic charge/discharge (GCD) curves using Equation 2.4. A GCD test is able to simulate a realistic workload of a supercapacitor. Therefore, in this work, the GCD test was used to calculate the specific capacitances, evaluate the life cycling stability, energy and power density of the electrodes.

3.4.3 Electrochemical impedance spectroscopy

Electrochemical impedance spectroscopy (EIS) provides a convenient way to access the frequency response characteristics of electrode materials, especially the equivalent series resistance (ESR) and the charge transfer resistance (R_{ct}) values. The EIS was carried out in the frequency range between 100 kHz and 0.1 Hz with perturbation amplitude of 5 mV versus the open-circuit potential.

CHAPTER 4

EFFECT OF pH ON MORPHOLOGY AND SUPERCAPACITIVE PROPERTIES OF POLYPYRROLE/MANGANESE OXIDE NANOCOMPOSITE

4.1 Introduction

Supercapacitors, also known as electrochemical capacitors or ultracapacitors, bridge the critical performance gap between the current alternatives of conventional capacitors and batteries. Supercapacitors offer a higher power density than batteries and a higher energy density than conventional capacitors (You et al., 2014). Hence, supercapacitors have attracted great attention as fast charging and discharging energy storage devices. They have an expanding array of applications, including starters, power back-up systems, hybrid electrical vehicles, and portable electronics (Calvo et al., 2013; Zhang et al., 2012).

Supercapacitors can be classified into two categories based on their operating mechanisms: electric double layer capacitors (EDLC) and pseudocapacitors. The charge storage mechanism of an EDLC is based on non-faradic charge separation at the electrode/electrolyte interface. On the other hand, pseudocapacitors are based on the faradic redox reaction that occurs at the surface of the active material of the electrodes. Recently, much attention has been focused on developing efficient materials for pseudocapacitors because they generally have higher capacitance values than carbon-based materials.

Various transition metal oxides such as RuO₂ (Hu et al., 2004), MnO₂ (Wang et al., 2011), Co₃O₄ (Jagdale et al., 2014), NiO (Cheng et al., 2013), TiO₂ (Lu et al., 2012), and V₂O₅ (Kim et al., 2012) have been reported to be suitable electrode materials for supercapacitors. Although hydrated RuO₂ has a high specific capacitance (>700 F g⁻¹), it is very expensive, toxic in nature, and requires a strongly acidic electrolyte (Chang et al., 2008). These drawbacks caused researchers to search for cheaper and “greener” alternatives as electrode materials. MnO₂ has drawn the attention of researchers because of its great abundance in nature, low cost, high theoretical specific capacitance, environmental friendliness, and satisfactory capacitance performance in mild electrolytes (Wei et al., 2011; Zhang & Chen, 2009), which have made it a promising material for pseudocapacitors. However, manganese oxides have intrinsically poor electrical conductivity, which reduces the charge transfer reaction kinetics, while their dense morphologies would cause difficulty in the penetration of electrolyte into the bulk of the oxide material. In order to improve high-performance supercapacitors, it would therefore be rational to improve the electrical conductivity such as compositing with carbonaceous materials (Chen et al., 2010; Sawangphruk et al., 2013), and conducting polymers (Huo et al., 2014; Li et al., 2010; Yao et al., 2013). Another effective way is by making nanomaterials with porous morphologies (Dai et al., 2015; Zhang et al., 2009). Porous structures are able to provide high surface area to volume ratio, providing shorter ions diffusion path and faster charge transfer kinetics.

Several studies have combined both MnO₂ and PPy for supercapacitor applications. For instance, the preparation of PPy/MnO₂ composite supported on multiwall carbon nanotube pre-dispersed in poly(4-styrenesulfonic acid) (Sharma et al., 2010). Li *et al.* synthesized one-dimensional nanostructured PPy/MnO₂ composite using complex of methyl orange and FeCl₃ as a reactive and self-degraded soft-template (Li et al., 2010). Also, PPy/MnO₂ coaxial nanotube has been prepared by using pre-prepared

MnO₂ nanotubes as reactive templates (Yao et al., 2013). Although all these attempts have shown some improvements in the better utilization of MnO₂, more substantial improvements still have to be made to improve the electrochemical property using simple and green preparation method as well as low fabrication cost for its successful commercialization.

In the present study, we successfully developed a green, one-step and facile synthesis method to prepare PPy/MnO₂ nanocomposites without any surfactant. Herein, we report for the first time the tunable morphologies made possible by varying the pH conditions of the reaction's medium. The effect of pH on the electrochemical properties was also investigated. Three- and two-electrode configurations were used to study the electrochemical performance of the porous PPy/MnO₂ nanocomposite.

4.2 Results and Discussion

4.2.1 FTIR and Raman analysis

In this study, the formation of the PPy/MnO₂ nanocomposite took place via the facile in-situ redox reaction of KMnO₄ and pyrrole, in which Mn⁷⁺ was reduced to Mn⁴⁺ and pyrrole was oxidized to polypyrrole (PPy) simultaneously. **Figure 4.1a** shows the FTIR spectrum of the PPy/MnO₂ nanocomposite. A broad band around 3250 cm⁻¹ and a band at 1610 cm⁻¹ are ascribed to the stretching vibration of the O–H group of adsorbed water. The peak at 1362 cm⁻¹ can be attributed to the ring vibration of the pyrrole ring (Zang & Li, 2011). The bands located at 1064 and 932 cm⁻¹ are ascribed to the N–H in-plane deformation vibration and C–H out-of-plane vibration, respectively, indicating the doped state of PPy (Li et al., 2010). The observed band located at 496 cm⁻¹ corresponds

to the characteristic bending vibrations of Mn–O of [MnO₆] octahedron (Abulizi et al., 2014; Huo et al., 2014).

The Raman spectrum of PPy/MnO₂ is shown in **Figure 4.1b**. The nanocomposite exhibits the characteristic peaks of PPy at 1345 and 1564 cm⁻¹, which are assigned to the ring stretching mode and C=C backbone stretching of PPy, respectively (Gu et al., 2010). The peak at 640 cm⁻¹ corresponds to the Mn–O lattice vibrations perpendicular to the direction of the MnO₆ octahedron double chains of MnO₂ (Kumar et al., 2014).

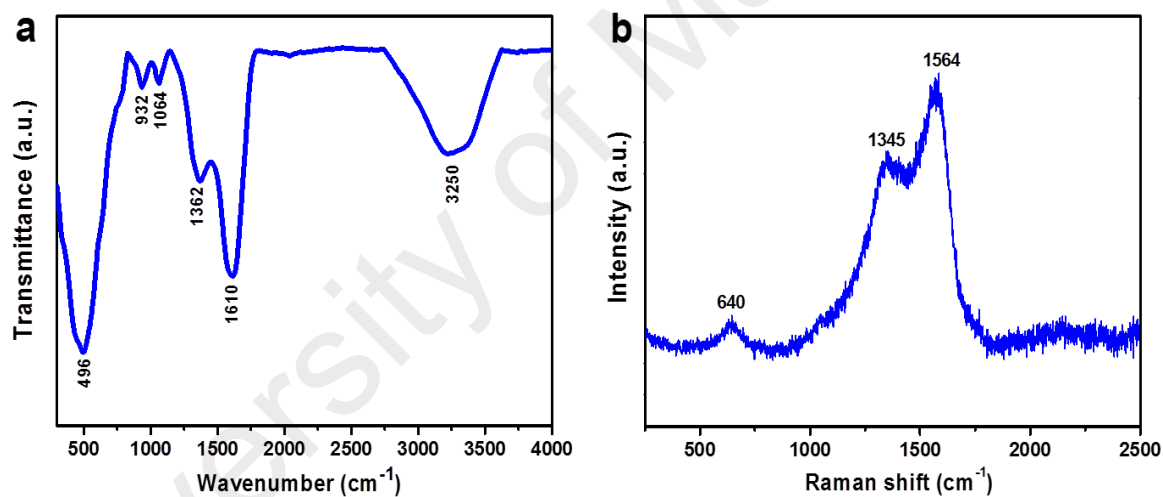


Figure 4.1: (a) FTIR and (b) Raman spectra of PPy/MnO₂ nanocomposite.

4.2.2 X-ray diffraction analysis

The PPy/MnO₂ nanocomposites were characterized by XRD, as shown in **Figure 4.2**. The two broad peaks observed at 37.3° and 66.1° are in good agreement with amorphous birnessite-type MnO₂ (JCPDS 18-0802). The XRD pattern of the nanocomposite shows weak and broad diffraction peaks, which suggest that the MnO₂ in the nanocomposite matrix has low crystallinity and a fine grain size (Wang et al., 2011). A broad diffraction peak located at ~13° was suspected to be due to the sample holder. This was verified by scanning the blank sample holder (Perspex material), and the diffraction peak found at 13.3° confirmed that the broad peak was due to the Perspex material.

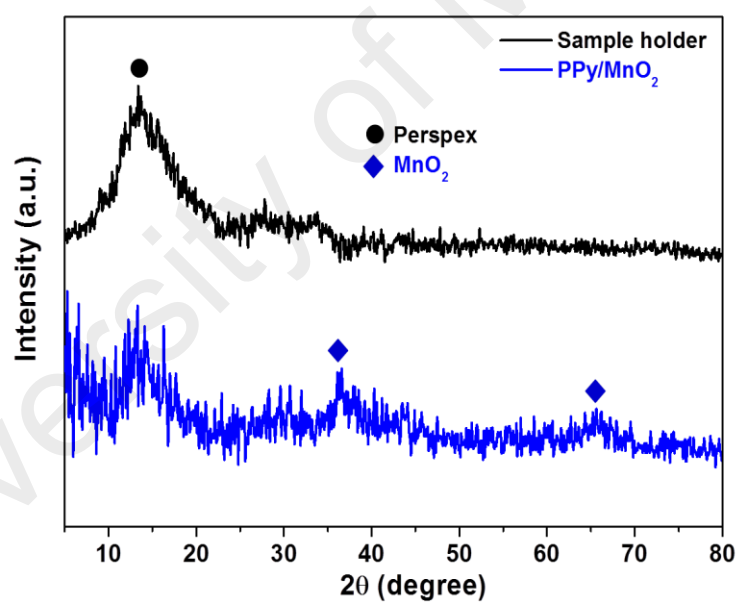


Figure 4.2: X-ray diffraction patterns of PPy/MnO₂ nanocomposite and sample holder.

4.2.3 Morphological studies

The morphologies of the PPy/MnO₂ nanocomposites prepared under different pH conditions were studied using FESEM. It was apparent that the pH had a significant effect on the morphology of the PPy/MnO₂ nanocomposite. The nanocomposite prepared at pH 1.0 (**Figure 4.3a**) shows a compact, sheet-like morphology, while a densely packed granular structure was observed when it was prepared at pH 2.0 (**Figure 4.3b**). Interestingly, when the pH was further increased to 4.0 (**Figure 4.3c**), the PPy/MnO₂ nanocomposite appeared to be highly porous in nature. At pH 5.0, as shown in **Figure 4.3d**, a porous structure can still be seen, but with some randomly dispersed composite granules within the structure. The porous structure was no longer observed when the pH of the solution was not adjusted, which was at 7.8; an FESEM image demonstrated a closely stacked granular morphology (**Figure 4.3e**). The elemental mapping (**Figure 4.3f**) represents the Mn, O, and N element distributions on the surface of the PPy/MnO₂ nanocomposite prepared at pH 4.0. Although the influence of the pH on the morphology of MnO₂ has also been reported elsewhere (Abulizi et al., 2014; Ji et al., 2012; Zhang & Mu, 2007), in this work, for the first time, we demonstrate the preparation of PPy/MnO₂ binary nanocomposites with different morphologies under the influence of pH.

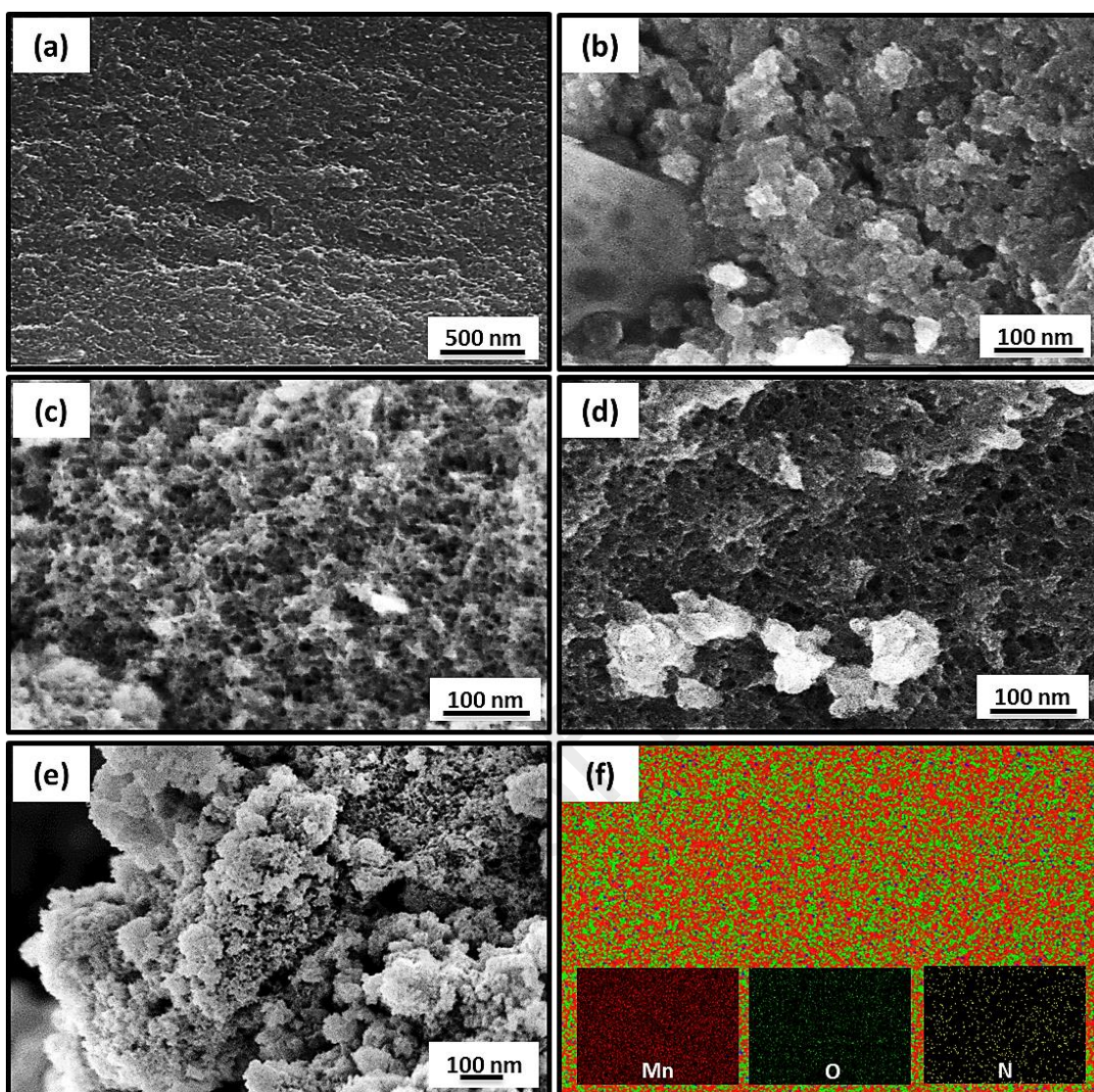


Figure 4.3: FESEM images of PPy/MnO₂ nanocomposites synthesized at various pH values of (a) 1.0, (b) 2.0, (c) 4.0, (d) 5.0, and (e) 7.8, and (f) elemental mapping of PPy/MnO₂ nanocomposite at pH 4.0.

4.2.4 Surface area analysis

The nitrogen adsorption-desorption isotherm can be used to measure the specific surface area of a material. The typical N₂ adsorption-desorption isotherm of the PPy/MnO₂ nanocomposite prepared at pH 1.0, 4.0 and 7.8 is shown in **Figure 4.4a**. For the nanocomposite prepared at pH 4.0, the isotherm displayed a Type IV isotherm according to the IUPAC classification, suggesting that the material has a mesoporous structure (Sharma et al., 2010). At a relative pressure above 0.6, the isotherm has a hysteresis loop, which is attributed to the capillary condensation that occurs in the mesopores (Liang et al., 2012). The typical pore-size distribution was obtained by means of the Barret-Joyner-Halenda (BJH) method. **Figure 4.4b** shows an abundance of mesopores centered at 11.1 nm for pH 4.0. A BET study showed that the PPy/MnO₂ prepared at pH 1.0, 4.0 and 7.8 had a specific surface area of 85, 230 and 173 m² g⁻¹, respectively. Furthermore, the porous PPy/MnO₂ prepared at pH 4.0 showed the highest total pore volume of 0.527 cm³ g⁻¹. The corresponding properties of the PPy/MnO₂ nanocomposites prepared at pH 1.0, 4.0, and 7.8 are summarized in **Table 4.1**. The highly porous and fibrous-liked structure of the PPy/MnO₂ prepared at pH 4.0, as seen from the FESEM, is in good agreement with the high specific surface area obtained from the BET studies.

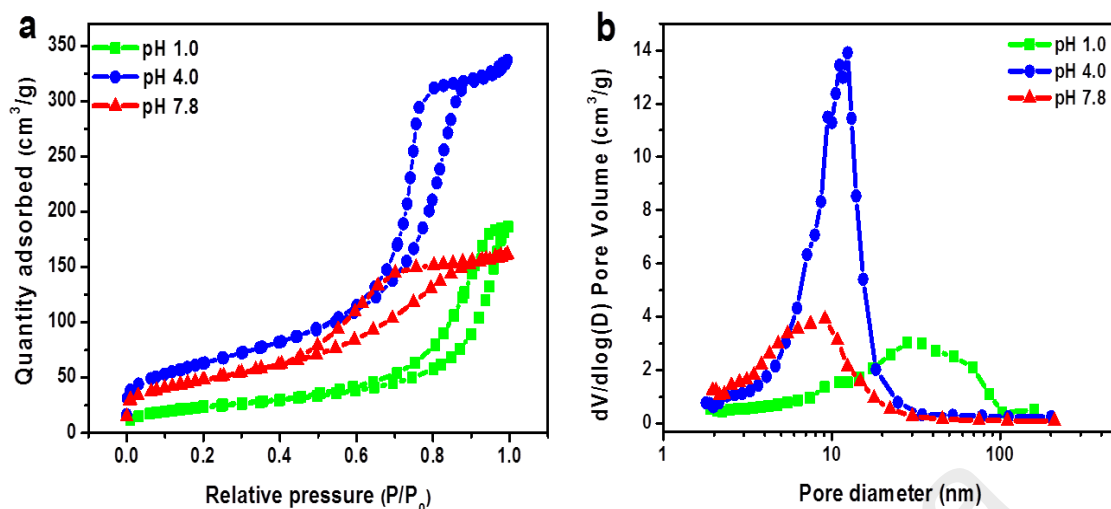


Figure 4.4: (a) N₂ adsorption/desorption isotherm and (b) pore size distribution curve of the PPy/MnO₂ nanocomposite prepared at pH 1.0, 4.0 and 7.8.

Table 4.1: BET specific surface areas (S_{BET}), total pore volumes, and average pore sizes of PPy/MnO₂ nanocomposites.

pH	Types of morphology	S_{BET} (m ² g ⁻¹)	Total pore volume (cm ³ g ⁻¹)	Average pore size (nm)
1.0	compact sheet	85	0.290	13.2
4.0	porous	230	0.527	8.0
7.8	granular	173	0.258	5.6

4.2.5 XPS analysis

Figure 4.5 shows the XPS spectra obtained from the porous PPy/MnO₂ nanocomposite. **Figure 4.5a** shows the Mn 2p core level spectrum of the PPy/MnO₂ nanocomposite, in which two peaks are observed at 642.3 and 654.1 eV corresponding to the binding energies of the Mn 2p_{3/2} and Mn 2p_{1/2} core levels, respectively. The spin

energy separation of 11.8 eV is in good agreement with the reported data for MnO₂ (Zhao et al., 2014). **Figure 4.5b** shows the O 1s core level spectrum of the porous nanocomposite. Deconvolution indicates three different oxygen binding configurations, namely an Mn–O–Mn oxide bond at 530.5 eV, Mn–O–H hydroxyl bond at 531.1 eV, and H–O–H residual water bond at 532.5 eV. The observed Mn–O–H and H–O–H reveals the hydrous nature of MnO₂ (Xiao et al., 2014).

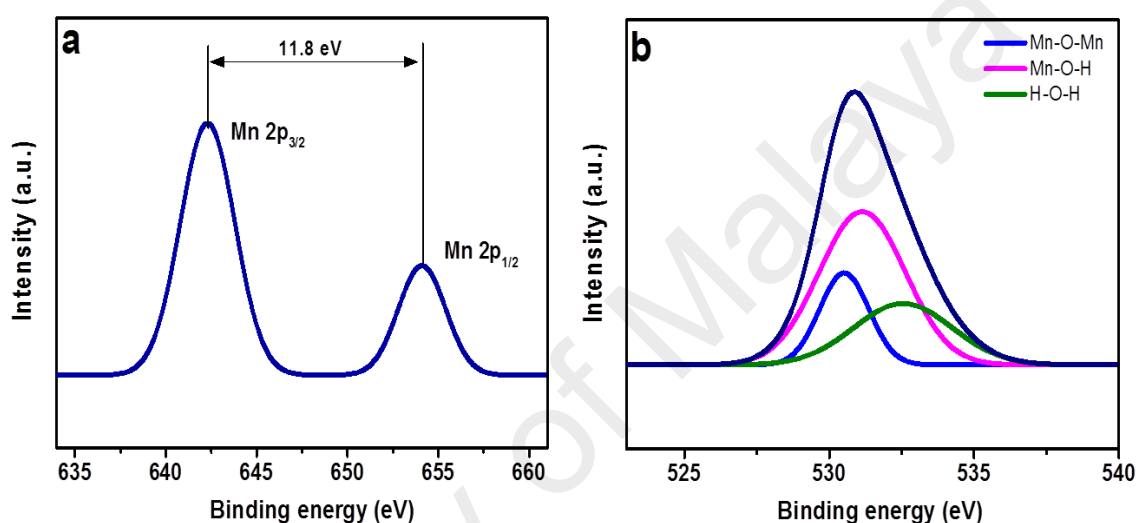


Figure 4.5: XPS spectra of MnO₂/PPy nanocomposite at (a) Mn 2p and (b) O 1s core level spectra.

4.2.6 Electrochemical characterization of PPy/MnO₂ nanocomposite

The electrochemical performances of the PPy/MnO₂ nanocomposites prepared under different pH conditions were evaluated using cyclic voltammetry (CV) techniques. Their respective CV curves at a scan rate of 10 mV s⁻¹ in 0.5 M Na₂SO₄ are shown in **Figure 4.6a**. Among the different pH values, the PPy/MnO₂ formed at pH 4.0 shows the largest current area. Therefore, as expected from its CV curve, Figure 4.6b the specific capacitance calculated from the GCD measurements showed the highest specific capacitance was obtained for the PPy/MnO₂ at pH 4, which was calculated to be 306 F

g^{-1} at 0.2 A g^{-1} . The specific capacitances calculated from the GCD measurements of the nanocomposites against the solution pH are plotted in **Figure 4.6b**. When the pH of the solution was increased from 1.0 to 4.0, the specific capacitance increased from 41 F g^{-1} to a maximum of 306 F g^{-1} . Then, a further increase in the pH eventually led to a decrease in specific capacitance. The KMnO_4 acted as an oxidant to initiate the oxidative polymerization of pyrrole, and its oxidizing capability could be easily controlled by the acidity and concentration (Wang et al., 2012b). In the case of pH 1.0 and 2.0, the very low specific capacitance compared to the other pH values was due the strong oxidizing power of the KMnO_4 under a strong acidic environment. The overoxidation of PPy causes polymer degradation and hinders the delocalization of charge carriers in the polymer, thus reducing its electronic conductivity (Frackowiak et al., 2006; Tallman et al., 2002). Consequently, the overall electrochemical performance would have deteriorated. The high specific capacitance of the PPy/ MnO_2 nanocomposite at pH 4.0 could be attributed to its highly porous morphology, which facilitated the diffusion and effusion of electrolyte ions. Hence, the charge transfer kinetics was improved because of the higher surface activity. When prepared at the optimized pH of 4.0, the growth of PPy and MnO_2 occurred simultaneously to form a porous structure, as seen from the FESEM. The moderate acidity of the reactant mixture was sufficient for the pyrrole to polymerize without overoxidation, concurrently improving the conductivity of MnO_2 by providing a percolative path for electrolytes ions. After the optimized pH of 4.0, the further diminution of the oxidizing power of KMnO_4 led to the formation of closely stacked granules, resulting in a lower specific capacitance value.

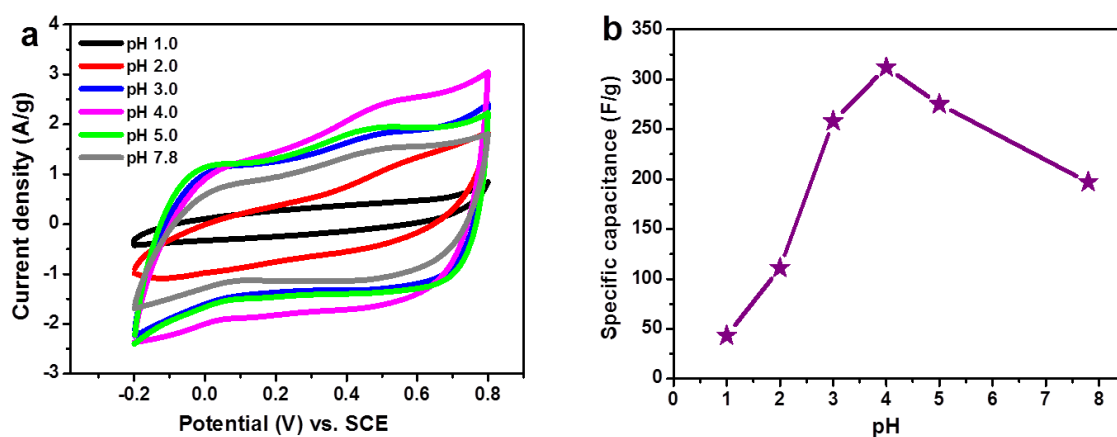


Figure 4.6: (a) CV curves at 10 mV s^{-1} obtained for PPy/MnO₂ nanocomposites prepared under different pH conditions and (b) specific capacitance values for different pH conditions calculated at current density of 0.2 A g^{-1} .

The influence of the scan rate on the electrochemical performance of the porous PPy/MnO₂ nanocomposite at pH 4.0 is shown in **Figure 4.7a**. The near-ideal rectangular shape at the low scan rates shows the good capacitance property. At 100 mV s^{-1} , the slightly distorted rectangle shape is the effect of the lower charge mobilization per unit time. **Figure 4.7b** presents the galvanostatic charge/discharge curves of the nanocomposite at various current densities, which gave a specific capacitance of 306 F g^{-1} at 0.2 A g^{-1} . The typical triangular shape from the charge and discharge curve suggests good charge propagation across the porous PPy/MnO₂ nanocomposite. The porous nanostructured design accounts for the increased specific surface area, which improved the electrolyte accessibility and effectively reduced the relaxation time for the electrode, resulting in a high electrochemical performance.

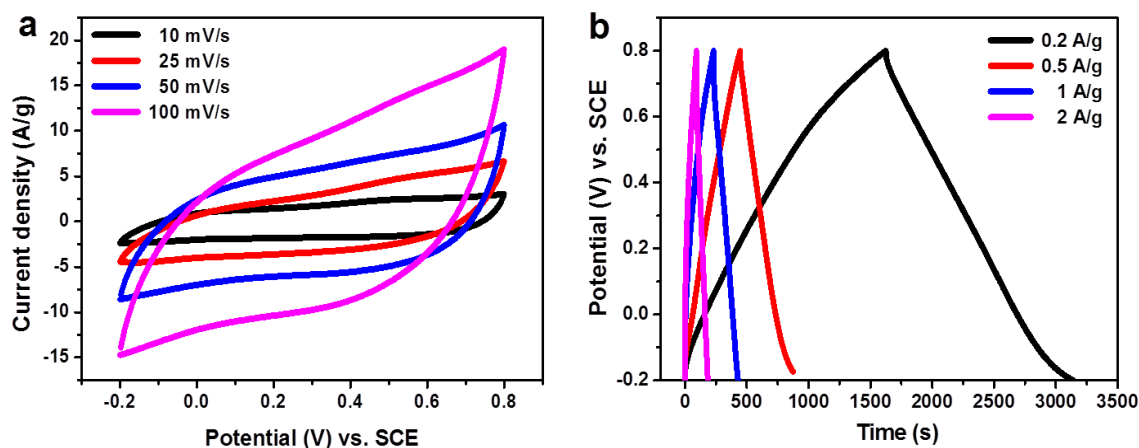


Figure 4.7: CV curves at various scan rates and (b) GCD curves at various current densities for porous PPy/MnO₂ nanocomposite (pH 4.0).

In order to understand the effect of the pH on the formation of the PPy/MnO₂ nanocomposite, the electrochemical impedance spectra (EIS) were recorded in a frequency range between 0.1 Hz and 100 kHz, as shown in **Figure 4.8**. The first intercept of the semicircle at the real axis in the high frequency region represents the equivalent series resistance (ESR), which is attributed to the resistance of the electrolyte; the contact resistance between the electrolyte, current collector, and active material; and the intrinsic resistance of the active material itself. The ESR values were determined to be 7.3, 4.0, and 6.1 Ω for the pH conditions of 1.0, 4.0, and 7.8, respectively. The charge transfer resistance (R_{ct}) can be determined from the diameter of the semicircle. From the Nyquist plot, the R_{ct} values of pH 1.0, 4.0, and 7.8 are 22.7, 2.9, and 15.9 Ω , respectively. The PPy/MnO₂ synthesized at pH 1.0 has a very large R_{ct} value due to the overoxidation of PPy under strong acidic conditions, which caused polymer degradation and decreased the electrical conductivity within the composite. The large ESR and R_{ct} values for pH 7.8 were most probably due to the high contact resistance between the nanocomposite particles as a result of its granular structure and lower porosity, which is in good agreement with the FESEM and BET results. The porous PPy/MnO₂

nanocomposite (pH 4.0) had the lowest ESR and R_{ct} values owing to its highly porous morphology, which allowed an efficient penetration of the electrolyte ions, faster charge transfer kinetics, and a good surface activity.

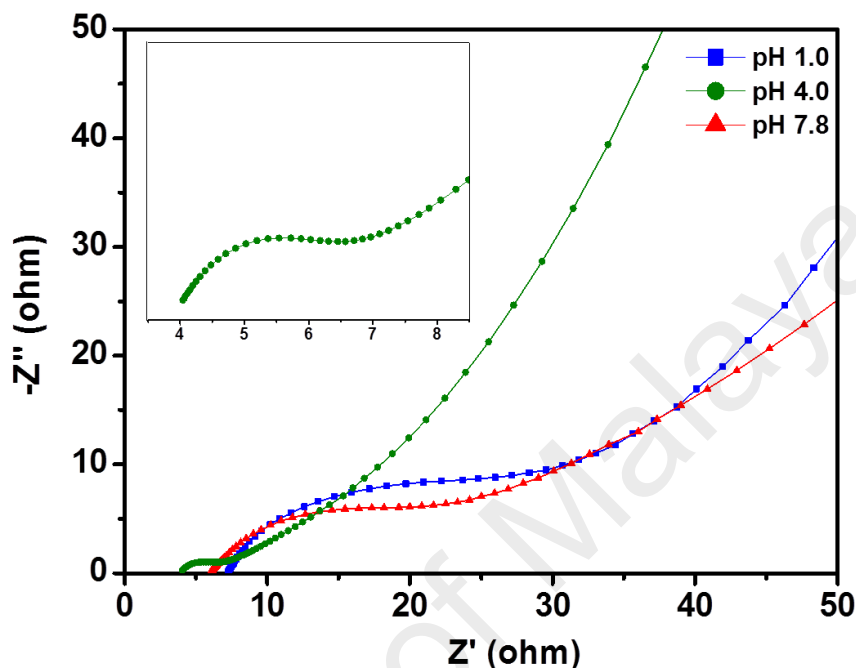


Figure 4.8: Nyquist plots of EIS for PPy/MnO₂ nanocomposites prepared at pH 1.0 (compact sheet), 4.0 (porous), and 7.8 (granular). Inset is a magnified portion of the PPy/MnO₂ prepared at pH 4.0.

4.2.7 Supercapacitor device performance of porous PPy/MnO₂ nanocomposite

We had made an attempt to fabricate a symmetric supercapacitor device to further evaluate the electrochemical performance of the porous PPy/MnO₂ nanocomposite (pH 4.0). **Figure 4.9a** shows the cyclic voltammograms of the symmetric supercapacitor device, which have a rectangular shape within the potential range of 0 to 1.0 V. The galvanostatic charge/discharge of the porous PPy/MnO₂ nanocomposite is shown in **Figure 4.9b**. The charging and discharging reveal symmetrical curves, signifying excellent reversibility. The specific capacitance obtained

from the discharging curve is calculated to be 134 F g^{-1} at a current density of 0.2 A g^{-1} . The high specific capacitance is ascribed to the good conductivity and porous structure of the porous PPy/MnO₂ nanocomposite. The mesopores favor the access of the electrolyte ions to the active surface of the electrode, improving the charge transfer process (Ra et al., 2009). The Ragone plot shows the dependence between the power output and energy density of the symmetric supercapacitor device (**Figure 4.9c**). The power density of the electrode decreased from 2800 to 475 W kg⁻¹ as the energy density increased from 3.9 to 17.0 W h kg⁻¹. A high power density of 2800 W kg⁻¹ was achieved with an energy density of 3.9 W h kg⁻¹.

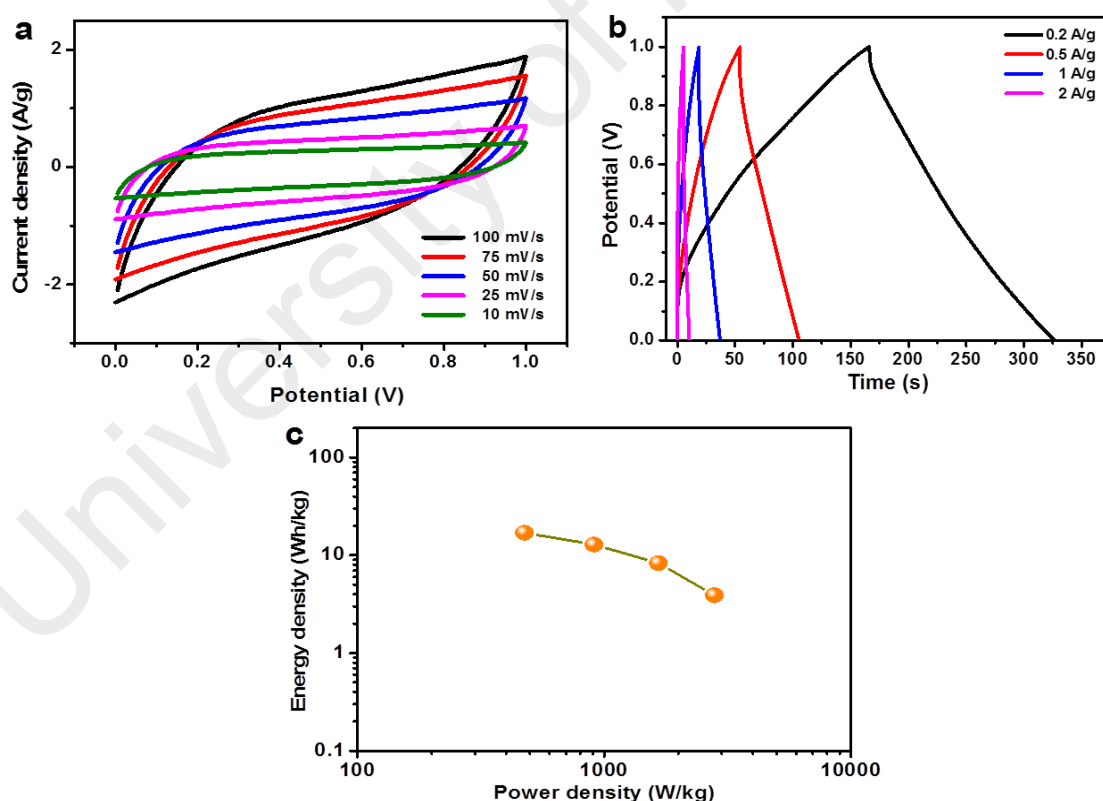


Figure 4.9: (a) CV curves at various scan rates, (b) galvanostatic charge/discharge curves at various current densities, and (c) Ragone plot of the symmetric supercapacitor device.

In our previous study, we obtained 321 F g^{-1} of specific capacitance for our $\text{MnO}_2\text{-Mn}_2\text{O}_3/\text{graphene/PPy}$ electrode (three-electrode system). However, such high capacitance value is only obtainable at a very low scan rate (1 mV s^{-1}) (Lim et al., 2014). The highly distorted shape of the CV curve at high scan rates showed large performance loss, which hinders their practical applications as supercapacitor electrode. The present study is able to achieve specific capacitance of 306 F g^{-1} at scan rate of 0.2 A g^{-1} and the CV shows quasi-rectangular shapes even at high scan rates suggest good charge propagation across the porous PPy/ MnO_2 nanocomposite. In another previous work, a symmetric supercapacitor of $\text{MnO}_2\text{-Mn}_2\text{O}_3/\text{graphene oxide/PPy}$ electrodeposited on porous nickel foam substrate showed very low maximum energy density of 6.8 W h kg^{-1} and a maximum power density of 469 W kg^{-1} (Ng et al., 2014), in contrast to our current study which showed a maximum energy density of 17.0 W h kg^{-1} and a maximum power density of 2800 W kg^{-1} . The study also showed a specific capacitance of 65 F g^{-1} at 1 A g^{-1} while our present study showed a specific capacitance of 87 F g^{-1} calculated at the same current density (**Figure 4.10**). These improvements are essential in meeting the increasing demand for high power and energy devices. Although the utilization of nickel foam as a substrate gave rise to porous morphologies, the nanocomposite itself is not porous enough on a nanoscopic level; hence its low energy and power density. In both previous studies, the electrodeposited manganese oxide within the composite consisted of Mn^{3+} and Mn^{4+} . According to Taguchi *et al.*, the conductivity of Mn_2O_3 involving Mn^{3+} is rather low as compared to that of MnO_2 involving Mn^{4+} (Taguchi et al., 2006). This could be the reason of the low electrochemical performances of our previous works. This present work has successfully addressed previous shortcomings by combining the desirable MnO_2 and the synthesis of nanoscopic porous structures. This demonstrates the superiority of the present PPy/ MnO_2 over our previous studies.

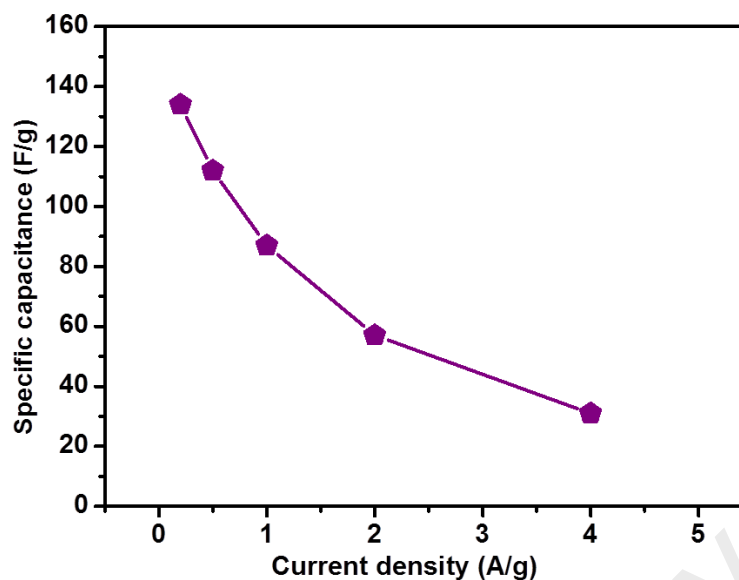


Figure 4.10: Dependence of specific capacitance values on current density for the symmetric supercapacitor device.

Cycling stability is essential for the commercialization of supercapacitor materials. **Figure 4.11** shows the capacitance retention as a function of the cycle number at a current density of 1 A g^{-1} for up to 1000 cycles. The porous PPy/MnO₂ showed remarkable cycling stability and retained up to 93.2% of its initial capacitance after 1000 charge/discharge cycles owing to its highly porous morphology that facilitates the diffusion and effusion of electrolytes, exhibit promising characteristics as an electrode material for high-performance supercapacitors.

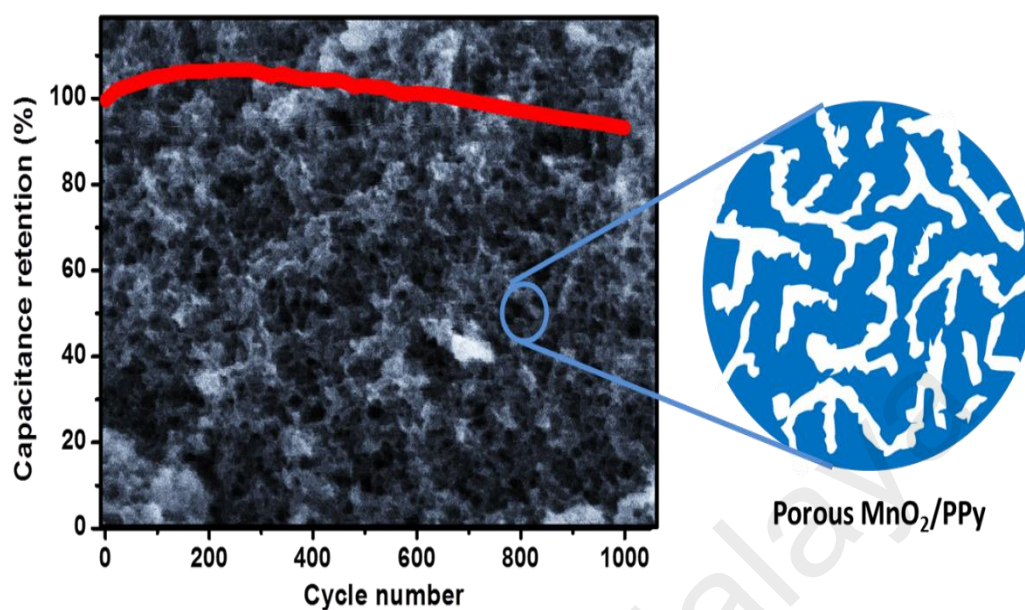


Figure 4.11: Cycling stability of the fabricated symmetric supercapacitor device.

4.3 Conclusion

This work featured a facile and inexpensive strategy for the synthesis of PPy/MnO₂ nanocomposites with tunable morphologies using simple pH adjustments. When the solution pH was increased from 1.0 to 7.8, the morphologies of the PPy/MnO₂ nanocomposite changed from a compact sheet-like structure to a highly porous structure and finally a granular structure. The improved capacitance and rate-capability of the porous PPy/MnO₂ nanocomposite can be accredited to several aspects, including (1) the incorporation of electrically conducting polymer into the composite, which enhanced the conductivity of MnO₂; (2) the pseudocapacitive intrinsic nature of PPy, which contributed positively to the electrochemical performance of the binary nanocomposite; (3) the porous structure of the PPy/MnO₂ nanocomposite, which

improved the electrolyte accessibility, improved the charge transfer kinetics, and produced a higher surface activity on the electrode, resulting in maximum utilization of the active materials. Benefiting from its splendid characteristics, the porous PPy/MnO₂ nanocomposite was shown to exhibit a significantly improved electrochemical performance.

University of Malaya

CHAPTER 5

EXCEPTIONAL ELECTROCHEMICAL PERFORMANCE OF HYDROPHILIC POLYPYRROLE/CHITOSAN NANOCOMPOSITE ELECTRODE FOR SUPERCAPACITORS

5.1 Introduction

Supercapacitors or electrochemical capacitors offer a promising approach to meet the increasing power demands of energy storage systems in the twenty first century and they bridge the critical performance gap between the current alternatives of conventional capacitors and batteries. Supercapacitors offer a higher power density than batteries and a higher energy density than conventional capacitors (You et al., 2014). Supercapacitors have a wide array of applications, including consumer electronics, power back-up systems, starters and military defence systems (Calvo et al., 2013; Zhang et al., 2012).

Based on the operating mechanism, supercapacitors can be classified into two categories; electric double layer capacitors (EDLC) and pseudocapacitors. Carbon-based materials are examples of EDLC. These carbonaceous store charges non-Faradaically, relying on the electrostatic charge separations at the highly accessible surface area of the electrode/electrolyte interface. Pseudocapacitors apply a completely different charge-storage mechanism. Instead of storing charges, charges are being transferred through the reversible faradaic redox reactions at the electrode/electrolyte interface (Su et al., 2013). Lately, pseudocapacitors have been brought into the limelight as they have relatively higher capacitances values than EDLC (Conway et al., 1997) and they can be chosen from a wide array of materials that include transition metal oxides

(Jagadale et al., 2014; Lei et al., 2010; Pusawale et al., 2013; Ren et al., 2013) and conducting polymers (Dubal et al., 2013; Ramya et al., 2013). Conducting polymers stood out from the rest as they have higher charge density compared to carbon materials and lower cost in contrast to metal oxides (Patil et al., 2013).

From an application standpoint, PPy is one of the most widely used polymers in the research and in the industry, due to its electrochemical processing flexibility, light weight, and high electrical conductivity than most commercially available conducting polymers (Hepowit et al., 2012). The main drawback of conducting polymers is that it suffer from low mechanical stability and a shorter life cycle due to phase changes and the slow diffusion of ions within the bulk of the electrode during faradic reaction (Snook et al., 2011). To counter this problem and to enhance the energy storage performance, PPy has been strategically combined with carbon based materials such as activated carbon (Keskinen et al., 2015), carbon nanotubes (Oh et al., 2008) and graphene (Wang et al., 2012) and metal oxides like MnO₂ (Bahloul et al., 2013), and CoO (Zhou et al., 2013). Producing PPy with porous morphologies is also an effective approach to enhance the electrochemical performance of PPy (Dubal et al., 2012; Sharma et al., 2008b).

Chitosan (CS) is a linear hydrophilic polysaccharide derived from naturally occurring chitin, second most abundant organic compound next to cellulose. Its unique properties such as antimicrobial activity, biocompatibility, nontoxicity, high mechanical strength and a susceptibility to chemical modifications have been utilized in biosensors, water purification, wound healing, and scaffolds for tissue engineering (Ayad et al., 2014; Fusco et al., 2013; Koev et al., 2010; Sun et al., 2009; Zeng et al., 2009).

For supercapacitor applications, CS is commonly used as a polymer gel electrolyte (Sudhakar & Selvakumar, 2012; Yamagata et al., 2013) or can be carbonized

to produce nitrogen-doped carbon materials (Hao et al., 2015; Ling et al., 2015; Sun et al., 2015). However, only a handful of studies employ CS nanocomposites directly as an electrode material for energy storage applications. Hassan *et al.* prepared MnO₂-CS nanocomposite *via* cathodic electrodeposition yielded a specific capacitance of 424 F g⁻¹ obtained at a current density of 1 mA cm⁻² (Hassan et al., 2014). A ternary composite of CS/ZnO/Polyaniline reached a maximum specific capacitance of 587 F g⁻¹ at a current density of 150 mA cm⁻² (Pandiselvi & Thambidurai, 2014).

In this present work, we attempt to increase the specific capacitance of PPy by improving its hydrophilicity with CS. Studies have reported that the increased hydrophilicity of an electrode surface can augment the supercapacitive characteristics due to the better infiltration of the electrolyte into the framework of the electrode (Erdenedelger et al., 2014; Navale et al., 2015; Pawar et al., 2012; Wang et al., 2012). The rationale of this study is to incorporate the hydrophilic CS into PPy to improve the hydrophilicity of the PPy and accordingly enhance its electrochemical capacitance as electrode materials for supercapacitors.

The work of Yalçinkaya *et al.* reported the electrochemical synthesis of PPy/CS composite with improved thermal stability. Electrochemical measurements have shown that the PPy/CS composite is very stable and extremely electroactive (Yalçinkaya et al., 2010). However, this study was limited to the synthesis and characterization of the PPy/CS composite without any application studies. To the best of our knowledge, there is no report on PPy/CS for supercapacitor applications. Herein, PPy/CS composites prepared *via* a one-step anodic electrodeposition were demonstrated for the first time as electrode material for supercapacitors. The CS content was varied to determine its effect on the hydrophilicity and the specific capacitance. Electrochemical performances of the PPy/CS composite electrodes were studied using three- and two-electrode configurations.

5.2 Results and Discussion

5.2.1 Synthesis and formation mechanism

In this study, the PPy/CS nanocomposite electrode was formed from a deposition mixture containing CS solution and pyrrole monomer. Even though we have successfully electrodeposited PPy and PPy/CS nanocomposite under the positive potential of 0.8 V, we were unable to do so for the lone CS solution. The electrodeposition of CS from an aqueous suspension had been reported using electrophoretic deposition method in which the deposition of CS occurs on the cathode under high voltages between 4 to 30 V (Li et al., 2011; Sun et al., 2009), another way of getting CS film is by applying reduction voltages (-0.1 to -1 V) to the working electrode in a conventional three-electrode system (Zangmeister et al., 2006; Zeng et al., 2009). Both methods take advantage of the pH dependent solubility of CS. At reducing potentials, hydrogen evolution takes place at the surface of the cathode lead to a locally high pH values. The CS then becomes deprotonated and is no longer soluble under basic conditions, depositing at the electrode surface (Koev et al., 2010; Luo et al., 2005). However, these working potentials are unsuitable for the electrodeposition pyrrole monomers because the high voltages applied during electrophoretic deposition may cause the overoxidation of PPy, producing unfavourable PPy films with low conductivity. On the other hand, the pyrrole monomers are unable to polymerize under reducing potentials. We found that the deposition of CS at low positive potentials is only possible in the presence of pyrrole monomer. We deduce that the pyrrole monomers were already entrapped in the CS biopolymer during the preparation of the deposition solution due to the strong hydrogen bonds formed between them. During the polymerization of pyrrole on the electrode surface, the pyrrole monomers with the attached CS will be attracted to the electrode surface and propagate to form the PPy/CS

nanocomposite. Electrodeposition of PPy/CS nanocomposite using CV technique scanned only at positive potentials was also reported where CS was incorporated into the nanocomposite without deprotonation (Yalçinkaya et al., 2010). The schematic representation in **Figure 5.1** shows the attachment of pyrrole monomers onto chitosan followed by polymerization to form the PPy/CS nanocomposite electrode.

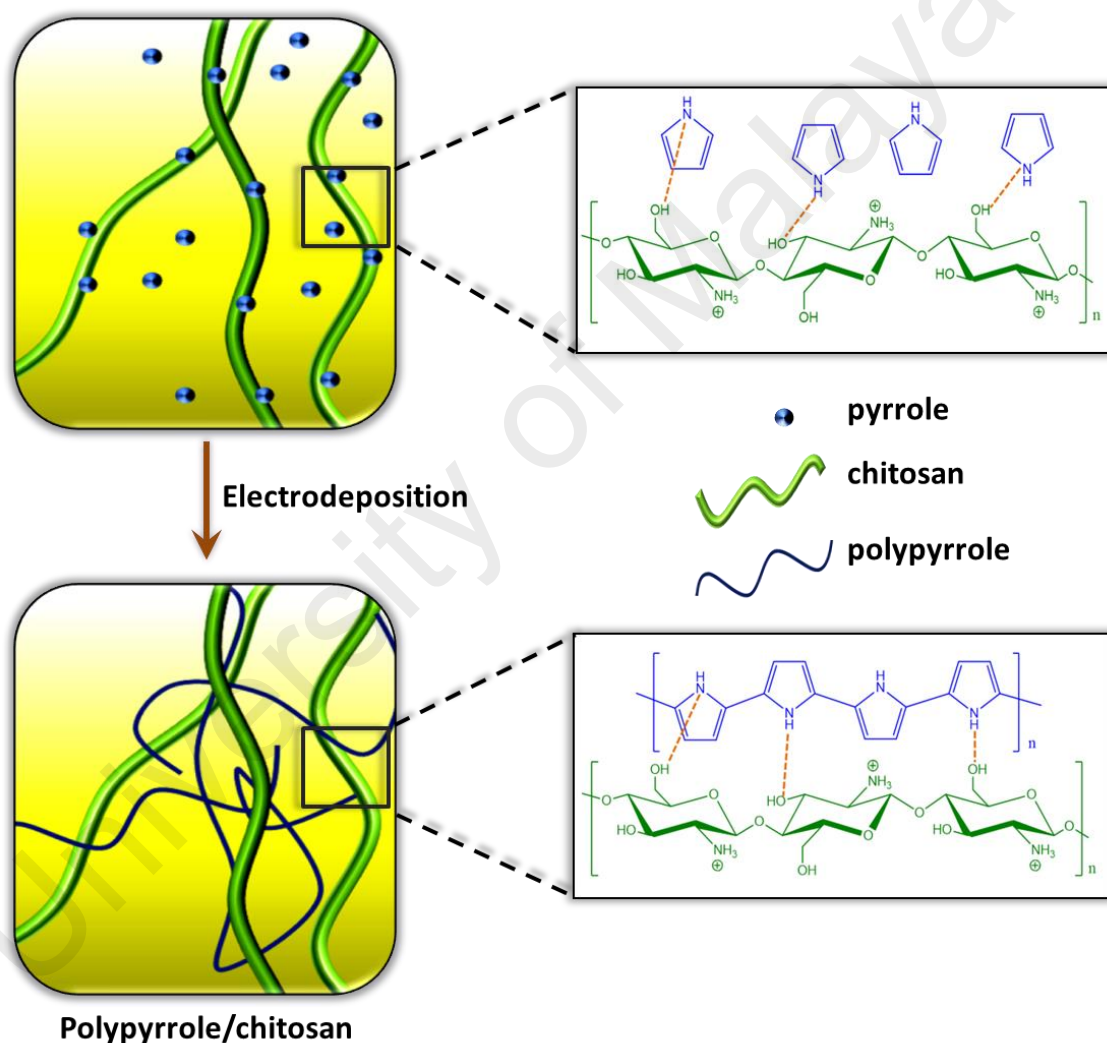


Figure 5.1: Mechanism for the formation of PPy/CS nanocomposite electrode.

5.2.2 FTIR analysis

Figure 5.2 shows the FTIR spectra of the CS, PPy and PPy/CS nanocomposite. For the CS powder, the broad band around 3318 cm^{-1} is due to the stretching vibrations of the primary amine ($-\text{NH}_2$) and hydroxyl groups ($\text{O}-\text{H}$) in CS (Fusco et al., 2013). The band at 2876 cm^{-1} is attributed to the aliphatic $\text{C}-\text{H}$ stretching and the band at 1588 cm^{-1} was corresponded to the $-\text{NH}_2$ bending vibration (Koev et al., 2010). A peak at 1381 cm^{-1} was assigned to $-\text{C}-\text{O}$ stretching mode of $-\text{CH}_2-\text{OH}$ group. The broad peak around 1027 cm^{-1} was due to the $\text{C}-\text{O}$ stretching (Li et al., 2011).

The PPy spectrum shows that the $\text{N}-\text{H}$ and $\text{C}-\text{H}$ stretching peaks were located at 3340 and 3000 cm^{-1} , respectively. The band at 1622 cm^{-1} was corresponded to the $\text{C}=\text{C}$ vibration of the pyrrole ring, while the band at 1490 cm^{-1} was contributed by the $\text{C}-\text{N}$ stretching vibration. The pyrrole ring vibration was observed at 1423 cm^{-1} while the $\text{C}-\text{H}$ in-plane deformation can be observed at 1278 cm^{-1} (Zang & Li, 2011). The bands at 1100 and 982 cm^{-1} can be attributed to $\text{N}-\text{H}$ in-plane deformation vibration and the $\text{C}-\text{H}$ out-of-plane vibration, respectively, implying the doping state of PPy (Li et al., 2010). In the PPy/CS nanocomposite, some of the CS peaks (3318 , 1381 , 1027 cm^{-1}) have overlapped with the characteristic peaks of PPy. The composite showed a broad absorption band around 3315 cm^{-1} due to the overlapping of $\text{N}-\text{H}$ and $\text{O}-\text{H}$ stretching vibration of CS with the amine group of PPy (Yalçınkaya et al., 2010). The absorption band attributed to $-\text{NH}_2$ bending vibration observed in CS disappeared (1588 cm^{-1}) and a new peak at 1649 cm^{-1} assigned to the asymmetric NH_3^+ bending vibration was observed. This indicated the protonation of the amine group of CS in the nanocomposite (Koev et al., 2010; Yamada & Honma, 2005) and also in good agreement with our proposed mechanism for the formation of PPy/CS nanocomposite whereby the amine groups are still protonated.

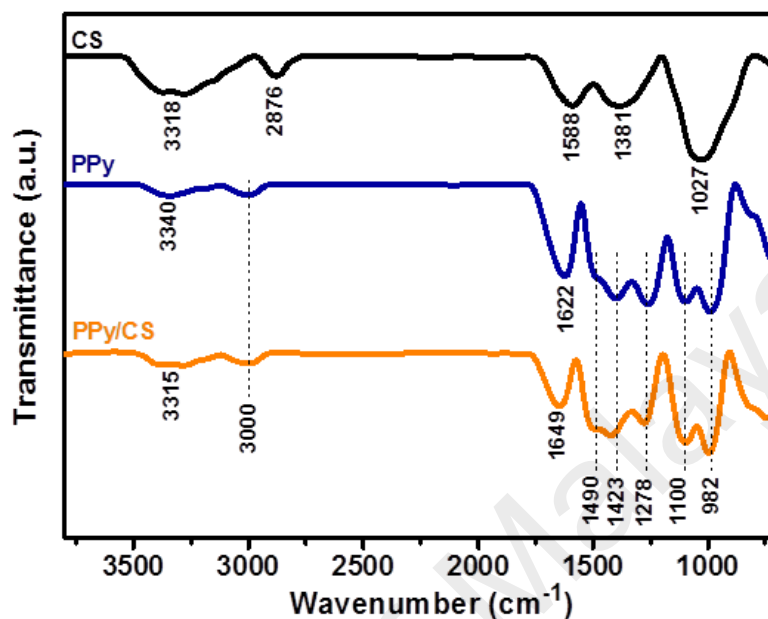


Figure 5.2: FTIR of CS, PPy and PPy/CS.

5.2.3 Morphological studies of PPy/CS nanocomposite electrodes

The morphologies of the PPy/CS composite electrodes were analyzed by FESEM. **Figure 5.3a** shows that the pure PPy electrode is made up of spheres with fairly smooth surfaces. For PPy/CS-0.5, the spheres appear to be rougher and more distinct from each other (**Figure 5.3b**). As for **Figure 5.3c** and **d**, the further increment in the CS content gave larger and rougher spheres with noticeable bulbous particle protruding out of the surface of the spheres. Elemental mapping was performed on the PPy/CS-0.75 nanocomposite, as shown in **Figure 5.3e**. The areas of bright contrast on the element maps correlate with the C, N and O signal maps.

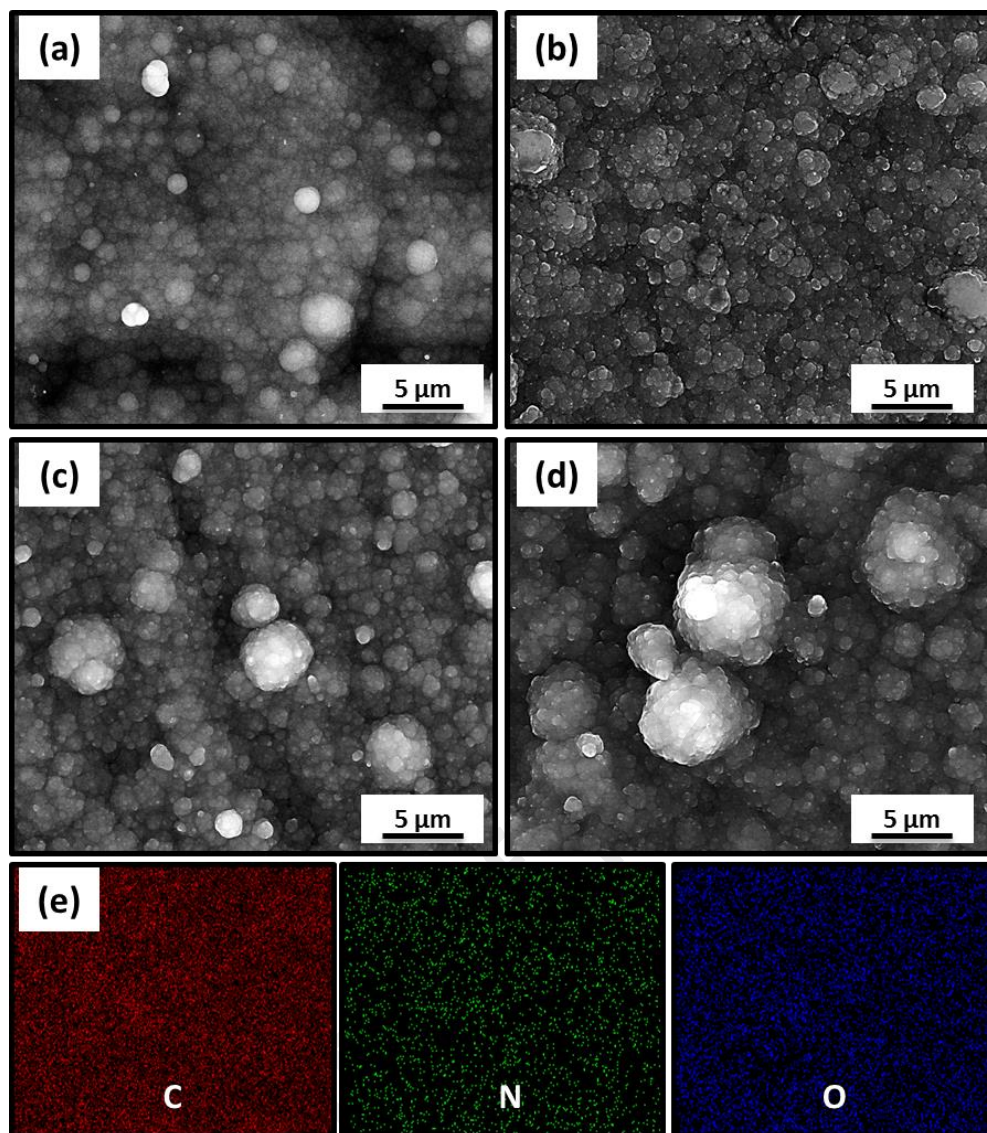


Figure 5.3: FESEM images of (a) pure PPy; PPy/CS nanocomposite electrodes with CS contents of (b) 0.5, (c) 0.75, (d) 1.0 wt%, and (e) elemental mapping of the PPy/CS-0.75 nanocomposite electrode.

5.2.4 Surface wettability studies of PPy/CS nanocomposite electrodes

An appreciable wetting of solid electrode by the aqueous electrolyte is only possible when the surface is hydrophilic in nature. The digital images for the water contact angle measurements are shown in **Figure 5.4**. The wettability of a solid with water depends on the relation between the interfacial tensions (water/air, water/solid and solid/air). A contact angle of 0° indicates complete wetting whilst a contact angle of

180° shows complete non-wetting. The water contact angle of the pure PPy electrode was found to be 71.1° which was still less than 90°, indicating that PPy is an intrinsically hydrophilic material (Jagadale et al., 2014). For the nanocomposite electrodes, it was observed that the water contact angle decreased from 46.5° to 33.6° when the CS content was increased from 0.5 to 1.0 wt%, displaying an increased in hydrophilicity. The water contact angle of the nanocomposites were far lower than the pure PPy because of the presence of hydroxyl and amine groups in the CS molecule that enable the formation of hydrogen bonds with the water droplet, greatly improving the electrode's wettability.

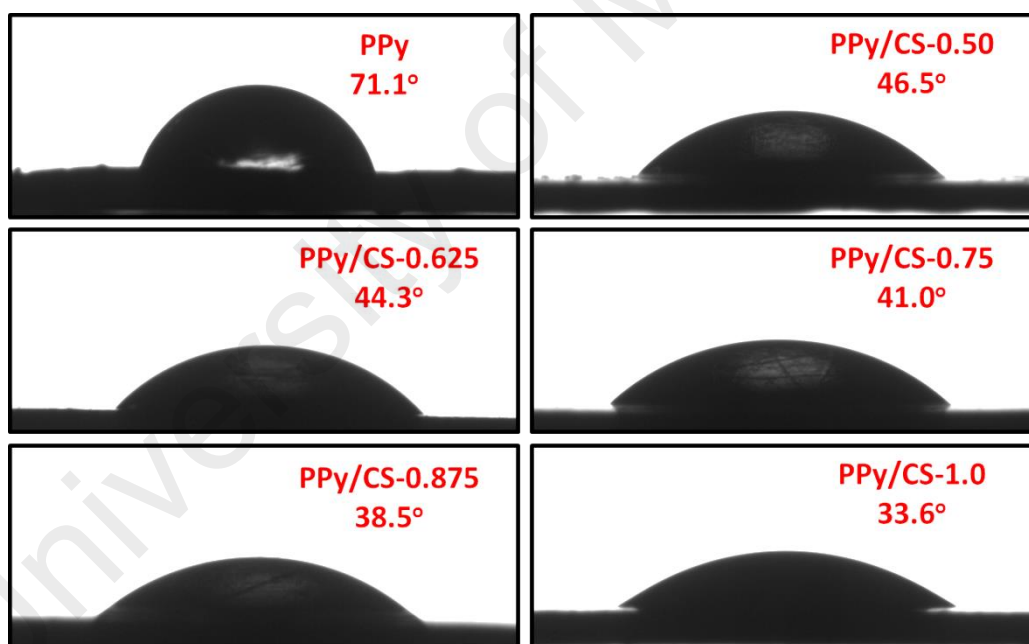


Figure 5.4: Digital images of water droplets on the surfaces of the as-prepared electrodes.

5.2.5 Electrochemical characterization of PPy/CS nanocomposite electrodes

Electrochemical performances of the electrodes were first examined in a three-electrode system by cyclic voltammetry (CV) and galvanostatic charge/discharge (GCD) in 1 M H₂SO₄. **Figure 5.5a** shows the CV profiles of PPy and PPy/CS nanocomposite electrode at a scan rate of 25 mV s⁻¹. Notably, the area under the curve for the PPy/CS composite electrode is larger than that of the PPy electrode. This larger area correlates to the higher specific capacitance that is attributed to the better wettability of the composite electrode. The GCD test of the PPy and PPy/CS were performed at a current density of 0.2 A g⁻¹. As shown in **Figure 5.5b**, the GCD curves exhibit almost linear lines, indicating typical behavior of supercapacitors. The specific capacitances of the electrodes calculated from the discharge curves are 273 and 403 F g⁻¹ for the PPy and PPy/CS, respectively. The advantage of PPy/CS composite electrode over the pure PPy electrode is evident. The improved hydrophilicity improved the infiltration of electrolyte ions, resulting in better utilization of the active materials (Pan et al., 2010). **Figure 5.5c** shows plot of specific capacitance verses current density of the PPy and PPy/CS electrodes. The PPy/CS composite electrode performed better than the PPy electrode at various current densities. It is noteworthy that a specific capacitance as high as at 215 A g⁻¹ can still be obtained for PPy/CS at 10 A g⁻¹, indicating good electrode wettability that enables rapid and effective interaction between electrolytes ions and electrode even at high scan rates. This desirable property allows the electrode to operate at a wide range of current densities. **Figure 5.5d** shows the CV curves of PPy/CS composite electrode obtained at various scan rates. The nearly rectangular CV profiles at various scan rates indicate good capacitive nature with good ion response (Zhang et al., 2011).

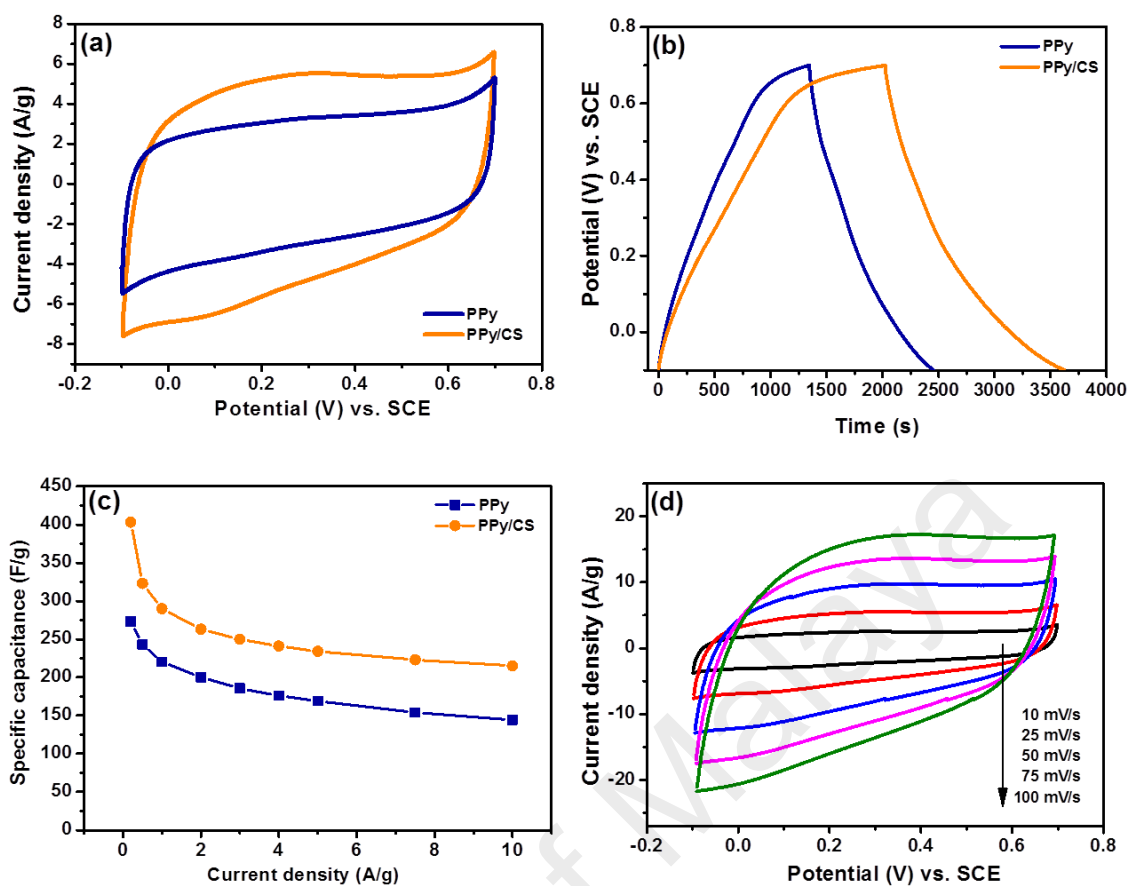


Figure 5.5: (a) CV curves at 25 mV s^{-1} , (b) GCD curves at 0.2 A g^{-1} , (c) dependence of specific capacitance on current density for PPy and PPy/CS nanocomposite electrode, and (d) CV curves of PPy/CS nanocomposite electrode as a function of scan rate.

Further optimization of CS with PPy is vital toward designing commercially feasible PPy/CS nanocomposite electrodes. On that account, the electrochemical performances of the PPy/CS nanocomposite electrodes prepared using different weight percentages of CS in the deposition solution were investigated. As shown in **Figure 5.6**, the observed results clearly revealed that the specific capacitance increased from 325 to 403 F g^{-1} when the CS content was increased from 0.5 to 0.75 wt\% , as a result of the increased hydrophilicity. Then, a further increase of the CS content attenuated the charge storage performance of the nanocomposite electrodes, which led to the decrease in specific capacitance. It is observed from the water contact angle measurement that CS

effectively increases the wettability of the electrodes; however, the CS biopolymer is not a conductive material (Yin et al., 2010). The high CS content beyond 0.75 wt% in the nanocomposite will lower the conductivity of the electrode to such a great degree that the increased hydrophilicity can no longer enhance the specific capacitance anymore and hence the importance of optimizing the CS content in the nanocomposite.

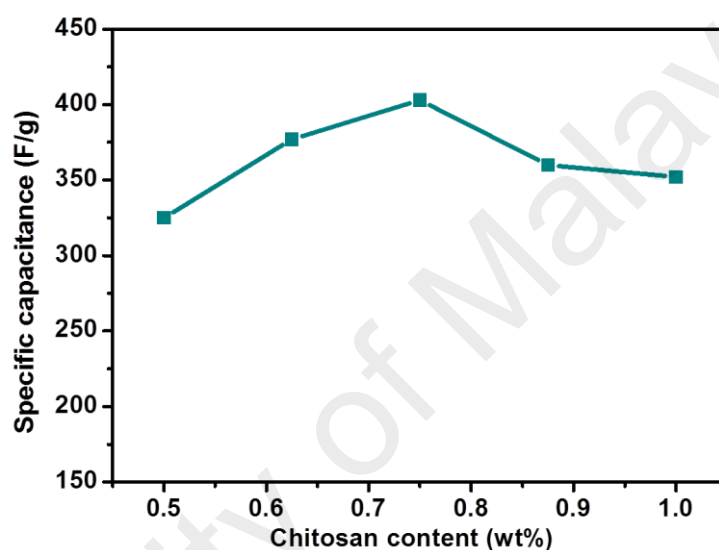


Figure 5.6: Specific capacitance values for different CS content calculated at current density of 0.2 A g^{-1} .

5.2.6 Supercapacitor device performance of PPy/CS nanocomposite electrode

In order to completely determine the electrochemical performance and the potential applications of the as-prepared composite electrodes, we assembled symmetrical supercapacitor devices based on the PPy/CS and PPy electrodes. The electrochemical impedance spectra (EIS) of the electrodes were carried out to study the effect of different CS contents on the impedance of the electrode. The Nyquist plots of EIS for the as-fabricated symmetric supercapacitors of PPy and PPy/CS nanocomposites electrode are shown in **Figure 5.7**. The equivalent series resistance

(ESR) can be obtained from the intercept at the real axis and it represents a combinational resistance of the ionic resistance of electrolyte; the intrinsic resistance of the active material; and the contact resistance between the active material, electrolyte and the current collector (Pusawale et al., 2013). The ESR of the PPy and PPy/CS nanocomposite electrodes (0.5, 0.75 and 1.0 wt%) were determined to be 0.30, 0.20, 0.22 and 0.22 Ω ; respectively. The charge transfer resistance (R_{ct}) can be estimated from the diameter of the semicircle. From the Nyquist plots, the R_{ct} value of PPy is only 2.90 whereas the R_{ct} values for all the PPy/CS nanocomposite electrodes increases from 3.20 to 6.18 Ω when the CS content was increased from 0.5 to 1.0 wt%. This increased in the R_{ct} value stems from the nonconductive CS in the nanocomposite (Yin et al., 2010). The corresponding ESR and R_{ct} values of the electrodes are summarized in **Table 5.1**.

As observed, the presence of CS in the nanocomposite increases the R_{ct} value; however, the ESR of the PPy/CS nanocomposite electrodes is lower than the PPy. This interesting feature is caused by the increased hydrophilicity of the electrode that facilitates the electrode/electrolyte interaction which reduces the contact resistance between the electrode and the aqueous electrolyte (Erdenedelger et al., 2014). Yu *et al.* also observed similar Nyquist plots with increased R_{ct} but reduced ESR values for their CS-Fe₃O₄ nanocomposite (Yu et al., 2011). These results also indicated that the CS was successfully incorporated into PPy to form PPy/CS nanocomposites.

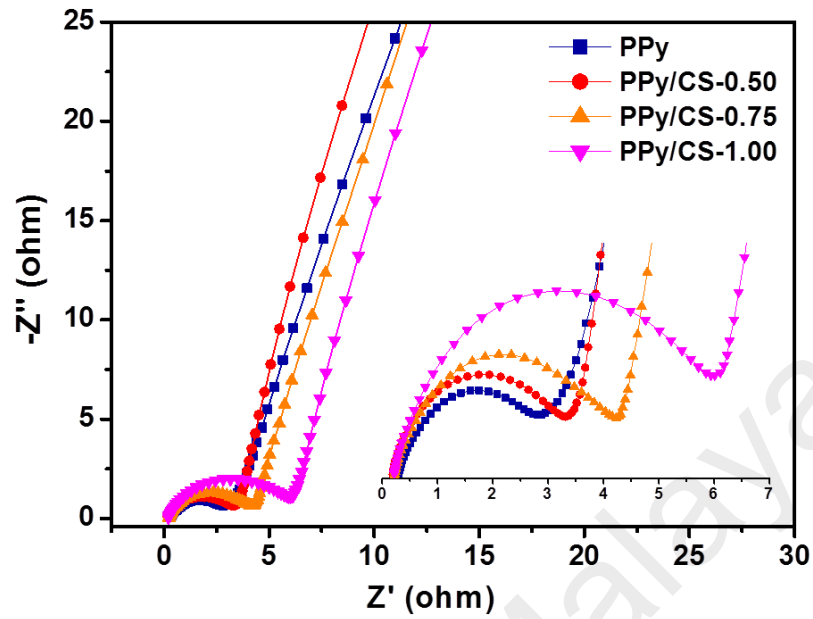


Figure 5.7: Nyquist plots of EIS for the as-fabricated symmetric supercapacitors of PPy and PPy/CS nanocomposite electrodes at 0.50, 0.75 and 1.0 wt% chitosan.

Table 5.1: The ESR and R_{ct} values of the symmetric supercapacitors of PPy and PPy/CS nanocomposites obtained from Nyquist plot.

Electrodes	ESR (Ω)	R_{ct} (Ω)
PPy	0.30	2.90
PPy/CS-0.50	0.20	3.20
PPy/CS-0.75	0.22	4.08
PPy/CS-1.0	0.22	6.18

The cyclic voltammograms of the PPy/CS symmetric supercapacitor is shown in **Figure 5.8a**. Rectangular-like shapes are observed even at a high scan rate of 200 mV s^{-1} , indicating ideal capacitive behavior. **Figure 5.8b** shows the GCD curves of the PPy/CS composite electrode at various current densities. The highly symmetrical charge/discharge curves indicated excellent reversibility. The specific capacitance calculated from the discharging curve is 146 F g^{-1} at a current density of 0.2 A g^{-1} while specific capacitance of 96 F g^{-1} was obtained for the PPy electrode at the same current density (**Figure 5.8c**). The PPy/CS symmetric supercapacitor gives good electrolyte affinity, resulting in an upsurge of electrolyte penetration into the surface layer, render its high specific capacitance (Yoo et al., 2014). As expected the specific capacitance decreased at higher current densities was due to the limited diffusion on the electrode surface (Huang et al., 2012).

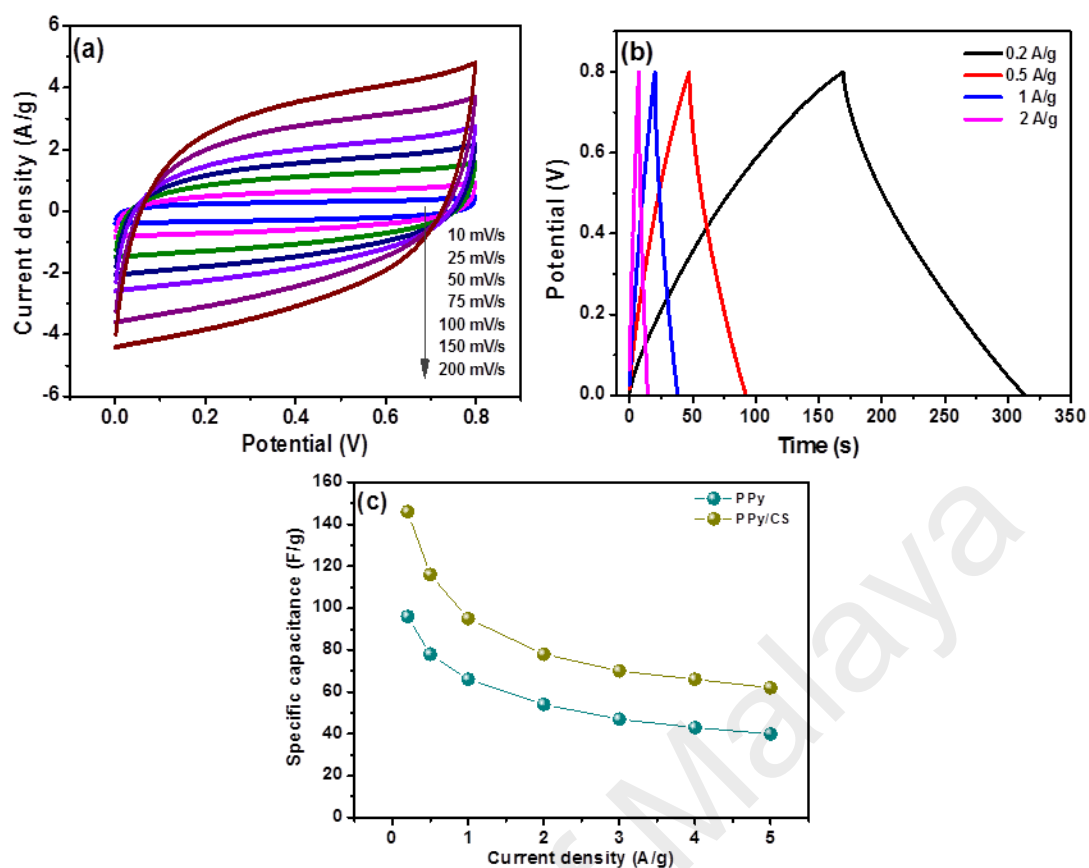


Figure 5.8: (a) CV curves at various scan rates, (b) GCD curves at various current densities of the PPy/CS symmetric supercapacitor, and (c) comparison of the dependence of specific capacitance on current density of the PPy and PPy/CS symmetric supercapacitor.

Figure 5.9a shows the Ragone plots of the symmetric supercapacitors that were calculated from the specific capacitance obtained from GCD measurements. A high power density of 6300 W kg^{-1} was achieved with energy density of 3.4 W h kg^{-1} and still maintained its power density of 316 W kg^{-1} with energy density of 12.6 W h kg^{-1} . On the other hand, the highest energy and power density reached by the PPy electrode is 8.6 W h kg^{-1} and 4000 W kg^{-1} , respectively. The result demonstrated the improved energy and power density from PPy.

Cycling stability is another critical factor for the commercialization of supercapacitor materials and is shown in **Figure 5.9b**. The specific capacitance increased rapidly in the first 100 cycles due to the good water absorbency character of CS that is capable to hydrate the internal volume of the electrode (Huang et al., 2013). The specific capacitance then decreased after this, but still retained up to 94.0% of its initial capacitance after 1000 cycles, whereas the PPy electrode only retained 88.8% of its initial capacitance. The improved electrochemical stability of the PPy/CS nanocomposite electrode is mainly due to the addition of CS in the polymer matrix that can partly prevent PPy component from severely swelling and shrinking during cycling, owing to the high mechanical strength of CS (Li et al., 2011). These results demonstrated that the addition of CS effectively enhanced the electrochemical stability of PPy.

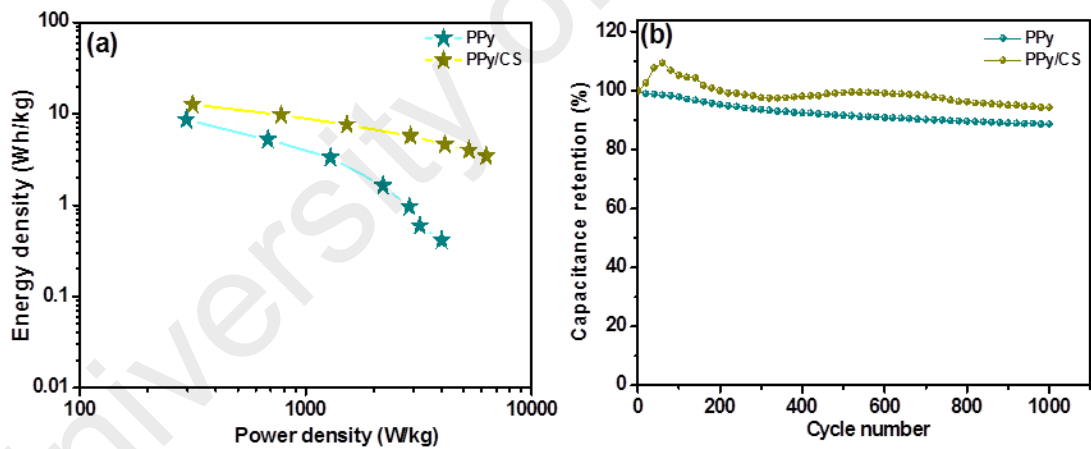


Figure 5.9: (a) Ragone plots, and (b) cycling stability plots for the symmetric supercapacitors of PPy and PPy/CS.

5.3 Conclusion

In this work, we demonstrated a facile strategy for the synthesis of PPy/CS nanocomposite. The deposition of CS under anodic potentials is made possible with the presence of pyrrole in the deposition solution. The improved specific capacitance and rate-capability of the PPy/CS nanocomposite electrode is undoubtedly due to the contribution of the hydrophilic CS biopolymer in the PPy/CS nanocomposite electrode. The enhanced hydrophilicity enables easy access of the solvated ions to the electrode/electrolyte interface, thereby reducing the contact resistance between the electrode and the electrolyte. Furthermore, the greater wettability of the PPy/CS nanocomposite electrode improved the infiltration of the electrolyte ions, resulting in better utilization of the electroactive PPy. Owing to its unique properties, the PPy/CS nanocomposite electrode shows the promise as an electrode material for high-performance supercapacitors.

CHAPTER 6

HYBRID SILVER NANOPARTICLE/NANOCLUSTER-DECORATED POLYPYRROLE FOR HIGH-PERFORMANCE SUPERCAPACITORS

6.1 Introduction

Supercapacitors or electrochemical capacitors have a wide array of applications, including starters, consumer electronics, military defence systems and power back-up systems (Calvo et al., 2013; Zhang et al., 2012). Supercapacitors have attracted great attention due to their superior fast charging and discharging process, long cycle life and environmental friendliness (Shen et al., 2013; Simon & Gogotsi, 2008; Vidhyadharan et al., 2014). They offer a higher energy density than conventional capacitors and a higher power density than batteries (You et al., 2014).

Supercapacitors can be classified into two categories; electric double layer capacitors (EDLC) and pseudocapacitors. EDLC store charges by non-faradaic charge separation at the electrode/electrolyte interface. Carbon-based materials are usually employed as electrode materials in EDLC. On the other hand, pseudocapacitors undergo fast and reversible faradaic reaction between electrolyte and electrode. Recently, much attention has been shifted to pseudocapacitors as they possess relatively higher capacitances as compared to carbon-based materials (Conway et al., 1997). The charge storage mechanisms of pseudocapacitors are based on the faradaic redox reactions that occur at the interface between the electrode and electrolyte. Pseudocapacitor materials include conducting polymers like polypyrrole (PPy), polyaniline (PANI) and several transition metal oxides, including V_2O_5 (Kim et al., 2012), NiO (Cheng et al., 2013), MnO_2 (Wang et al., 2011), and Co_3O_4 (Jagadale et al., 2014). Among pseudocapacitor

materials, conducting polymers offer the advantages of higher charge density compared to carbon materials and lower cost in contrast to metal oxides (Patil et al., 2013).

Among the available conducting polymers, PPy is one of the most studied conducting polymers as pseudocapacitor materials. PPy, which contains a conjugated structure of alternating C=C double bonds has recently garnered much attention due to its greater degree electrochemical processing flexibility, light weight, and high electrical conductivity than most other commercially available conducting polymers (Hepowit et al., 2012). The main drawback of using conducting polymers as supercapacitor electrodes is their poor stability during cycling when used as bulk materials. The conducting polymers films undergo swelling, shrinking, cracks or breaking during the doping-dedoping process (insertion/deinsertion of counter ions). These processes gradually aggravate their conducting properties (Frackowiak et al., 2006; Simon & Gogotsi, 2008). To overcome this problem, researches have focused on synthesizing PPy/carbon based composites such as activated carbon (Keskinen et al., 2015), carbon nanotubes (Oh et al., 2008), and graphene (Wang et al., 2012). Also, the synergistic effects of PPy/metal oxides composite electrodes have been applied as electrode for supercapacitor applications (Yao et al., 2013; Zhou et al., 2013). Another effective way to enhance the electronic conductivity of PPy is by metal doping (García-Fernández et al., 2015; Wysocka-Żołopa et al., 2013).

Recently, PPy hybrids with silver have been prepared from various methods for different application studies. Zhao *et al.* have synthesized nanofiber-like Ag@PPy core-shell structure from silver nitrate and pyrrole in the presence of sodium dodecyl benzyl sulfonate (SDBS). They investigated the effects of the concentration of SDBS on the morphology and the electrical conductivity of the composites (Zhao & Nan, 2012). PPy-Ag nanowire has been synthesized by Hnida *et al.* via cathodic co-deposition and its use in hydrogen peroxide sensing (Hnida et al., 2013). Yang *et al.* have reported the

formation of PPy-Ag composite nanotubes in the presence of polyvinylpyrrolidone (PVP) and its chemiresistor response to ammonia (Yang et al., 2010).

PPy/Ag composites used as electrode materials for supercapacitors applications are worthwhile to explore considering the highly electrically conductive Ag metal that may mediate the effective charge migration through the PPy. However, there have been a limited number of studies on the supercapacitor application of PPy/Ag composites. In a recent study, Patil *et al.* synthesized PPy/polyacrylic acid (PAA)/Ag composite electrodes for supercapacitor application (Patil et al., 2013). The PPy/PAA/Ag electrodes were prepared via a series of steps involving the polymerization of pyrrole using oxidant, preparing a solution mixture of PPy, PAA and silver nitrate, followed by dip coating of the substrate into the solution mixture. Although supercapacitance of the composite electrode was enhanced due to the incorporation of Ag, the pre-synthesized PPy bulk particles do not have sufficient surface area for the incorporation of Ag nanoparticles on a nanoscale level as only the outer surface of the PPy particles are decorated with Ag nanoparticles. This approach reduces the practical specific capacitance of the PPy. Hence, substantial improvements have to be made for its commercialization.

In this study, we report a facile route to synthesize a unique hybrid Ag nanoparticle/nanocluster-decorated PPy electrode. Herein, we report for the first time the formation of hybrid Ag nanoparticle/nanocluster compositing with PPy via *in-situ* redox reaction followed by electrodeposition. The influence of the AgNO_3 concentrations on the formation of Ag nanoparticle/nanocluster and their electrochemical performances were also investigated. Three- and two- electrode configurations were used to study the electrochemical performances of the hybrid Ag@PPy nanocomposite electrodes.

6.2 Results and Discussion

6.2.1 Synthesis and formation mechanism

In this study, the formation of the Ag@PPy nanocomposite took place via a facile *in-situ* redox reaction of pyrrole and AgNO₃, in which the Ag⁺ was reduced to Ag and pyrrole was oxidized to PPy in the absence of any stabilizer or surfactant. The recent work of Amarnath *et al.* showed that pyrrole can act as a reducing agent (Amarnath *et al.*, 2011). When AgNO₃ is added into the pyrrole solution, pyrrole monomers will oxidize to form the radical cations of pyrrole monomer, releasing free electrons during the process. The Ag⁺ ions are subsequently reduced to Ag particles by the free electrons released during the formation of free radicals. The coupling process between two cation radicals followed by the expelling of two protons resulted in the generation of an aromatic dimer. The propagation step continues via the oxidation, coupling and deprotonation processes. Even though the reaction mixture of pyrrole and AgNO₃ was only allowed to stir for 5 min, color change can already be observed in the reaction vessel as shown in **Figure 6.1**. We believe that it is due to the formation of pyrrole oligomers. The stirring time is kept short to prevent the oligomers from propagating into solid PPy, as solid PPy is not suitable for electrodeposition. Finally, the propagation step is continued via electrodeposition to deposit Ag@PPy nanocomposite onto a graphite sheet.

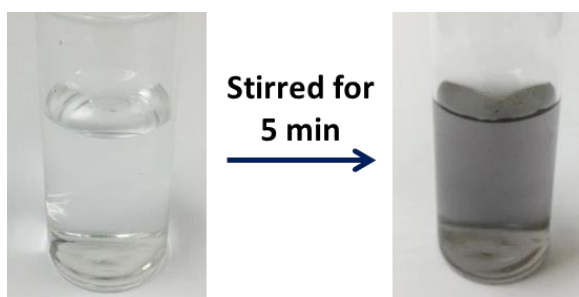


Figure 6.1: Physical appearance of the reaction mixture after stirring for 5 min prior to electrodeposition.

6.2.2 FTIR and Raman analysis

Figure 6.2a shows the FTIR spectrum of the Ag@PPy nanocomposite. The N–H and C–H stretching peaks were located at 3340 and 3000 cm^{-1} , respectively. The band at 1622 cm^{-1} was corresponded to the C=C vibration of the pyrrole ring, while the band at 1399 cm^{-1} was contributed by the pyrrole ring vibration. C–H in-plane deformation can be observed at 1260 cm^{-1} (Zang & Li, 2011). The bands at 1096 and 982 cm^{-1} can be attributed to N–H in-plane deformation vibration and the C–H out-of-plane vibration, respectively, implying the doping state of PPy (Li et al., 2010).

The Raman spectra of pure PPy and Ag@PPy are shown in **Figure 6.2b**. The characteristic bands at 1575 and 1385 cm^{-1} are assigned to the ring stretching mode and C=C backbone stretching of PPy, respectively. For the pure PPy, the band at 1055 cm^{-1} is attributed to the symmetrical C–H in plane bending. In addition, the two bands at 975 and 935 cm^{-1} are due to the bipolaron ring and polaron structure (Gu et al., 2010). The characteristics absorption peaks of PPy are also exhibited in Ag@PPy with little alteration of the bands, which indicates the presence of the unchanged internal structure of the PPy in the composite.

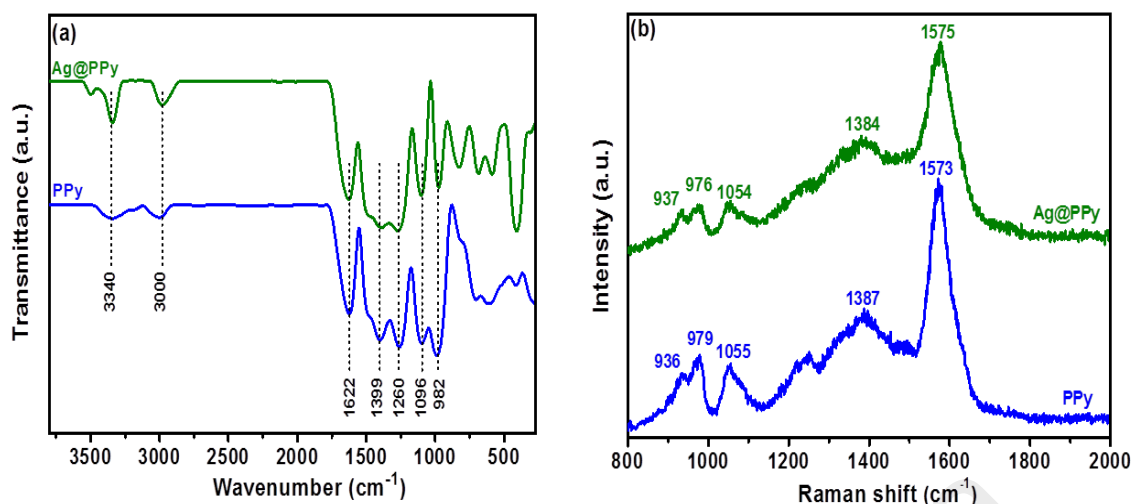


Figure 6.2: (a) FTIR and (b) Raman spectra of PPy and Ag@PPy.

6.2.3 Morphological studies of Ag@PPy nanocomposite

Figure 6.3 shows the FESEM morphologies of the as-prepared samples. **Figure 6.3a** shows the silver-free PPy film had typical cauliflower morphology and the higher magnification image shows a smooth PPy without any embedment of Ag nanoparticles. For 0.01M-Ag@PPy, small spherical Ag nanoparticles can be clearly seen on the surface of PPy as shown in **Figure 6.3b**. Surprisingly, when the concentration of AgNO₃ increased to 0.05 M, two different sizes of Ag were observed; Ag nanoparticles and Ag nanoclusters. The Ag nanoclusters with particle size ranging from 55-100 nm can be seen decorated evenly alongside the small Ag nanoparticles on the PPy film (**Figure 6.3c**). We deduce that the small Ag nanoparticles were already formed during the initial redox reaction between pyrrole and Ag⁺ ions prior to electrodeposition. During electrodeposition, the oxidizing role of Ag⁺ ions is replaced by the electrode oxidation process on the substrate when potential is applied. The excess Ag⁺ ions will selectively adsorbed onto the Ag nanoparticles surfaces because of ionic adsorption effect (Patil et al., 2013) and is subsequently reduced to Ag nanoclusters from the free electrons released during the continuous formation of radical pyrrole cations. The Ag

nanoclusters tend to have irregular shapes with increased in their sizes when the AgNO_3 concentration was further increased to 0.10 M as depicted in **Figure 6.3d**. Elemental mapping was performed on the 0.05M-Ag@PPy nanocomposite, as shown in **Figure 6.3e**. The areas of bright contrast correlate to the distributions of C, N and Ag in the nanocomposite. The model for the formation of different Ag@PPy nanocomposite is shown in **Figure 6.4**.

University of Malaya

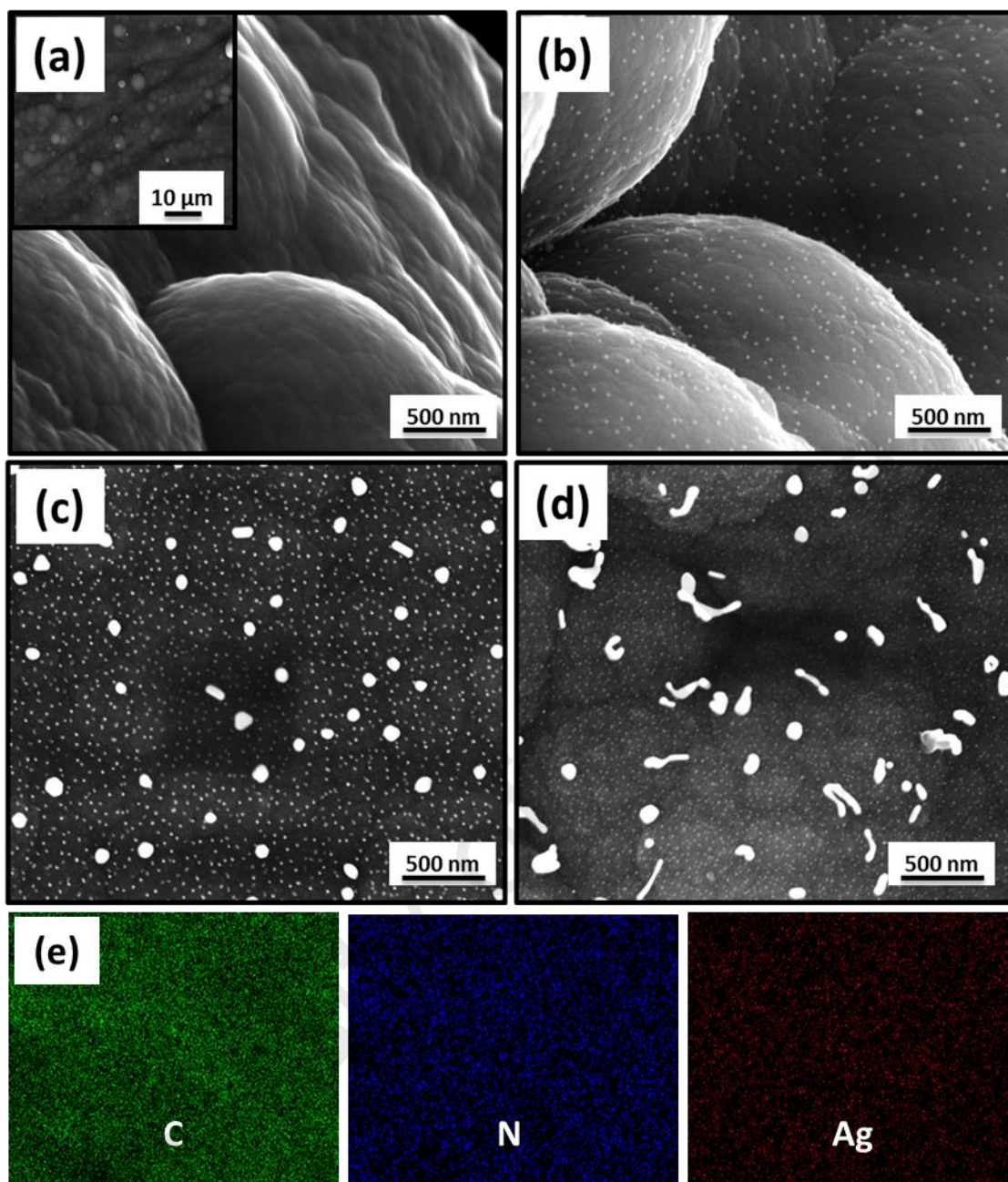


Figure 6.3: FESEM images of (a) pure PPy, inset showing PPy at lower magnification; Ag@PPy nanocomposites with AgNO₃ concentrations of (b) 0.01 M, (c) 0.05 M, (d) 0.10 M, and (e) elemental mapping of the 0.05M-Ag@PPy nanocomposite.

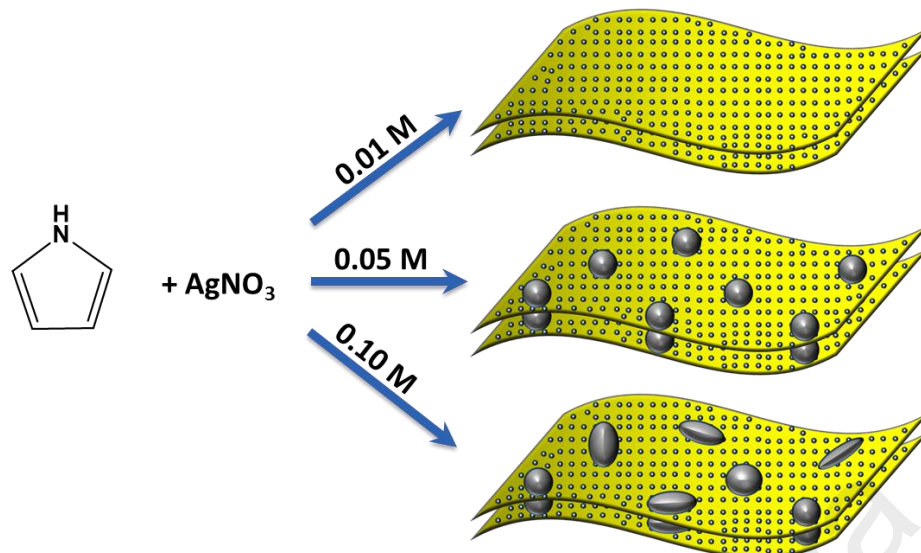


Figure 6.4: Schematic representation of the evolution of different Ag@PPy nanocomposites.

HRTEM images of the 0.05M-Ag@PPy nanocomposite are shown in **Figure 6.5**. The Ag nanoclusters and Ag nanoparticles can be clearly seen in **Figure 6.5a** and **b**, respectively. **Figure 6.5b** clearly shows the deposition of distributed ultra-small Ag nanoparticles having a size range of 2-4 nm on the surface of the PPy film.

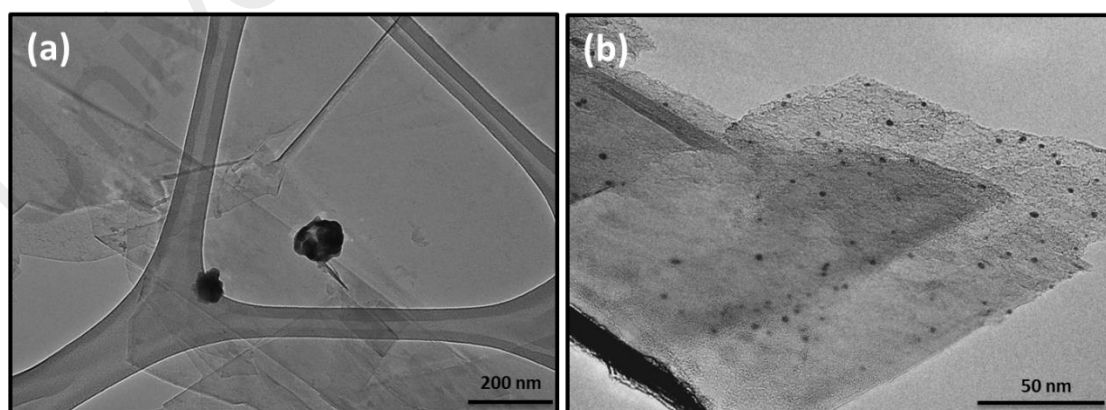


Figure 6.5: HRTEM images of (a) Ag nanoclusters and (b) Ag nanoparticles.

6.2.4 XPS analysis of hybrid Ag@PPy nanocomposite

XPS was used to characterize the chemical state of the as-prepared hybrid Ag@PPy nanocomposite and is shown in **Figure 6.6**. The N 1s core level spectrum of the Ag@PPy nanocomposite could be deconvoluted into three peaks as shown in **Figure 6.6a**. The main peak at 399.1 eV was attributed to the neutral amine nitrogen (N–H). The peak at higher binding energy of 400.3 eV corresponds to the positively charged nitrogen ($-N^+$). Another peak at the lower binding energy side (397.9 eV) can be assigned to the imine nitrogen ($-N=$) (Cao et al., 2015). The Ag 3d core level spectrum of the Ag@PPy nanocomposite is shown in **Figure 6.6b**. Two peaks are observed at 368.0 and 374.1 eV with 6.1 eV spin energy separations, corresponding to the binding energies of the Ag 3d_{5/2} and Ag 3d_{3/2} core levels, respectively (Babu et al., 2012). The XPS analysis provided support for the existence of metallic silver in the nanocomposite materials.

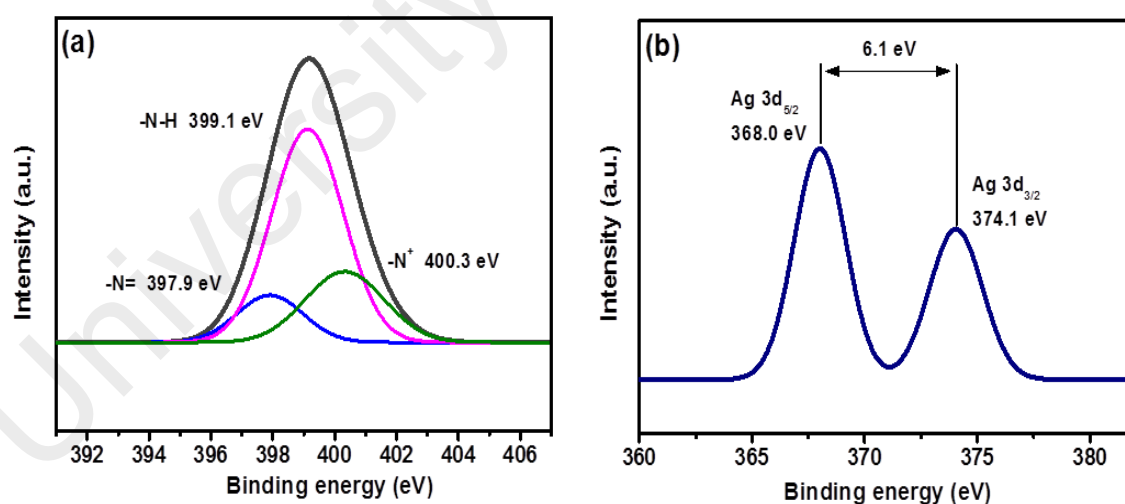


Figure 6.6: XPS spectra of Ag@PPy nanocomposite at (a) N 1s and (b) Ag 3d core level spectra.

6.2.5 Electrochemical characterizations of Ag@PPy nanocomposite

Cyclic voltammetry (CV) was used to evaluate the electrochemical performances of the as-prepared PPy and Ag@PPy nanocomposite electrodes. **Figure 6.7a** shows the CV curves of the electrodes in 1.0 M H₂SO₄ electrolyte at a scan rate of 10 mV s⁻¹. It is apparent that the peak current was greatly enhanced for the Ag@PPy nanocomposite electrode as compared to that for the pure PPy electrode. No well-defined peaks were observed for the PPy electrode. Interestingly, two pairs of redox peaks were observed for the Ag@PPy nanocomposite electrode. For the Ag nanoparticles, the oxidation peak was observed at 0.19 V while the minute reduction peak was observed at around 0.01 V (Patil et al., 2012). The second pair of redox peak was attributed by the oxidation and reduction of Ag nanoclusters, having broad anodic and cathodic peaks situated at 0.50 and 0.20 V, respectively (Wei et al., 2013). Here we observed that redox behavior is affected by size. Also, the separation between the anodic and cathodic peaks increases with the size of Ag particles. These observations are in good agreement with previous studies (Chaki et al., 2004; Ivanova & Zamborini, 2010). The CV results imply the presence of hybrid Ag nanoparticles and Ag nanoclusters in the Ag@PPy nanocomposite.

Figure 6.7b shows the GCD curves of the pure PPy and the Ag@PPy nanocomposite electrodes at current density of 0.2 A g⁻¹. The GCD curve of Ag@PPy nanocomposite shows longer discharge time than the pure PPy, indicating that the Ag@PPy nanocomposite has better capacitance property than PPy. The specific capacitances of the electrodes were calculated from the GCD curves at current density of 0.2 A g⁻¹. A capacitance of 273 F g⁻¹ was found for the pure PPy and the capacitance improved to 414 F g⁻¹ with the incorporation of Ag nanoparticles and nanoclusters, which was almost a 52% increment in the specific capacitance. This shows that the

addition of Ag nanoparticles improved the electron transfer in the Ag@PPy system. The metallic conductor Ag nanoparticles mediate the electron hopping within the conjugated systems of the PPy chains, harnessing fully the capacitance properties of PPy while the anchored Ag nanoclusters acted as spacers to prevent the restacking of PPy films. Conversely, the thick and densely packed PPy electrode is undesirable for fast ion kinetics and attributes to decreased charge storage performance. The dependence of specific capacitance on current density for the PPy and hybrid Ag@PPy nanocomposite is shown in **Figure 6.7c**. It can be observed that the specific capacitance of the hybrid Ag@PPy nanocomposite is much higher than that of pure PPy at all current densities. The specific capacitance for the hybrid Ag@PPy nanocomposite at 10 A g^{-1} remained high at 206 F g^{-1} ; this desirable feature of the electrode allows it to operate at a wide range of current densities. It should be noted that the specific capacitance of 414 F g^{-1} of the optimized Ag@PPy nanocomposite electrode is higher than that of many previously reported Ag@PPy-based electrodes, such as PPy-Ag free standing porous films (282 F g^{-1} at 1 mV s^{-1}) (Singh et al., 2013) and PPy/Polyacrylic acid/Ag nanocomposite (226 F g^{-1} at 10 mV s^{-1}) (Patil et al., 2013).

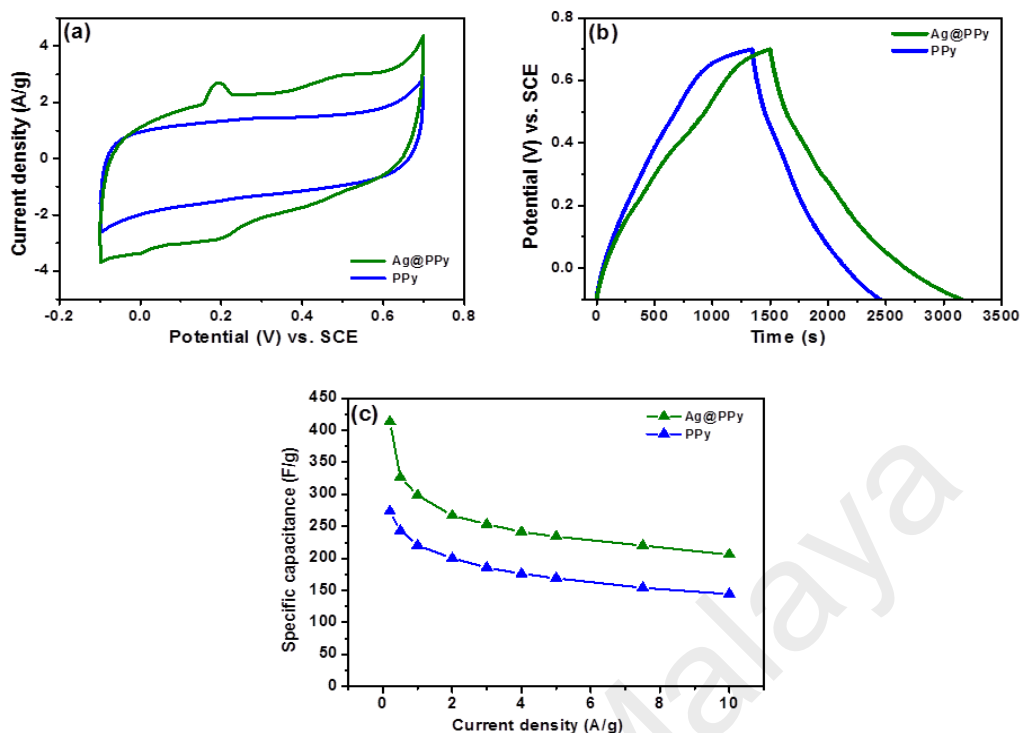


Figure 6.7: CV curves at 10 mV s^{-1} , (b) GCD curves at 0.2 A g^{-1} , and (c) dependence of specific capacitance on current density for PPy and hybrid Ag@PPy nanocomposite electrode.

To ascertain the applicability of the electrodes for high-performance supercapacitors, CV curves of PPy and hybrid Ag@PPy nanocomposite electrode were recorded and compared at various scan rates. **Figure 6.8a** and **b** show that the area under the curve increases as the scan rate increases. At their respective scan rates, the Ag@PPy nanocomposite electrode exhibited higher output current in comparison the PPy electrode, indicating an enhancement of charge storage in the composite electrode. Although the output currents of the PPy electrode was lower compared to that of the hybrid Ag@PPy nanocomposite electrode, the CV curves still exhibited quasi-rectangular shapes, revealing the good capacitance behavior and high-rate compatibility of PPy, making it a suitable platform for the anchoring of Ag nanoparticle/nanocluster. As shown in **Figure 6.8b**, with the increase of potential scan rate from 10 to 100 mV s^{-1} ,

the anodic peak potential shifted to higher potentials and the cathodic peaks shifted to lower potentials. This is mainly due to the resistance of the electrode (Yan et al., 2010). The shape of the CV curves was maintained even at high scan rates, indicating excellent capacitance behavior of the nanocomposite electrode.

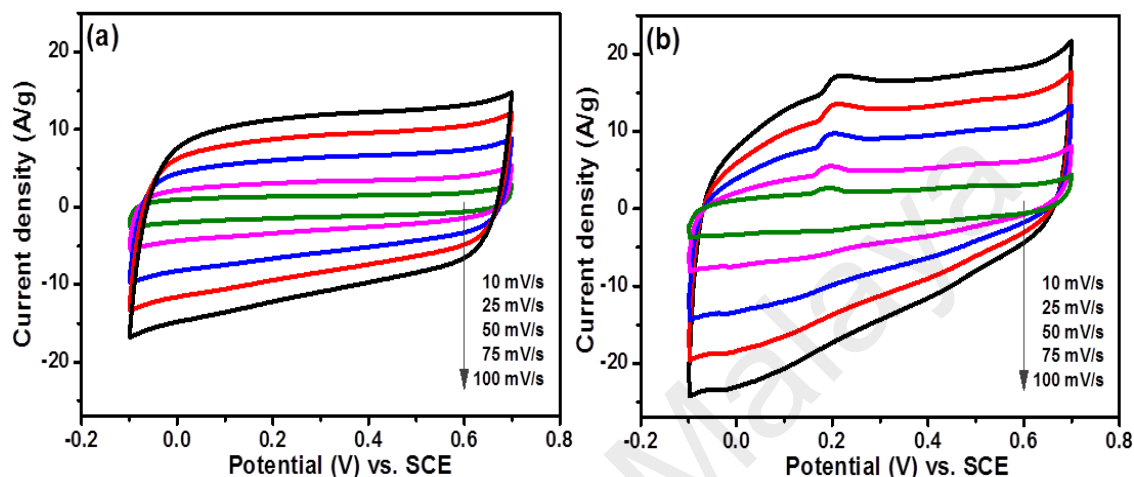


Figure 6.8: CV curves at various scan rates for (a) PPy, and (b) hybrid Ag@PPy nanocomposite electrode.

The optimization of Ag on PPy is essential from the economic and high-performance perspective for a supercapacitor. Hence, the electrochemical performances of the Ag@PPy nanocomposite electrodes prepared using different concentrations of AgNO₃ were evaluated. **Figure 6.9** shows the effect of AgNO₃ concentration on the electrochemical performance of nanocomposite. The specific capacitances increased from 273 F g⁻¹ to 414 F g⁻¹ when the AgNO₃ concentration was increased from 0 to 0.05 M. Then, a further increase in the AgNO₃ concentration eventually led to the decrease in specific capacitance. The decrease in the efficiency at high Ag loading is due to the free standing/excess Ag in the composite that may oxidized to Ag(I) and also may be eroded by the electrolyte (Lim et al., 2014). As seen from the FESEM results, the Ag@PPy prepared from 0.10 M AgNO₃ has irregular and large Ag nanoclusters anchored on the nanocomposite which may lead to a decrease in the active surface area

of PPy film, reducing its interaction with the electrolyte ions. Consequently, the overall supercapacitance performance of the electrode would have deteriorated.

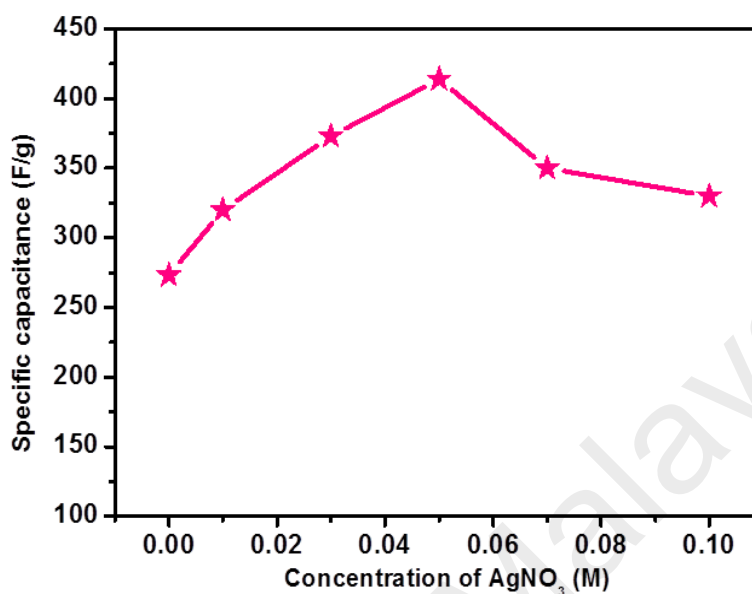


Figure 6.9: Specific capacitance values for different AgNO₃ concentrations calculated at current density of 0.2 A g⁻¹.

6.2.6 Supercapacitor device performance of hybrid Ag@PPy nanocomposite

A three-electrode system has heightened sensitivity to faradaic reaction that can lead to large deviation when projecting the energy storage capability of an electrode material (Stoller & Ruoff, 2010). To the best of our knowledge, there is no report on the electrochemical performance of a two-electrode system fabricated from Ag@PPy nanocomposite. We had made an attempt to fabricate a symmetrical two-electrode cell using hybrid Ag@PPy. **Figure 6.10a** shows the cyclic voltammograms of the symmetric supercapacitor device, which have a rectangular shape within the range of 0 to 0.8 V. The GCD curves of the hybrid Ag@PPy nanocomposite are shown in **Figure 6.10b**. The charging and discharging reveal symmetrical curves, signifying excellent reversibility. The specific capacitance obtained from the discharging curve is calculated

to be 161 F g^{-1} at a current density of 0.2 A g^{-1} . The high specific capacitance is ascribed to the unique hybrid Ag nanoparticle/nanocluster-decorated PPy nanocomposite. The highly conducting metallic Ag nanoparticles mediate the effective charge migration through the PPy, whilst Ag nanoclusters prevent the restacking of PPy films. Both hybrid Ag nanoparticle/nanocluster extend the active sites for redox reactions, leading to improved specific capacitance of the hybrid Ag@PPy electrode.

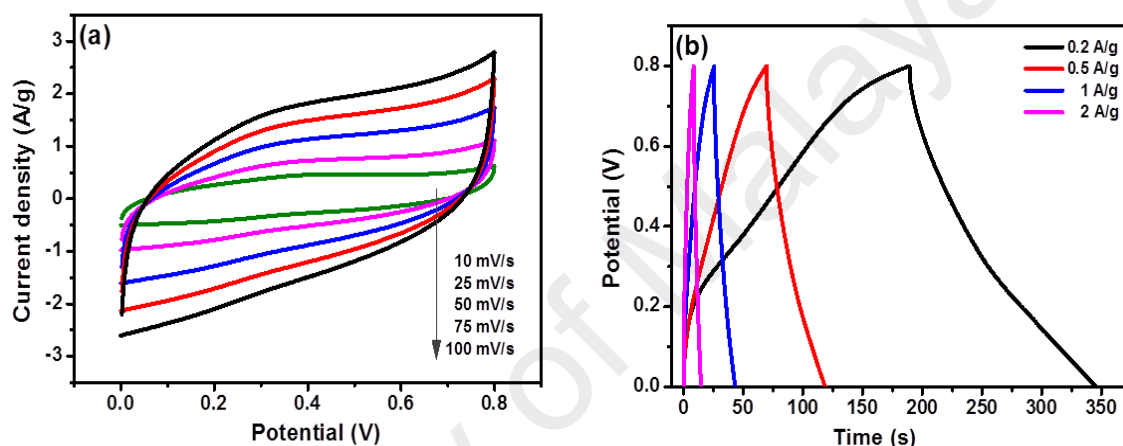


Figure 6.10: (a) CV at various scan rates and (b) GCD at various current densities of the as-fabricated symmetric supercapacitor of Ag@PPy nanocomposite.

The electrochemical impedance spectra (EIS) of the fabricated symmetric supercapacitors were recorded in a frequency range between 0.1 Hz and 100 kHz, as shown in **Figure 6.11**. The first intercept of the semicircle at the real axis in the high frequency region represents the equivalent series resistance (ESR), which is attributed to the resistance of the electrolyte; the contact resistance between the electrolyte, current collector, and active material; and the intrinsic resistance of the active material itself. The ESR values were determined to be 0.30 and 0.26 Ω for the PPy and hybrid Ag@PPy nanocomposite electrode, respectively. The charge transfer resistance (R_{ct}) can be estimated from the diameter of the semicircle. From the Nyquist plot, the R_{ct} values

of PPy and hybrid Ag@PPy nanocomposite and 2.90 and 0.82 Ω , respectively. The remarkably reduced R_{ct} is the result of the integration of metallic silver into PPy. This desirable feature effectively enhanced the electron hopping system of the PPy, resulting in better utilization of the PPy.

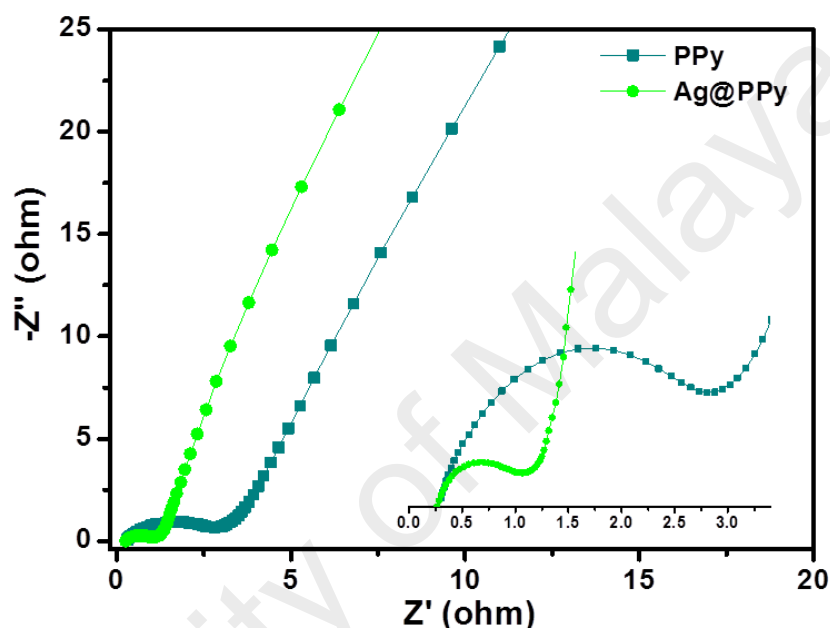


Figure 6.11: Nyquist plots of EIS for the symmetric supercapacitors of PPy and hybrid Ag@PPy nanocomposites. Inset is a magnified portion of the high-frequency region.

The Ragone plot shows the dependence between the power output and energy density of the symmetric supercapacitor device (**Figure 6.12a**). The energy density of the hybrid Ag@PPy nanocomposite decreased from 13.6 to 2.6 W h kg^{-1} as the power density increased from 312 to 5850 W kg^{-1} . On the other hand, the highest energy and power density reached by the PPy electrode is 8.6 W h kg^{-1} and 4000 W kg^{-1} , respectively. The result demonstrated the improved energy and power density from PPy. Cycling stability is essential for the commercialization of supercapacitor materials. **Figure 6.12b** shows the capacitance retention as a function of the cycle number at a

current density of 0.5 A g^{-1} for 1000 cycles. The hybrid Ag@PPy nanocomposite exhibited remarkable cycling stability and retained up to 98.9% of its initial capacitance after 1000 charge/discharge cycles, whereas the PPy electrode only retained 88.8% of capacitance. These results show that the addition of hybrid Ag particles enhanced the cycling stability of PPy.

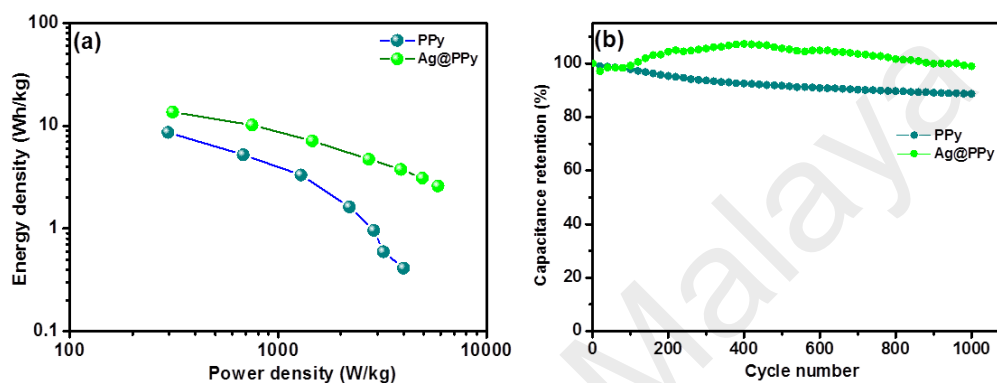


Figure 6.12: (a) Ragone plot, and (b) cycling stability of the symmetric supercapacitors of PPy and hybrid Ag@PPy nanocomposite.

6.3 Conclusion

This work featured a facile strategy for the synthesis of hybrid Ag nanoparticle/nanocluster-decorated PPy nanocomposites. The FESEM images showed that the best combination of nanoparticles and nanoclusters are formed at the optimized concentration of 0.05 M AgNO_3 . When lower concentration was used, no Ag nanoclusters were found, while at higher concentration, many Ag nanoclusters agglomerated with irregular shapes were observed. The improved capacitance and rate-capability of the hybrid Ag@PPy can be accredited to its unique architecture. Firstly, the 2-4 nm Ag nanoparticles that are evenly distributed on PPy effectively enhanced the electron hopping system of the conjugated PPy, thereby increasing the capacitance of the PPy. Secondly, the larger Ag nanoclusters with a size range of 55-100 nm were

uniformly adhered to the PPy film acted as spacers, preventing the PPy films from restacking. Thirdly, the enhanced morphology shortened the transport pathway for electrons and gave better cycling stability. Benefiting from its splendid characteristics, the hybrid Ag nanoparticle/nanocluster-decorated PPy nanocomposite was shown to exhibit a significantly improved electrochemical performance.

University of Malaya

CHAPTER 7

BOOSTING THE SUPERCAPACITIVE PROPERTIES OF POLYPYRROLE WITH CHITOSAN AND HYBRID SILVER NANOPARTICLE/NANOCLUSTER

7.1 Introduction

The increasing demand for energy has triggered enormous research activities for energy storage and conversion from clean and renewable energy sources. Electrochemical capacitors, also known as supercapacitors, are promising energy storage devices for many applications including portable power systems, hybrid electric vehicles, consumer electronics, and power back-up systems (Calvo et al., 2013; Zhang et al., 2012).

Generally, supercapacitors are classified into two types; (i) electric double layer capacitors (EDLC), which are carbon-based materials that depend on the non-faradaic charge separation at the electrode/electrolyte interface, and (ii) pseudocapacitors, which are made of metal oxides and conducting polymers, undergo faradic charge transfer across the active material of the electrodes. The conducting polymer, polypyrrole (PPy) is particularly promising and one of the most widely used polymers owing to its good electrical conductivity, ease of low cost synthesis, environmental stability and electrochemical processing flexibility (Biswas & Drzal, 2010; Hepowit et al., 2012).

Recently, researches have shifted their focuses on the synthesis of PPy composites electrode in order to reinforce the stability of the PPy composite as well as to improve the capacitance of PPy. Hybrids of PPy that combines carbonaceous materials or metal oxides with PPy include graphene (Davies et al., 2011), carbon nanotubes (Raicopol et al., 2013) activated carbon (Keskinen et al., 2015), carbon

aerogel (An et al., 2010), MnO₂ (Bahloul et al., 2013), and CoO (Zhou et al., 2013) have been widely studied. These composites are usually done by combining the different classes of supercapacitors i.e., EDLCs and pseudocapacitors, that enhanced the electrochemical performance of PPy.

Another effective way that is worthwhile to explore is by incorporating the highly conductive metallic silver into the structures of PPy to assist the electron transport throughout the conjugated system of PPy. Zhao *et al.* studied the effect of different morphologies of Ag@PPy core-shell structures on the electrical conductivity of the composite (Zhao & Nan, 2012). The formation of Ag@PPy composite nanotubes by Yang *et al.* showed improved chemiresistor response towards ammonia due to better charge transmission in the nanocomposite (Yang et al., 2010). There are limited studies on Ag@PPy for supercapacitors applications. In a recent study by Patil *et al.*, PPy/polyacrylic acid (PAA)/Ag nanocomposite electrodes have been synthesized for supercapacitor applications through the polymerization of PPy followed by dipping in a solution of PPy, PAA and silver nitrate (Patil et al., 2013). The nanocomposite achieved a maximum specific capacitance of 226 F g⁻¹ at 10 mV s⁻¹. In our previous report, we studied the effect of the concentration of silver nitrate on the electrochemical performance of Ag@PPy nanocomposite electrode. The unique architectures of hybrid Ag nanoparticle/nanocluster-decorated PPy and the reduced resistivity of the electrode gave a specific capacitance of 414 F g⁻¹ at 0.2 A g⁻¹ (Gan et al., 2015).

Besides increasing the electrical conductivity of PPy, excellent electrode wettability is also indispensable for producing outstanding supercapacitors. Many studies have demonstrated that the hydrophilicity of an electrode surface can enhance the supercapacitive properties of an active material (Erdenedelger et al., 2014; Navale et al., 2015; Pawar et al., 2012; Wang et al., 2012). An electrode with good wettability enables better infiltration of the electrolyte ions into the framework of the electrode. In

our previous study, PPy was composited with chitosan (CS) showed an improvement in the capacitance mainly due to the hydrophilic contribution by CS. Furthermore, CS is an attractive biomaterial with many unique properties such as environmental friendly nature, low cost, nontoxicity, high mechanical strength, and antimicrobial activity that have found its niche in a variety of applications (Ayad et al., 2014; Fusco et al., 2013; Koev et al., 2010; Sun et al., 2009; Zeng et al., 2009).

In the present investigation we attempt to combine the merits CS and Ag with PPy to further augment the supercapacitive characteristics of PPy. The roles of CS and Ag on the structural and electrochemical properties on the Ag@PPy/CS ternary nanocomposite were discussed. The electrochemical performance was first investigated using a three-electrode configuration followed by the fabrication of symmetric supercapacitor of Ag@PPy/CS.

7.2 Results and Discussion

7.2.1 Synthesis and formation mechanism

The Ag@PPy/CS nanocomposite electrode was formed via a facile and easily scalable electrodeposition method. The Ag@PPy/CS nanocomposite electrode was formed at selected chitosan content of 0.75 wt% and 0.05 M AgNO₃ which were the optimized concentrations to get the highest specific capacitance as reported in our earlier work. The as-prepared deposition solution was subjected to electrodeposition under a constant potential of +0.8 V to coat the Ag@PPy/CS nanocomposite onto a piece of graphite sheet. It is interesting to note that the reduction of Ag and the deposition of CS are only possible at negative potentials. However, they are also feasible under anodic potentials in the presence of pyrrole. In the former case, pyrrole acted as a reducing agent

(Amarnath et al., 2011) to reduce the Ag^+ ions to Ag. The redox reaction was initiated upon the introduction of AgNO_3 where pyrrole is oxidized to form radical cations of pyrrole monomers, the free electrons released during the formation of radicals caused the Ag^+ ions to reduce to Ag. The free electrons released from the polymerization of pyrrole during the electrodeposition step continue to reduce Ag^+ ions to Ag. In the latter case, the pyrrole monomers were entrapped in the CS biopolymer due to the hydrogen bonds formed between the hydroxyl and amine groups of CS with the amine group of pyrrole monomers. During the polymerization of pyrrole on the electrode surface, the attached pyrrole monomers on CS will be attracted to the electrode surface and propagate to form PPy/CS films with the simultaneous doping of Ag on the PPy/CS films, producing the Ag@PPy/CS nanocomposite electrode.

CS has also been reported to act as a reducing agent in either basic condition, heating, or both (Fang et al., 2015; Guo et al., 2012; Sanpui et al., 2008). The basic suspension and the degradation products of CS (e.g. glucosamide) during heating may supply electrons and function as a reducing agent (Twu et al., 2008). Since no base and heating were involved in this work, the role of CS as a reducing agent was unlikely. However, CS can act as a stabilizing agent, protecting the Ag particles from agglomeration (Akmaz et al., 2013; Wei et al., 2009).

7.2.2 FTIR and XPS analysis

Figure 7.1a shows the FTIR spectra of the CS, PPy, Ag@PPy, PPy/CS and Ag@PPy/CS nanocomposite. For the CS powder, the broad band around 3318 cm^{-1} is due to the stretching vibrations of the primary amine ($-\text{NH}_2$) and hydroxyl groups ($\text{O}-\text{H}$) in CS (Fusco et al., 2013). The bands at 2876 cm^{-1} and 1588 cm^{-1} were attributed to the aliphatic $\text{C}-\text{H}$ stretching and $-\text{NH}_2$ bending vibration, respectively (Koev et al., 2010).

C–O stretching mode of $-\text{CH}_2\text{-OH}$ group was observed at 1381 cm^{-1} whilst a broad peak at 1027 cm^{-1} was attributed to the C–O–C stretching (Li et al., 2011).

The spectra of PPy and Ag@PPy showed the typical N–H stretching at 3340 cm^{-1} , the peak located 3000 cm^{-1} was assigned to aromatic C–H stretching of the pyrrole ring and the peak at 1622 cm^{-1} was corresponded to the C=C vibration of the pyrrole ring. The peak at 1490 cm^{-1} was contributed by the C–N stretching vibration while the peak at 1415 cm^{-1} was due to the pyrrole ring vibration. Absorption bands at 1278 , 1094 and 990 cm^{-1} were corresponded to C–H in-plane deformation, N–H in-plane deformation vibration and the C–H out-of-plane vibration, respectively (Gu et al., 2010; Zang & Li, 2011).

The infrared spectrum of the PPy/CS and Ag@PPy/CS nanocomposites showed a broad absorption band centered around 3313 cm^{-1} due to the overlapping of N–H and O–H stretching vibration of CS with the amine group of PPy (Yalçinkaya et al., 2010). The absorption band corresponded to $-\text{NH}_2$ bending vibration in the CS at 1588 cm^{-1} was not observed in the PPy/CS and Ag@PPy/CS nanocomposite. Instead, a new peak attributed to the asymmetric NH_3^+ bending at 1649 cm^{-1} appeared in the CS nanocomposites, indicating the protonation of the amine group in the CS (Koev et al., 2010; Yamada & Honma, 2005). The CS in the nanocomposites remained protonated because the electrodeposition took place under an anodic potential of $+0.8\text{ V}$ in the presence of pyrrole. CS films that are electrodeposited under cathodic potentials will give deprotonated CS films. This is due to the fact that cathodic electrodeposition takes advantage of CS's pH dependent solubility. At negative potentials, the evolution of hydrogen leads to a locally high pH near the cathode surface. The CS becomes deprotonated and is no longer soluble under basic conditions, depositing CS films on the electrode (Koev et al., 2010; Luo et al., 2005).

Figure 7.1b shows the XPS spectroscopic analysis of core level spectra for Ag 3d of Ag@PPy and Ag@PPy/CS. The Ag 3d_{5/2} peak at 368.0 eV and Ag 3d_{3/2} peak at 374.1 eV with spin energy separations of 6.1 eV indicate the presence of metallic silver in the nanocomposite electrodes (Babu et al., 2012).

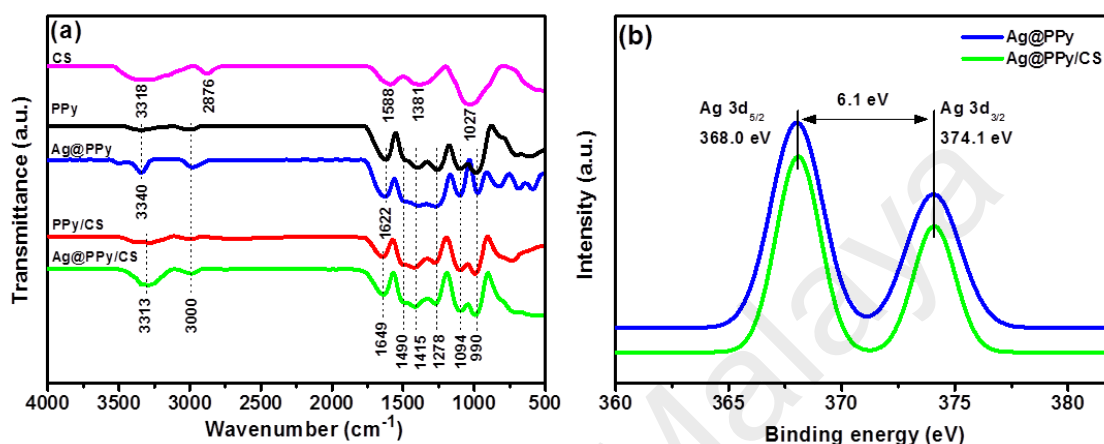


Figure 7.1: (a) FTIR of CS, PPy, Ag@PPy, PPy/CS and Ag@PPy/CS (b) XPS spectra of Ag@PPy and Ag@PPy/CS nanocomposite electrodes at Ag 3d core level spectra.

7.2.3 X-ray diffraction analysis

XRD patterns of the PPy nanocomposite electrodes as well as PPy and CS were shown in **Figure 7.2**. The diffraction pattern of PPy and its nanocomposites showed a broad peak at 21.9°, indicating that the electrodeposited PPy is in the amorphous phase. CS exhibited two peaks at 9.6° and 20.3° which are the typical fingerprints of CS. (Ayad et al., 2014) However, both characteristic peaks of CS were not observed in the nanocomposite (PPy/CS and Ag@PPy/CS) suggesting that the CS did not induce the phase change of PPy. When Ag is present, three diffraction peaks positioned at 38.1°, 44.3° and 64.4° can be indexed to the (1 1 1), (2 0 0) and (2 2 0) diffraction planes of metallic Ag (JCPDS no.89-3722), respectively. This also confirmed that the hybrid Ag particles are crystalline in nature. (Izrini et al., 2015)

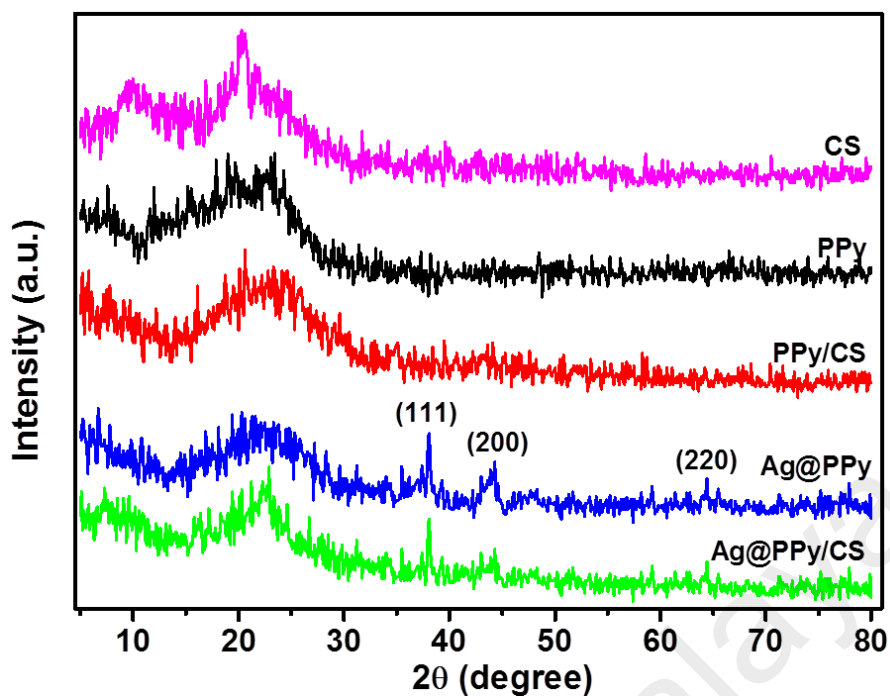


Figure 7.2: X-ray diffraction patterns of CS, PPy, PPy/CS, Ag@PPy and Ag@PPy/CS nanocomposites.

7.2.4 Morphological studies

Figure 7.3 shows the FESEM morphologies of the as-prepared samples. **Figure 7.3a** shows that the PPy electrode had the typical cauliflower morphology. Upon the addition of CS, the PPy/CS electrode surface appeared to be rougher with more noticeable protrusion of bulbous-like spheres compared to PPy as seen in **Figure 7.3b**. The morphology of Ag@PPy nanocomposite electrode is shown in **Figure 7.3c**. Two distinguishable sizes of Ag were observed; namely Ag nanoparticles and Ag nanoclusters. The bigger Ag nanoclusters (55-100 nm) can be seen decorated evenly alongside the smaller Ag nanoparticles on the PPy film. As for the Ag@PPy/CS nanocomposite electrode, both Ag nanoparticles and Ag nanoclusters can be observed as well. However, the Ag nanoclusters appeared to be smaller in size, with their particle size in the range of 30-80 nm, as shown in **Figure 7.3d**. As mentioned in our previous studies, the Ag nanoparticles were already formed in the deposition solution during the

redox reaction between pyrrole and Ag^+ ions. The oxidation of the pyrrole during electrodeposition at the electrode surface continues to supply electrons to reduce the remaining Ag^+ ions to Ag nanoclusters. The significantly higher rate of reduction of Ag^+ during electrodeposition gave rise to the bigger particle size of Ag nanoclusters. The base morphology of Ag@PPy/CS is also similar to that of PPy/CS where bulbous-like spheres can be seen projecting out of the surface. In **Figure 7.3e**, the areas of bright contrast on the element maps correlate with the C, N, O and Ag signal maps.

University of Malaya

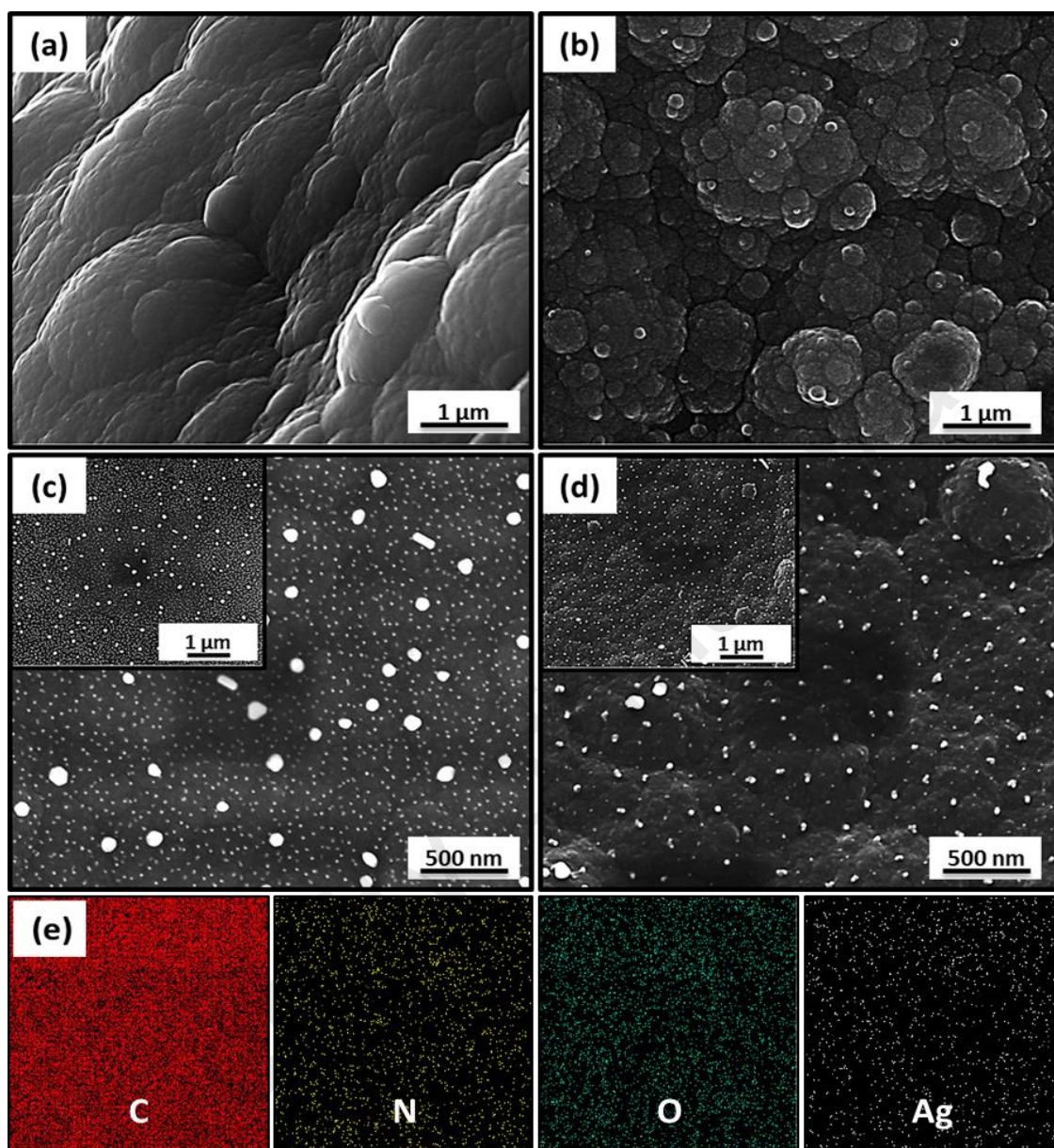


Figure 7.3: FESEM images of (a) PPy, (b) PPy/CS, (c) Ag@PPy, (d) Ag@PPy/CS nanocomposite electrodes, and (e) elemental mapping of the Ag@PPy/CS nanocomposite electrode. Insets of (c) and (d) show the lower magnification images of the respective nanocomposites.

The structure of the Ag@PPy and Ag@PPy/CS nanocomposite electrodes was characterized by HRTEM and shown in **Figure 7.4**. The Ag nanoclusters in both nanocomposite electrodes can be seen in **Figure 7.4a** and **7.4c**. An obvious reduction in the size of Ag nanoclusters was observed in Ag@PPy/CS due to the addition of CS. Similarly, the ultra-small Ag nanoparticles also showed decrease in size when CS is present in the nanocomposite. The Ag nanoparticles from Ag@PPy displayed a size range of 2 – 4 nm (**Figure 7.4b**) whilst the Ag nanoparticles from Ag@PPy/CS displayed an even smaller size range of 1 – 2 nm as seen in **Figure 7.4d**. It was found that the addition of CS caused an apparent decrease in the particle sizes of both Ag nanoclusters and Ag nanoparticles. Ag⁺ ions readily form coordinate bonds with the lone pair electrons from the amine groups of PPy. When CS is added, more coordinate bonds can be formed with the Ag⁺ ions due to the presence hydroxyl groups in the CS, providing more sites for the reduction of Ag⁺ ions. Furthermore, the long polymer chains of CS retarded the growth of metallic Ag sterically by protecting the particles from agglomeration and slowing the particle growth, facilitating the particle size reduction of Ag (Cruz-Silva et al., 2007; Sun et al., 2012).

The schematic representation for the one-step electrodeposition of Ag@PPy/CS nanocomposite is illustrated in **Figure 7.5**. Color change can be observed in the reaction vessel during the preparation of the deposition solution indicating the initial formation of Ag particles and oligomers of pyrrole.

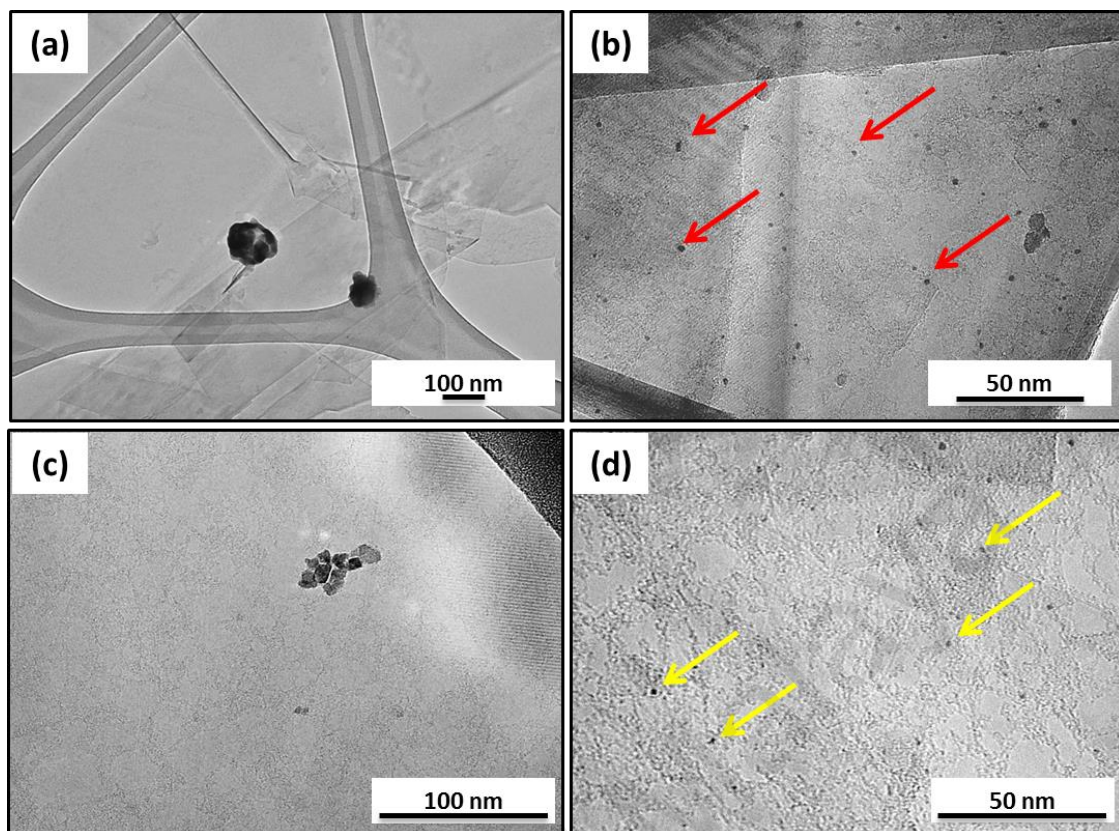


Figure 7.4: HRTEM images of (a) Ag nanoclusters, (b) Ag nanoparticles from Ag@PPy and (c) Ag nanoclusters and (d) Ag nanoparticles from Ag@PPy/CS.

University of

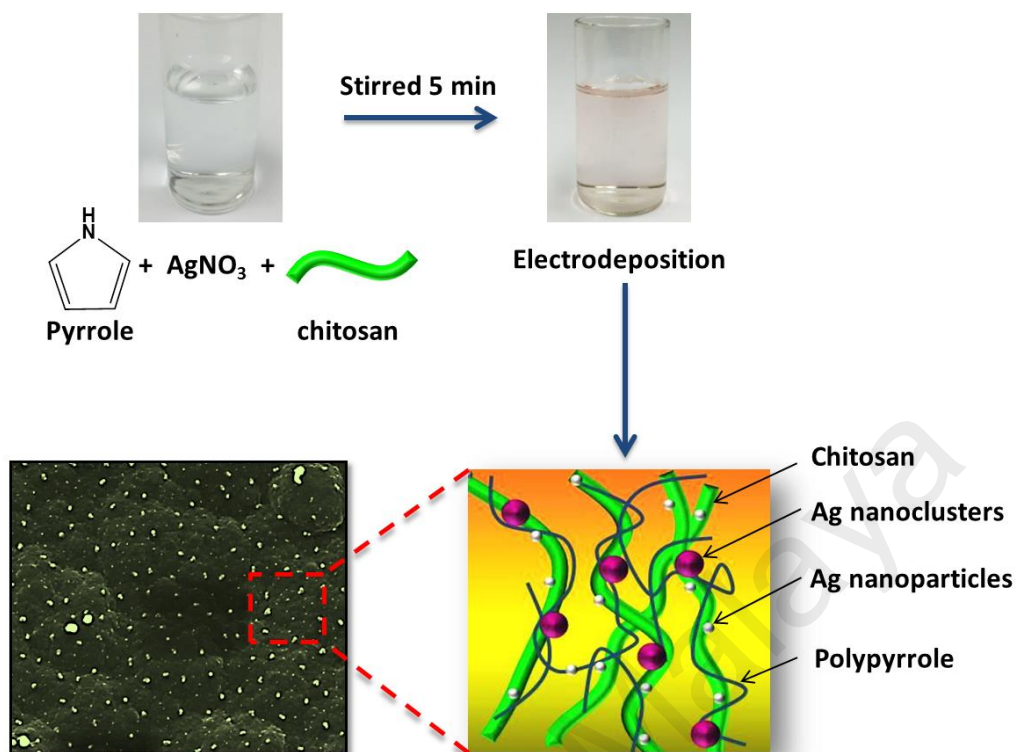


Figure 7.5: Schematic representation for the formation of Ag@PPy/CS nanocomposite via one-step electrodeposition.

7.2.5 Surface wettability studies

The wettability of a solid with water depends on the interfacial tensions between water/air, water/solid and solid/air. The wettability of the electrode by aqueous electrolyte plays an important role on the specific capacitance of the electrode because a hydrophilic electrode will allow better electrolyte infiltration throughout the internal volume of the material. The wetting results are showed in **Figure 7.6**. A contact angle of 180° means complete non-wetting, on the other hand, a contact angle of 0° corresponds to complete wetting. The water contact angles of PPy and Ag@PPy were measured to be 85.1° and 85.2°, respectively. Both electrodes having similar contact angle implies that the embedded Ag nanoparticles and Ag nanoclusters on the PPy

surface did not affect the hydrophilicity of the PPy. In addition, their contact angles were less than less than 90° , indicating that PPy is an intrinsically hydrophilic material, as the amine groups on PPy readily form hydrogen bonds with water (Du et al., 2013). The hydrophilicity of the CS nanocomposite electrodes were improved tremendously due to the extensive formation of hydrogen bonds with the hydroxyl and amine groups of CS. Hence, PPy/CS and Ag@PPy/CS displayed contact angles of 41.8° and 43.3° , respectively. This revealed that the hydrophilicity of the electrodes was enhanced by the addition of CS. The slight increment of the contact angle in Ag@PPy/CS could be due to the blocking of the larger Ag nanoclusters on the surface of the PPy/CS films.

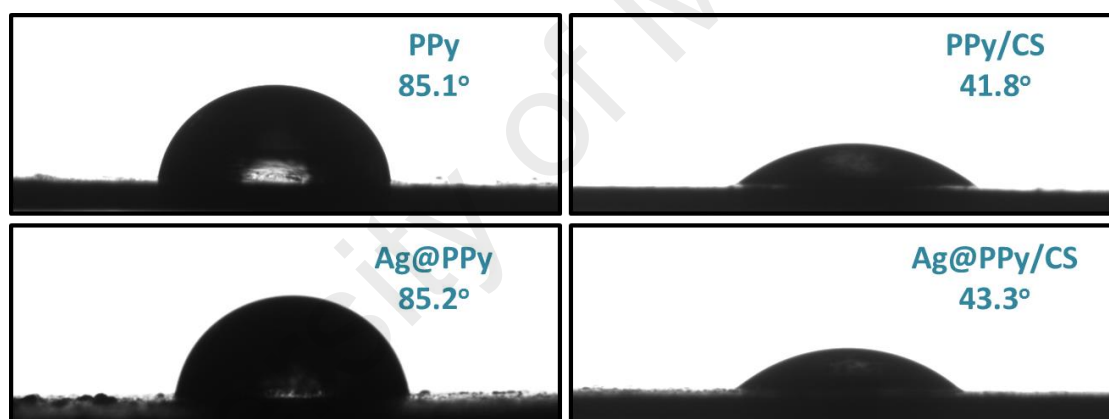


Figure 7.6: Digital images of water droplets on the surfaces of the as-prepared electrodes.

7.2.6 Electrochemical characterization

CV and GCD tests were performed to evaluate the electrochemical performances of the electrodes in a three-electrode system. The CV curves of the electrodes were shown in **Figure 7.7a** at a scan rate of 10 mV s^{-1} , with $1 \text{ M H}_2\text{SO}_4$ as the electrolyte. Clearly, all the nanocomposite electrodes exhibited higher peak current than that of PPy.

Two pairs of redox peaks can be observed when Ag nanoparticles and Ag nanoclusters are present in the nanocomposites. It has been reported that the electrochemical redox behavior and the peak separation are dependent on the size of Ag particles (Chaki et al., 2004; Ivanova & Zamborini, 2010). The Ag nanoparticles and Ag nanoclusters in the nanocomposite electrodes can be distinguished easily from their redox peak. The anodic and cathodic peaks of Ag nanoparticles in both nanocomposite electrodes are 0.19 and 0.01 V, respectively, having a peak separation of 0.18 V. Their redox peak potentials are the same due to them having very close size ranges. The Ag nanoclusters in the ternary nanocomposite Ag@PPy/CS displayed the anodic and cathodic peaks at 0.44 and 0.21, respectively, with a peak separation of 0.23 V. On the other hand, the Ag nanoclusters in the binary nanocomposite Ag@PPy displayed a pair of redox peaks located at 0.50 and 0.20, owing to the anodic and cathodic peak of Ag, with a peak separation of 0.30 V. As the size of Ag increase, it is observed that the peak separation between the anodic and cathodic peaks increases. This is due to the decrease in the electron transfer with an increase in the size (Chaki et al., 2004). The CV results signify the presence of hybrid Ag nanoparticles and Ag nanoclusters in the Ag@PPy and Ag@PPy/CS nanocomposites. **Table 7.1** summarizes detailed analysis of the electrochemical parameters such as anodic and cathodic peak potentials, peak separation obtained from the cyclic voltammograms at 10 mV s^{-1} scan rate, along with the size range of Ag particles.

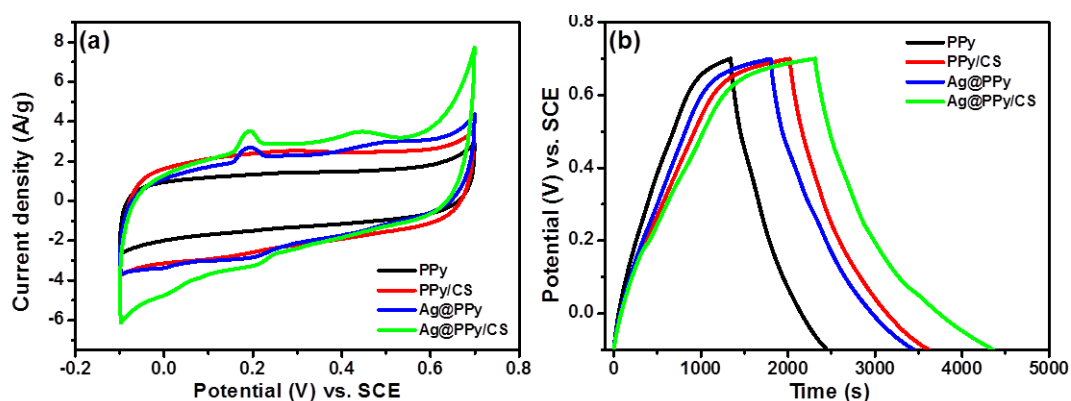


Figure 7.7: (a) CV curves at 10 mV s^{-1} and (b) GCD curves at 0.2 A g^{-1} of the as-synthesized electrodes.

Table 7.1: Electrochemical data for Ag@PPy and Ag@PPy/CS nanocomposite electrodes.

Electrode	Types of Ag particles	Size range (nm)	Anodic peak E_a (V)	Cathodic peak E_c (V)	Peak separation ΔE (V)
Ag@PPy	Ag nanoparticles	2 – 4	0.19	0.01	0.18
	Ag nanoclusters	55 – 100	0.50	0.20	0.30
Ag@PPy/CS	Ag nanoparticles	1 – 2	0.19	0.01	0.18
	Ag nanoclusters	30 – 80	0.44	0.21	0.23

The GCD curves of the nanocomposite electrodes were shown in **Figure 7.7b**. Ag@PPy/CS showed the longest discharge time, revealing that it has the highest specific capacitance among the other electrodes. Hence, the specific capacitances calculated from the discharge curve at 0.2 A g^{-1} were 273, 403, 414 and 513 F g^{-1} for PPy, PPy/CS, Ag@PPy and Ag@PPy/CS. The Ag@PPy/CS outperformed the other electrodes due to the synergetic contribution from the Ag particles and CS. The Ag nanoparticles increase the electrical conductivity of the PPy by enhancing the electron hopping along the conjugated PPy chains while the bigger Ag nanoclusters prevent the

PPy/CS films from restacking. Additionally, the CS promotes the electrolyte affinity of the Ag@PPy/CS, resulting in an upsurge of electrolyte penetration into the surface (Yoo et al., 2014). The combined merits of hybrid Ag nanoparticle/nanocluster and CS with PPy led to a high specific capacitance of the ternary nanocomposite.

7.2.7 Supercapacitor device performance

Symmetric supercapacitor devices were assembled from the as-synthesized nanocomposites electrodes in order to completely determine the electrochemical performances and the potentials applications of the materials. The CV curves of the electrodes scanned at 10 mV s^{-1} were shown in **Figure 7.8a**. It can be seen that the area of the CV curves for the binary and ternary nanocomposite electrodes were larger than that of PPy, due to the effective enhancement of the capacitance properties from the addition of Ag and CS, with Ag@PPy/CS showing the largest CV curve. Even at a high scan rate of 200 mV s^{-1} , Ag@PPy/CS still maintains a fairly rectangular cyclic voltammogram, demonstrating ideal capacitive behavior (**Figure 7.8b**). The GCD curves of the symmetric supercapacitors operated at 0.2 A g^{-1} current density were shown in **Figure 7.8c**. The ternary nanocomposite Ag@PPy/CS showed the highest specific capacitance of 183 F g^{-1} followed by Ag@PPy, PPy/CS and PPy with specific capacitances of 161, 146, and 96 F g^{-1} , respectively.

Figure 7.8d displayed the specific capacitance of the symmetric supercapacitors as a function of current density. Ag@PPy/CS still exhibits the highest specific capacitance at all current densities due to its enhanced electrical conductivity and hydrophilicity. The critical aspect of the electrode wettability becomes more evident when comparing between Ag@PPy and PPy/CS. It is interesting to note that, Ag@PPy showed higher specific capacitance than that of PPy/CS at low current densities but its

performance rapidly degrades at higher current densities, rendering it to perform poorer than PPy/CS. Generally, the specific capacitance decreases with increasing current density because of the lower charge mobilization of the electrolyte ions per unit time. A more hydrophilic electrode will allow rapid infiltration of electrolyte ions into the framework of the electrode; hence more capacitance can be retained at high current densities. Therefore, the PPy/CS has higher specific capacitance than Ag@PPy at high current densities.

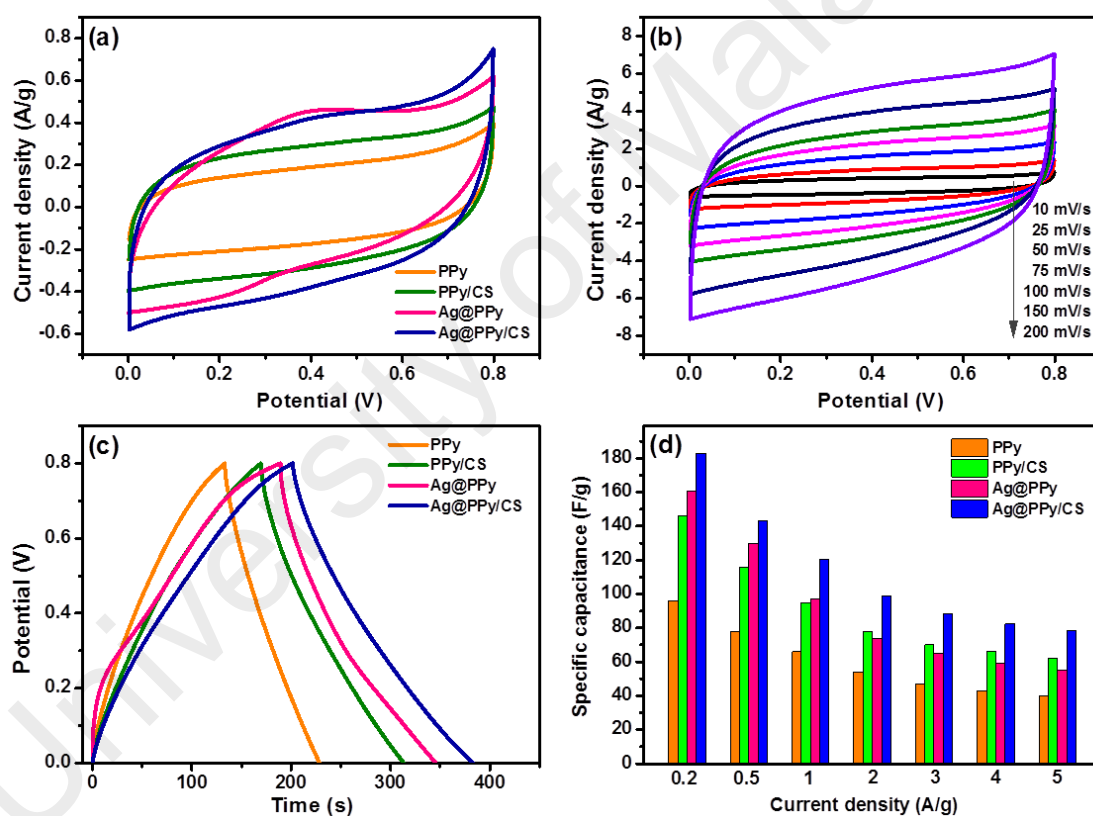


Figure 7.8: (a) CV curves at 10 mV s^{-1} , (b) CV curves of Ag@PPy/CS symmetric supercapacitor at various scan rates, (c) GCD curves at 0.2 A g^{-1} , and (d) comparison of the dependence of specific capacitance on the current density of the symmetric supercapacitors.

Electrochemical impedance spectroscopy (EIS) studies were performed to investigate the influence of Ag and CS on the resistance of the nanocomposite. The Nyquist plots of EIS for the symmetric supercapacitors are shown in **Figure 7.9**. At high frequencies region, the equivalent series resistance (ESR) and charge transfer resistance (R_{ct}) can be obtained from the intercept at the real axis and the diameter of the semicircle, respectively. The ESR represents the contact resistance between the electrolyte, current collector, and active material; the intrinsic resistance of the active material; and the resistance of the electrolyte. The corresponding ESR and R_{ct} values of the symmetric supercapacitors are summarized in **Table 7.2**. The PPy/CS gave the highest R_{ct} of 4.08 Ω due to the addition of the non-conducting CS into the nanocomposite (Yin et al., 2010). Nonetheless, the increased resistance of the PPy/CS electrode was compensated for its enhanced hydrophilicity, exhibiting higher specific capacitance value than the pure PPy electrode. The electrical conductivity was successfully restored upon the embedment of hybrid Ag nanoparticle/nanocluster into the Ag@PPy/CS nanocomposite electrode. As a result, the R_{ct} value of Ag@PPy/CS was evidently reduced to 0.89 Ω which is close to that of Ag@PPy (0.82 Ω).

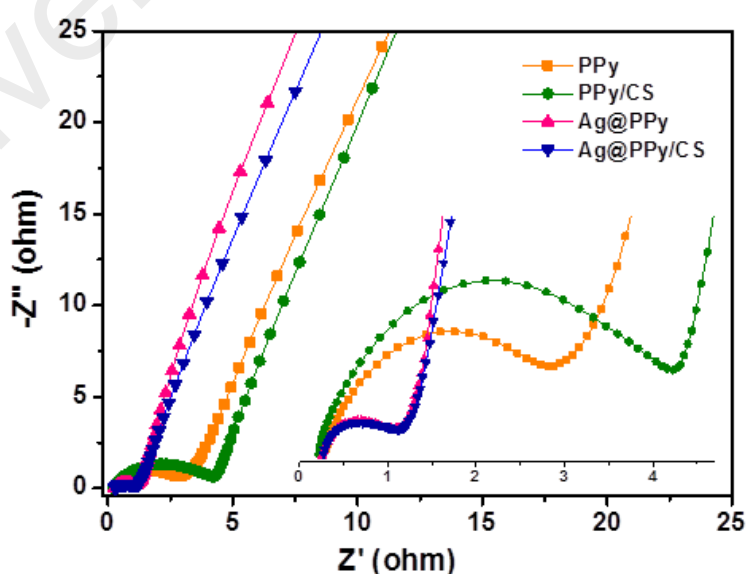


Figure 7.9: Nyquist plots of EIS for the as-fabricated symmetric supercapacitors.

Table 7.2: The ESR and R_{ct} values of the symmetric supercapacitors obtained from the Nyquist plots.

Electrodes	ESR (Ω)	R_{ct} (Ω)
PPy	0.30	2.90
PPy/CS	0.22	4.08
Ag@PPy	0.26	0.82
Ag@PPy/CS	0.28	0.89

The Ragone plots of the symmetric supercapacitors calculated from the GCD curves are shown in **Figure 7.10a**. The Ag@PPy/CS nanocomposite electrode had an energy density of 16.3 W h kg^{-1} at a power density of 322 W kg^{-1} . The power density can be improved to 8707 W kg^{-1} at an energy density of 7.0 W h kg^{-1} . The energy and power density of the Ag@PPy/CS nanocomposite electrode was superior to Ag@PPy, PPy/CS and PPy, proving the active involvement of the hybrid Ag nanoparticle/nanocluster and CS in improving the electrochemical properties of the PPy.

The cycling stability of the electrodes was accessed over 1000 charge/discharge cycle at 0.5 A g^{-1} and are shown in **Figure 7.10b**. The Ag@PPy/CS and Ag@PPy revealed good capacitance retention, retaining up to 98.3% and 98.9%, respectively. The rapid increment of the specific capacitance in the first 100 cycles of the PPy/CS is believed to be caused by the good water absorbency of CS (Huang et al., 2013), but still able to retained up to 94.0% of its initial capacitance. PPy only retained 88.8% capacitance due to its excessive swelling and shrinking of the polymer chains during the charge/discharge process (Zhang et al., 2009). The improved cycling stability of the binary and ternary nanocomposites revealed that the electrochemical stability of PPy has been enhanced.

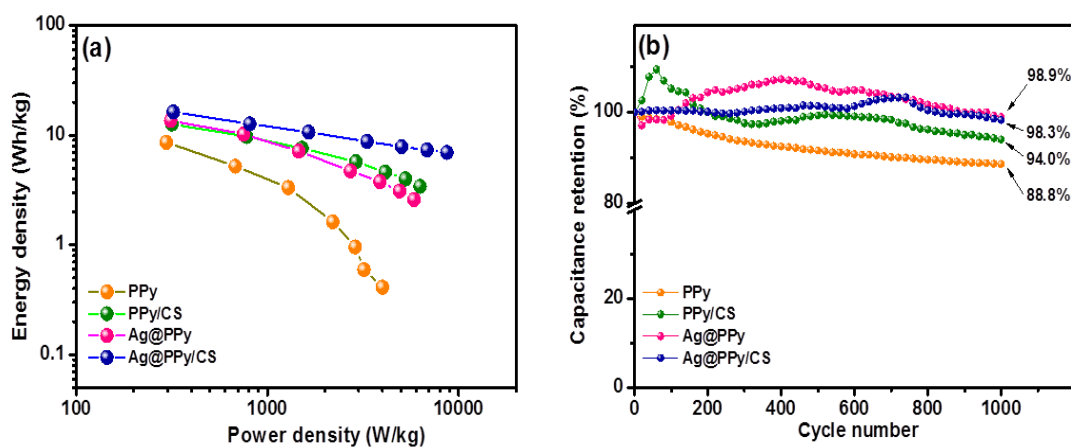


Figure 7.10: (a) Ragone plots, and (b) cycling stability plots for the symmetric supercapacitors.

7.3 Conclusion

In this study, we demonstrate a facile one-step electrodeposition to produce a Ag@PPy/CS nanocomposite. The results show that Ag@PPy/CS nanocomposite electrode is beneficial for the transportation of both electrolyte ions and electrons, leading to high electrochemical performance. Firstly, the increased accessibility of electrolyte ions is due to the enhanced hydrophilicity contributed by CS. Secondly, the coordination of CS with Ag stabilized the growth of metallic Ag, reducing the particle size of the hybrid Ag nanoparticle/nanocluster. Thirdly, the evenly distributed ultra-small Ag nanoparticles (1-2 nm) enhanced the electron hopping system of the conjugated PPy. Finally, the larger Ag nanoclusters in the size range of 30-80 nm acted as spacers, preventing the restacking of PPy/CS films besides improving the electrical conductivity of the nanocomposite. The elegant synergy between CS and Ag boosted the supercapacitive properties of PPy making it a promising candidate for application as electrode for high-performance supercapacitors.

CHAPTER 8

CONCLUSION AND FUTURE WORK RECOMMENDATIONS

8.1 Conclusion

The aim of this research was to develop PPy-based nanocomposites, which was intended to harness the unique physical and electrochemical benefits of PPy. The synthesis and electrochemical characterization of four different PPy-based nanocomposites were presented in this work.

Firstly, the PPy was paired up with another class of pseudocapacitor, MnO₂. The facile mixing of KMnO₄ and pyrrole gave rise to PPy/MnO₂ nanocomposite. Various morphologies were synthesized by varying the pH value of the reaction mixture. When the solution pH increased from 1.0 to 7.8, the morphologies of the PPy/MnO₂ nanocomposite changed from a compact sheet-like structure to a highly porous structure and finally to a granular structure. The porous morphology obtained at pH 4.0 showed the highest specific surface area of 230 m² g⁻¹ thereby displayed the highest specific capacitance of 306 F g⁻¹ compared to the other PPy/MnO₂ prepared at different pH values.

PPy/CS was the second nanocomposite explored in this work. Even though CS is a non-conductive material as observed from the increased R_{ct} in the EIS data, however, it offered excellent hydrophilic nature to the PPy/CS. The good electrode wettability of the PPy/CS nanocomposite electrode encouraged better electrolyte infiltration into the electrode. This enhanced hydrophilic property compensated the increased resistivity of the PPy/CS. Therefore, the specific capacitance was improved accordingly from 273 to 403 F g⁻¹ for PPy to PPy/CS, respectively.

The third part of this work featured a hybrid Ag nanoparticle/nanocluster decorated on PPy. The unique hybrid Ag nanoparticle/nanocluster was optimized at 0.05 M AgNO₃. Incorporation of metallic Ag undoubtedly improved the electrochemical properties of PPy due to the highly conductive Ag nanoparticles and Ag nanoclusters. Moreover, the larger Ag nanoclusters suppress the restacking of PPy films, extending the active sites for redox reactions. As a result, the Ag@PPy showed a maximum of specific capacitance of 414 F g⁻¹.

The fourth PPy-based nanocomposite presented in this thesis is Ag@PPy/CS. The combined advantages of both Ag and CS successfully enhanced the electrical conductivity and hydrophilicity of the ternary nanocomposite. Additionally, the presence of the biopolymer chitosan acted as a stabilizer for the growth of Ag particles, producing smaller sizes of Ag nanoparticle/nanocluster in Ag@PPy/CS as compared to Ag@PPy. As a consequence of the improved electron and electrolyte ion transport, the ternary nanocomposite displayed a specific capacitance of 513 F g⁻¹.

The PPy nanocomposite (PPy/MnO₂, PPy/CS, Ag@PPy and Ag@PPy/CS) presented in this thesis was formed by strategically combining electroactive and non-electroactive materials into PPy in order to improve its supercapacitive performance. The evaluation of the physical structure and morphology, in conjunction with electrochemical measurements, revealed that the PPy-based nanocomposite as a novel and promising class of electrode materials for high-performance supercapacitors.

8.2 Future work recommendations

Supercapacitors are still needed to address the critical performance gap between batteries and conventional capacitors. Designing high-performance supercapacitors with high specific capacitance, high energy density and good cycling stability are required due to the rapidly growing demands on energy storage devices. This thesis is finalized with recommendations for further research works based on this research.

In this research, the aqueous electrolytes Na_2SO_4 and H_2SO_4 were used for the electrochemical characterization of the as-prepared nanocomposite electrodes. However, the operating voltage of aqueous electrolytes is often limited by the decomposition potential of water which is at 1.23 V. This limits their practical employment in supercapacitor applications as energy density is largely dependent on the operating charge discharge of the supercapacitor. Hence, organic and ionic liquid electrolyte can be used to replace the current aqueous electrolyte. The higher decomposition potential of organic electrolytes allow the operating voltage to go above 2 V and even up to 3 V for ionic liquid as mentioned in the literature review section in this thesis. Employing these electrolytes can dramatically boost the energy density of the PPy-based nanocomposite electrodes.

Another way of widening the operating voltage of the supercapacitor electrode is by fabricating asymmetric supercapacitors. Therefore, researches on asymmetric supercapacitors are recommended. Normally carbon-based electrodes are employed as the negative electrode whereas pseudocapacitors are used as the positive electrode because of their complementary working potential windows. In asymmetric supercapacitors, the pseudocapacitors electrode can reach for a higher voltage, while the minimum potential of the carbon-based electrode is extended towards more negative

potential values. This allows the cell voltages to reach up to 2 V or more, significantly improving the energy density (Demarconnay et al., 2011; Gao et al., 2012).

Finally, as CS and Ag are neither EDLC nor pseudocapacitors, their incorporation of Ag and CS into PPy presented in chapter 5, 6 and 7 can pave the way for designing new hybrid supercapacitor electrodes with desirable properties. The results reported in this thesis may provide useful information for further researches into the employment of non-electroactive materials with common electroactive materials.

University of Malaysia

REFERENCES

- Abulizi, A., Yang, G. H., Okitsu, K., & Zhu, J.-J. (2014). Synthesis of MnO₂ nanoparticles from sonochemical reduction of MnO₄⁻ in water under different pH conditions. *Ultrasonics Sonochemistry*, 21: 1629–1634.
- Akmaz, S., Adıgüzel, E. D., Yasar, M., & Erguven, O. (2013). The effect of Ag content of the chitosan-silver nanoparticle composite material on the structure and antibacterial activity. *Advances in Materials Science and Engineering*, 2013: 12–18.
- Allen, M. J., Tung, V. C., & Kaner, R. B. (2010). Honeycomb carbon: a review of graphene. *Chemical Reviews*, 110: 132–145.
- Amarnath, C. A., Hong, C. E., Kim, N. H., Ku, B.-C., Kuila, T., & Lee, J. H. (2011). Efficient synthesis of graphene sheets using pyrrole as a reducing agent. *Carbon*, 49: 3497–3502.
- An, H., Wang, Y., Wang, X. X., Zheng, L., Wang, X. X., Yi, L., Bai, L., & Zhang, X. (2010). Polypyrrole/carbon aerogel composite materials for supercapacitor. *Journal of Power Sources*, 195: 6964–6969.
- Andreas, H. A., & Conway, B. E. (2006). Examination of the double-layer capacitance of an high specific-area C-cloth electrode as titrated from acidic to alkaline pHs. *Electrochimica Acta*, 51: 6510–6520.
- Ansari, R. (2006). Polypyrrole Conducting Electroactive Polymers: Synthesis and Stability Studies. *E-Journal of Chemistry*, 3: 186–201.
- Ayad, M., Salahuddin, N., Fayed, A., Bastakoti, B. P., Suzuki, N., & Yamauchi, Y. (2014). Chemical design of a smart chitosan–polypyrrole–magnetite nanocomposite toward efficient water treatment. *Phys. Chem. Chem. Phys.*, 16: 21812–21819.
- Babu, K. F., Dhandapani, P., Maruthamuthu, S., & Kulandainathan, M. A. (2012). One pot synthesis of polypyrrole silver nanocomposite on cotton fabrics for multifunctional property. *Carbohydrate Polymers*, 90: 1557–1563.
- Bahloul, A., Nessark, B., Briot, E., Groult, H., Mauger, A., Zaghbi, K., & Julien, C. M. (2013). Polypyrrole-covered MnO₂ as electrode material for supercapacitor. *Journal of Power Sources*, 240: 267–272.
- Baños, R., Manzano-Agugliaro, F., Montoya, F. G., Gil, C., Alcayde, a., & Gómez, J. (2011). Optimization methods applied to renewable and sustainable energy: A review. *Renewable and Sustainable Energy Reviews*, 15: 1753–1766.
- Becker, H.I 1957 Patent US280616 (1957). Low voltage electrolytic capacitor.

- Biswas, S., & Drzal, L. T. (2010). Multilayered nanoarchitecture of graphene nanosheets and polypyrrole nanowires for high performance supercapacitor electrodes. *Chemistry of Materials*, 5667–5671.
- Bordjiba, T., Mohamedi, M., & Dao, L. H. (2008). New class of carbon-nanotube aerogel electrodes for electrochemical power sources. *Advanced Materials*, 20: 815–819.
- Brousse, T., Bélanger, D., & Long, J. W. (2015). To be or not to be pseudocapacitive? *Journal of the Electrochemical Society*, 162: A5185–A5189.
- Burke, A. (2000). Ultracapacitors: Why, how, and where is the technology. *Journal of Power Sources*, 91: 37–50.
- Burke, A. (2007). R&D considerations for the performance and application of electrochemical capacitors. *Electrochimica Acta*, 53: 1083–1091.
- Calvo, E. G., Lufrano, F., Staiti, P., Brigandì, A., Arenillas, A., & Menéndez, J. A. (2013). Optimizing the electrochemical performance of aqueous symmetric supercapacitors based on an activated carbon xerogel. *Journal of Power Sources*, 241: 776–782.
- Cao, J., Wang, Y., Chen, J., Li, X., Walsh, F. C., Ouyang, J., Jia, D., & Zhou, Y. (2015). Three-dimensional graphene oxide/polypyrrole composite electrodes fabricated by one-step electrodeposition for high performance supercapacitors. *Journal of Materials Chemistry A*, 3: 14445–14457.
- Chaki, N. K., Sharma, J., Mandle, A. B., Mulla, I. S., Pasricha, R., Vijayamohan, K., & Division, P. C. (2004). Size dependent redox behavior of monolayer protected silver nanoparticles (2–7 nm) in aqueous medium. *Physical Chemistry Chemical Physics : PCCP*, 6: 1304–1309.
- Chang, H., & Wu, H. (2013). Graphene-based nanocomposites: preparation, functionalization, and energy and environmental application. *Energy & Environmental Science*, 6: 3483–3507.
- Chang, J.-K., Lee, M.-T., Huang, C.-H., & Tsai, W.-T. (2008). Physicochemical properties and electrochemical behavior of binary manganese–cobalt oxide electrodes for supercapacitor applications. *Materials Chemistry and Physics*, 108: 124–131.
- Chen, W., Fan, Z., Gu, L., Bao, X., & Wang, C. (2010). Enhanced capacitance of manganese oxide via confinement inside carbon nanotubes. *Chemical Communications*, 46: 3905–3907.
- Cheng, Q., Tang, J., Ma, J., Zhang, H., Shinya, N., & Qin, L.-C. (2011). Graphene and nanostructured MnO₂ composite electrodes for supercapacitors. *Carbon*, 49: 2917–2925.

- Cheng, S., Yang, L., Liu, Y., Lin, W., Huang, L., Chen, D., Wong, C. P., & Liu, M. (2013). Carbon fiber paper supported hybrid nanonet/nanoflower nickel oxide electrodes for high-performance pseudo-capacitors. *Journal of Materials Chemistry A*, 1: 7709–7716.
- Cheng, Y., Mierlo, J. Van, Bosschet, P. Van Den, & Lataire, P. (2006). Using super capacitor based energy storage to improve power quality in distributed power generation. *Power Electronics and Motion Control Conference, EPE-PEMC*, 537 – 543.
- Cherusseri, J., & Kar, K. K. (2015). Self-standing carbon nanotube forest electrodes for flexible supercapacitors. *RSC Advances*, 5: 34335–34341.
- Conway, B. E., Birss, V., & Wojtowicz, J. (1997). The role and utilization of pseudocapacitance for energy storage by supercapacitors. *Journal of Power Sources*, 66: 1–14.
- Conway, B.E. (1999). *Electrochemical supercapacitors: Scientific fundamentals and technological applications*. New York, Kluwer Academic/Plenum Press.
- Cruz-Silva, R., Escamilla, A., Nicho, M. E., Padron, G., Ledezma-Perez, A., Arias-Marin, E., Moggio, I., & Romero-Garcia, J. (2007). Enzymatic synthesis of pH-responsive polyaniline colloids by using chitosan as steric stabilizer. *European Polymer Journal*, 43: 3471–3479.
- Cuentas-Gallegos, A. K., & Gómez-Romero, P. (2005). In-situ synthesis of polypyrrole-MnO_{2-x} nanocomposite hybrids. *Journal of New Materials for Electrochemical Systems*, 188: 181–188.
- Dai, Y., Li, J., Yan, G., Xu, G., Xue, Q., & Kang, F. (2015). Preparation of the cactus-like porous manganese oxide assisted with surfactant sodium dodecyl sulfate for supercapacitors. *Journal of Alloys and Compounds*, 621: 86–92.
- Dai, Y. M., Tang, S. C., Ba, Z. X., Zhu, S. S., Wang, Q., Wang, C., & Meng, X. K. (2014). Coating MnO₂ nanowires by silver nanoparticles for an improvement of capacitance performance. *Materials Letters*, 117: 104–107.
- Davies, A., Audette, P., Farrow, B., Hassan, F., Chen, Z., Choi, J.-Y., & Yu, A. (2011). Graphene-based flexible supercapacitors: pulse-electropolymerization of polypyrrole on free-standing graphene films. *The Journal of Physical Chemistry C*, 115: 17612–17620.
- Demarconnay, L., Raymundo-Piñero, E., & Béguin, F. (2011). Adjustment of electrodes potential window in an asymmetric carbon/MnO₂ supercapacitor. *Journal of Power Sources*, 196: 580–586.
- Dhibar, S., & Das, C. K. (2014). Silver nanoparticles decorated polyaniline/multiwalled carbon nanotubes nanocomposite for high-performance supercapacitor electrode. *Industrial & Engineering Chemistry Research*, 53: 3495–3508.
- Donald, L.B. 1970 US3536963 (1970). Electrolytic capacitor having carbon paste electrodes.

- Douglas, H., & Pillay, P. (2005). Sizing ultracapacitors for hybrid electric vehicles. *Industrial Electronics Society, 2005. IECON 2005. 31st Annual Conference of IEEE*, 6.
- Du, X., Hao, X., Wang, Z., Ma, X., Guan, G., Abuliti, A., Ma, G., & Liu, S. (2013). Highly stable polypyrrole film prepared by unipolar pulse electro-polymerization method as electrode for electrochemical supercapacitor. *Synthetic Metals*, 175: 138–145.
- Dubal, D. P., Lee, S. H., Kim, J. G., Kim, W. B., & Lokhande, C. D. (2012). Porous polypyrrole clusters prepared by electropolymerization for a high performance supercapacitor. *Journal of Materials Chemistry*, 22: 3044–3052.
- Dubal, D. P., Patil, S. V., Gund, G. S. S., & Lokhande, C. D. (2013). Polyaniline–polypyrrole nanograined composite via electrostatic adsorption for high performance electrochemical supercapacitors. *Journal of Alloys and Compounds*, 552: 240–247.
- Dubal, D. P., Patil, S. V., Kim, W. B., & Lokhande, C. D. (2011). Supercapacitors based on electrochemically deposited polypyrrole nanobricks. *Materials Letters*, 65: 2628–2631.
- Energy Information Administration, 2013. Accessed on 5/10/2015, <http://www.eia.gov/todayinenergy/detail.cfm?id=12251>
- Erdenedelger, G., Lee, T., Dao, T. D., Kim, J. S., Kim, B.-S., & Jeong, H. M. (2014). Solid-state functionalization of graphene with amino acids toward water-dispersity: implications on a composite with polyaniline and its characteristics as a supercapacitor electrode material. *Journal of Materials Chemistry A*, 2: 12526–12534.
- Fang, L., Liyan, Z., & Tao, X. (2015). Synthesis and performance study of nano-Ag particles-chitosan-graphene composites synthesis and performance study of nano-Ag. *Integrated Ferroelectrics*, 160: 10–17.
- Fic, K., Lota, G., Meller, M., & Frackowiak, E. (2012). Novel insight into neutral medium as electrolyte for high-voltage supercapacitors. *Energy & Environmental Science*, 5: 5842–5850.
- Frackowiak, E. (2007). Carbon materials for supercapacitor application. *Physical Chemistry Chemical Physics : PCCP*, 9: 1774–1785.
- Frackowiak, E., Khomenko, V., Jurewicz, K., Lota, K., & Béguin, F. (2006). Supercapacitors based on conducting polymers/nanotubes composites. *Journal of Power Sources*, 153: 413–418.
- Fusco, S., Chatzipirpiridis, G., Sivaraman, K. M., Ergeneman, O., Nelson, B. J., & Pané, S. (2013). Chitosan electrodeposition for microrobotic drug delivery. *Advanced Healthcare Materials*, 2: 1037–1044.

- Gan, J. K., Lim, Y. S., Huang, N. M., & Lim, H. N. (2015). Hybrid silver nanoparticle/nanocluster-decorated polypyrrole for high-performance supercapacitors. *RSC Adv.*, 5: 75442–75450.
- Gao, H., Xiao, F., Ching, C. B., & Duan, H. (2012). Flexible all-solid-state asymmetric supercapacitors based on free-standing carbon nanotube/graphene and Mn_3O_4 nanoparticle/graphene paper electrodes. *ACS Applied Materials & Interfaces*, 4: 7020–7026.
- García-Fernández, M. J., Buitrago-Sierra, R., Pastor-blas, M. M., Soares, O. S. G. P., Pereira, M. F. R., & Sepúlveda-Escribano, A. (2015). Green synthesis of polypyrrole-supported metal catalysts: application to nitrate removal in water. *RSC Advances*, 5: 32706–32713.
- Ge, J., Yao, H.-B., Hu, W., Yu, X.-F., Yan, Y.-X., Mao, L.-B., Li, H.-H., Li, S.-S., & Yu, S.-H. (2013). Facile dip coating processed graphene/ MnO_2 nanostructured sponges as high performance supercapacitor electrodes. *Nano Energy*, 2: 505–513.
- Geim, A. K., & Novoselov, K. S. (2007). The rise of graphene. *Nature Materials*, 6: 183–191.
- Ghosh, A., Ra, E. J., Jin, M., Jeong, H.-K., Kim, T. H., Biswas, C., & Lee, Y. H. (2011). High Pseudocapacitance from Ultrathin V_2O_5 Films Electrodeposited on Self-Standing Carbon-Nanofiber Paper. *Advanced Functional Materials*, 21: 2541–2547.
- Goodenough, J., Abruña, H., & Buchanan, M. (2007). Basic research needs For electrical energy storage: Report of basic energy sciences workshop on energy storage. *Office of Basic Energy Sciences, DOE*. Retrieved from http://www.sc.doe.gov/bes/reports/files/EES_rpt.pdf
- Gu, Z., Li, C., Wang, G., Zhang, L., Li, X., Wang, W., & Jin, S. (2010). Synthesis and characterization of polypyrrole/graphite oxide composite by in situ emulsion polymerization. *Journal of Polymer Science Part B: Polymer Physics*, 48: 1329–1335.
- Guo, Y., Sun, X., Liu, Y., Wang, W., Qiu, H., & Gao, J. (2012). One pot preparation of reduced graphene oxide (RGO) or Au (Ag) nanoparticle-RGO hybrids using chitosan as a reducing and stabilizing agent and their use in methanol electrooxidation. *Carbon*, 50: 2513–2523.
- Hao, P., Zhao, Z., Leng, Y., Tian, J., Sang, Y., Boughton, R. I., Wong, C. P., Liu, H., & Yang, B. (2015). Graphene-based nitrogen self-doped hierarchical porous carbon aerogels derived from chitosan for high performance supercapacitors. *Nano Energy*, 15: 9–23.
- Hassan, S., Suzuki, M., & El-moneim, A. A. (2014). Synthesis of MnO_2 -chitosan nanocomposite by one-step electrodeposition for electrochemical energy storage application. *Journal of Power Sources*, 246: 68–73.
- Hepowit, L. R., Kim, K. M., Kim, S. H., Ryu, K. S., Lee, Y. M., & Ko, J. M. (2012). Supercapacitive properties of electrodeposited polypyrrole on acrylonitrile-butadiene rubber as a flexible current collector. *Polymer Bulletin*, 69: 873–880.

- Hnida, K. E., Socha, R. P., & Sulka, G. D. (2013). Polypyrrole–silver composite nanowire arrays by cathodic co-deposition and their electrochemical properties. *The Journal of Physical Chemistry C*.
- Hu, C.-C., Chen, W.-C., & Chang, K.-H. (2004). How to Achieve Maximum Utilization of Hydrous Ruthenium Oxide for Supercapacitors. *Journal of The Electrochemical Society*.
- Hu, C.-C., Liu, M.-J., & Chang, K.-H. (2007). Anodic deposition of hydrous ruthenium oxide for supercapacitors. *Journal of Power Sources*, 163: 1126–1131.
- Huang, H., Wu, J., Lin, X., Li, L., Shang, S., Yuen, M. C., & Yan, G. (2013). Self-assembly of polypyrrole/chitosan composite hydrogels. *Carbohydrate Polymers*, 95: 72–76.
- Huang, Z.-D., Zhang, B., Oh, S., Zheng, Q., Lin, X., Yousefi, N., & Kim, J.-K. (2012). Self-assembled reduced graphene oxide/carbon nanotube thin films as electrodes for supercapacitors. *Journal of Materials Chemistry*, 22: 3591–3599.
- Huo, Y.-Q., Zhang, S.-B., & Zhang, H.-Y. (2014). Capacitive performance of polyaniline/manganese dioxide nanofiber microsphere. *Journal of Applied Polymer Science*, 131: 40575.
- Inagaki, M., Konno, H., & Tanaike, O. (2010). Carbon materials for electrochemical capacitors. *Journal of Power Sources*, 195: 7880–7903.
- Ivanova, O. S., & Zamborini, F. P. (2010). Size-dependent electrochemical oxidation of silver nanoparticles. *Journal of the American Chemical Society*, 132: 70–72.
- Izrini, N., Rameshkumar, P., Pandikumar, A., Ikhsan, N. I., Rameshkumar, P., Pandikumar, A., Shahid, M. M., Huang, N. M., Kumar, S. V., Lim, H. N., Izrini, N., Rameshkumar, P., & Pandikumar, A. (2015). Facile synthesis of graphene oxide-silver nanocomposite and its modified electrode for enhanced electrochemical detection of nitrite ions. *Talanta*, 144: 908–914.
- Jagadale, A. D., Kumbhar, V. S., Bulakhe, R. N., & Lokhande, C. D. (2014). Influence of electrodeposition modes on the supercapacitive performance of Co_3O_4 electrodes. *Energy*, 64: 234–241.
- Ji, Z.-H., Dong, B., Liu, Y.-Q., & Liu, C.-G. (2012). The effect of pH and anions on the anisotropic growth of MnO_2 . *Materials Research Bulletin*, 47: 3377–3382.
- Ju, Y.-W., Choi, G., Jung, H.-R., & Lee, W.-J. (2008). Electrochemical properties of electrospun PAN/MWCNT carbon nanofibers electrodes coated with polypyrrole. *Electrochimica Acta*, 53: 5796–5803.
- Keskinen, J., Tuurala, S., Sjödin, M., Kiri, K., Nyholm, L., Flyktman, T., Strømme, M., & Smolander, M. (2015). Asymmetric and symmetric supercapacitors based on polypyrrole and activated carbon electrodes. *Synthetic Metals*, 203: 192–199.

- Khomenko, V., Frackowiak, E., & Béguin, F. (2005). Determination of the specific capacitance of conducting polymer/nanotubes composite electrodes using different cell configurations. *Electrochimica Acta*, 50: 2499–2506.
- Kierzek, K., Frackowiak, E., Lota, G., Gryglewicz, G., & Machnikowski, J. (2004). Electrochemical capacitors based on highly porous carbons prepared by KOH activation. *Electrochimica Acta*, 49: 515–523.
- Kim, B.-H., Kim, C. H., Yang, K. S., Rahy, A., & Yang, D. J. (2012). Electrospun vanadium pentoxide/carbon nanofiber composites for supercapacitor electrodes. *Electrochimica Acta*, 83: 335–340.
- Kim, D.-S. (2004). Activated carbon from peach stones using phosphoric acid activation at medium temperatures. *Journal of Environmental Science and Health, Part A*, 39: 1301–1318.
- Kim, J.-H., Lee, Y.-S., Sharma, A. K., & Liu, C. G. (2006). Polypyrrole/carbon composite electrode for high-power electrochemical capacitors. *Electrochimica Acta*, 52: 1727–1732.
- Koev, S. T., Dykstra, P. H., Luo, X., Rubloff, G. W., Bentley, W. E., Payne, G. F., & Ghodssi, R. (2010). Chitosan: an integrative biomaterial for lab-on-a-chip devices. *Lab on a Chip*, 10: 3026–3042.
- Kumar, G. G., Awan, Z., Nahm, K. S., & Xavier, J. S. (2014). Nanotubular MnO₂/graphene oxide composites for the application of open air-breathing cathode microbial fuel cells. *Biosensors and Bioelectronics*, 53: 528–534.
- Kuperman, A., & Aharon, I. (2011). Battery–ultracapacitor hybrids for pulsed current loads: A review. *Renewable and Sustainable Energy Reviews*, 15: 981–992.
- Lai, J., Levy, S., & Rose, M. F. (1992). High energy density double-layer capacitors for energy storage applications. *Aerospace and Electronic Systems Magazine, IEEE*, 14–19.
- Lee, H. Y., & Goodenough, J. B. (1999). Supercapacitor Behavior with KCl Electrolyte. *Journal of Solid State Chemistry*, 144: 220–223.
- Lee, R.-J., Temmer, R., Tamm, T., Aabloo, A., & Kiefer, R. (2013). Renewable antioxidant properties of suspensible chitosan–polypyrrole composites. *Reactive and Functional Polymers*, 73: 1072–1077.
- Lee, Y.-H., Chang, K.-H., & Hu, C.-C. (2013). Differentiate the pseudocapacitance and double-layer capacitance contributions for nitrogen-doped reduced graphene oxide in acidic and alkaline electrolytes. *Journal of Power Sources*, 227: 300–308.
- Lei, Y., Daffos, B., Taberna, P. L., Simon, P., & Favier, F. (2010). MnO₂-coated Ni nanorods: enhanced high rate behavior in pseudo-capacitive supercapacitor. *Electrochimica Acta*, 55: 7454–7459.

- Li, C., Wang, D., Liang, T., Wang, X., & Ji, L. (2004). A study of activated carbon nanotubes as double-layer capacitors electrode materials. *Materials Letters*, 58: 3774–3777.
- Li, J., Cui, L., & Zhang, X. (2010). Preparation and electrochemistry of one-dimensional nanostructured MnO₂/PPy composite for electrochemical capacitor. *Applied Surface Science*, 256: 4339–4343.
- Li, Q., Liu, J., Zou, J., Chunder, A., Chen, Y., & Zhai, L. (2011). Synthesis and electrochemical performance of multi-walled carbon nanotube/polyaniline/MnO₂ ternary coaxial nanostructures for supercapacitors. *Journal of Power Sources*, 196: 565–572.
- Li, X., & Wei, B. (2012). Facile synthesis and super capacitive behavior of SWNT/MnO₂ hybrid films. *Nano Energy*, 1: 479–487.
- Li, X., & Zhitomirsky, I. (2013). Electrodeposition of polypyrrole-carbon nanotube composites for electrochemical supercapacitors. *Journal of Power Sources*, 221: 49–56.
- Li, Y., Pang, X., Epand, R. F., & Zhitomirsky, I. (2011). Electrodeposition of chitosan-hemoglobin films. *Materials Letters*, 65: 1463–1465.
- Liang, K., Tang, X., & Hu, W. (2012). High-performance three-dimensional nanoporous NiO film as a supercapacitor electrode. *Journal of Materials Chemistry*, 22: 11062–11067.
- Lim, S. P., Pandikumar, A., Huang, N. M., & Lim, H. N. (2014). Enhanced photovoltaic performance of silver@titania plasmonic photoanode in dye-sensitized solar cells. *RSC Advances*, 4: 38111–38118.
- Lim, Y. S., Tan, Y. P., Lim, H. N., Huang, N. M., & Tan, W. T. (2013). Preparation and characterization of polypyrrole/graphene nanocomposite films and their electrochemical performance. *Journal of Polymer Research*, 20: 156.
- Lim, Y. S., Tan, Y. P., Lim, H. N., Huang, N. M., Tan, W. T., Yarmo, M. A., & Yin, C.-Y. (2014). Potentiostatically deposited polypyrrole/graphene decorated nano-manganese oxide ternary film for supercapacitors. *Ceramics International*, 40: 3855–3864.
- Ling, Z., Wang, G., Zhang, M., Fan, X., Yu, C., Yang, J., Xiao, N., & Qiu, J. (2015). Boric acid-mediated B,N-codoped chitosan-derived porous carbons with a high surface area and greatly improved supercapacitor performance. *Nanoscale*, 7: 5120–5125.
- Liu, Y., Peng, X., Ye, H., Xu, J., & Chen, F. (2015). Fabrication and properties of conductive chitosan/polypyrrole composite fibers. *Polymer-Plastics Technology and Engineering*, 54: 411–415.

- Long, C., Jiang, L., Wu, X., Jiang, Y., Yang, D., Wang, C., Wei, T., & Fan, Z. (2015). Facile synthesis of functionalized porous carbon with three-dimensional interconnected pore structure for high volumetric performance supercapacitors. *Carbon*, *93*: 412–420.
- Lozano-Castelló, D., Cazorla-Amorós, D., Linares-Solano, A., Shiraishi, S., Kurihara, H., & Oya, A. (2003). Influence of pore structure and surface chemistry on electric double layer capacitance in non-aqueous electrolyte. *Carbon*, *41*: 1765–1775.
- Lu, X., Wang, G., Zhai, T., Yu, M., Gan, J., Tong, Y., & Li, Y. (2012). Hydrogenated TiO₂ Nanotube Arrays for Supercapacitors. *Nano Letters*, *12*: 1690–1696.
- Luo, X. L., Xu, J. J., Zhang, Q., Yang, G. J., & Chen, H. Y. (2005). Electrochemically deposited chitosan hydrogel for horseradish peroxidase immobilization through gold nanoparticles self-assembly. *Biosensors and Bioelectronics*, *21*: 190–196.
- Lust, E., Jänes, a, & Arulepp, M. (2004). Influence of solvent nature on the electrochemical parameters of electrical double layer capacitors. *Journal of Electroanalytical Chemistry*, *562*: 33–42.
- Maxwell Technologies. Accessed on 20/11/2015, <http://www.maxwell.com/>
- Mazda. Accessed on 20/11/2015, <http://www2.mazda.com/en/technology/env/i-e-loop/>
- Meng, C., Liu, C., & Fan, S. (2009). Flexible carbon nanotube/polyaniline paper-like films and their enhanced electrochemical properties. *Electrochemistry Communications*, *11*: 186–189.
- Mi, J., Wang, X. R., Fan, R. J., Qu, W. H., & Li, W. C. (2012). Coconut-shell-based porous carbons with a tunable micro/mesopore ratio for high-performance supercapacitors. *Energy and Fuels*, *26*: 5321–5329.
- Mison, I. I., Zain, N. K. M., Aziz, R. A., Vidyadharan, B., & Jose, R. (2015). Electrochemical properties of carbon from oil palm kernel shell for high performance supercapacitors. *Electrochimica Acta*, *174*: 78–86.
- Muthulakshmi, B., Kalpana, D., Pitchumani, S., & Renganathan, N. G. (2006). Electrochemical deposition of polypyrrole for symmetric supercapacitors. *Journal of Power Sources*, *158*: 1533–1537.
- Navale, S. T., Mali, V. V., Pawar, S. a., Mane, R. S., Naushad, M., Stadler, F. J., & Patil, V. B. (2015). Electrochemical supercapacitor development based on electrodeposited nickel oxide film. *RSC Adv.*, *5*: 51961–51965.
- Ng, C. H., Lim, H. N., Lim, Y. S., Chee, W. K., & Huang, N. M. (2014). Fabrication of flexible polypyrrole/graphene oxide/manganese oxide supercapacitor. *International Journal of Energy Research*, *39*: 344–355.
- Oh, J., Kozlov, M. E., Kim, B. G., Kim, H.-K., Baughman, R. H., & Hwang, Y. H. (2008). Preparation and electrochemical characterization of porous SWNT–PPy nanocomposite sheets for supercapacitor applications. *Synthetic Metals*, *158*: 638–641.

- Ong, L. K., Kurniawan, a., Suwandi, a. C., Lin, C. X., Zhao, X. S., & Ismadji, S. (2012). A facile and green preparation of durian shell-derived carbon electrodes for electrochemical double-layer capacitors. *Progress in Natural Science: Materials International*, 22: 624–630.
- Ozdemir, I., Şahin, M., Orhan, R., & Erdem, M. (2014). Preparation and characterization of activated carbon from grape stalk by zinc chloride activation. *Fuel Processing Technology*, 125: 200–206.
- Pan, H., Li, J., & Feng, Y. P. (2010). Carbon nanotubes for supercapacitor. *Nanoscale Research Letters*, 5: 654–668.
- Pandiselvi, K., & Thambidurai, S. (2014). Chitosan-ZnO/polyaniline ternary nanocomposite for high-performance supercapacitor. *Ionics*, 20: 551–561.
- Pang, S. C., Anderson, M. a, & Chapman, T. W. (2000). Novel electrode materials for thin-film ultracapacitors: Comparison of electrochemical properties of sol-gel-derived and electrodeposited manganese dioxide. *Journal of The Electrochemical Society*, 147: 444–450.
- Patil, D. S., Pawar, S. A., Devan, R. S., Gil, M., Ma, Y.-R., Hyeok, J., & Patil, P. S. (2013). Electrochemical supercapacitor electrode material based on polyacrylic acid/polypyrrole/silver composite. *Electrochimica Acta*, 105: 569–577.
- Patil, D. S., Shaikh, J. S., Pawar, S. A., Devan, R. S., Ma, Y. R., Moholkar, A. V., Kim, J. H., Kalubarme, R. S., Park, C. J., & Patil, P. S. (2012). Investigations on silver/polyaniline electrodes for electrochemical supercapacitors. *Physical Chemistry Chemical Physics : PCCP*, 14: 11886–95.
- Pawar, D. K., Shaikh, J. S., Pawar, B. S., Pawar, S. M., Patil, P. S., & Kolekar, S. S. (2012). Synthesis of hydrophilic nickel zinc ferrite thin films by chemical route for supercapacitor application. *Journal of Porous Materials*, 19: 649–655.
- Pusawale, S. N., Deshmukh, P. R., Gunjekar, J. L., & Lokhande, C. D. (2013). SnO₂-RuO₂ composite films by chemical deposition for supercapacitor application. *Materials Chemistry and Physics*, 139: 416–422.
- Qi, F., Wang, Y., Ma, T., Zhu, S., Zeng, W., Hu, X., Liu, Z., Huang, J., & Luo, Z. (2013). Electrical regulation of olfactory ensheathing cells using conductive polypyrrole/chitosan polymers. *Biomaterials*, 34: 1799–1809.
- Ra, E. J., Raymundo-Piñero, E., Lee, Y. H., & Béguin, F. (2009). High power supercapacitors using polyacrylonitrile-based carbon nanofiber paper. *Carbon*, 47: 2984–2992.
- Raicopol, M., Pruna, A., & Pilan, L. (2013). Supercapacitance of single-walled carbon nanotubes-polypyrrole composites. *Journal of Chemistry*, 2013: 367473.
- Ramya, R., Sivasubramanian, R., & Sangaranarayanan, M. V. (2013). Conducting polymers-based electrochemical supercapacitors—progress and prospects. *Electrochimica Acta*, 101: 109–129.

- Ren, B., Fan, M., Liu, Q., Wang, J., Song, D., & Bai, X. (2013). Hollow NiO nanofibers modified by citric acid and the performances as supercapacitor electrode. *Electrochimica Acta*, 92: 197–204.
- Ricketts, B. W., & Ton-That, C. (2000). Self-discharge of carbon-based supercapacitors with organic electrolytes. *Journal of Power Sources*, 89: 64–69.
- Ryu, K. S., Kim, K. M., Park, N.-G., Park, Y. J., & Chang, S. H. (2002). Symmetric redox supercapacitor with conducting polyaniline electrodes. *Journal of Power Sources*, 103: 305–309.
- Sadki, S., Schottland, P., Sabouraud, G., & Brodie, N. (2000). The mechanisms of pyrrole electropolymerization. *Chemical Society Reviews*, 29: 283–293.
- Sanpui, P., Murugadoss, a., Prasad, P. V. D., Ghosh, S. S., & Chattopadhyay, A. (2008). The antibacterial properties of a novel chitosan-Ag-nanoparticle composite. *International Journal of Food Microbiology*, 124: 142–146.
- Sawangphruk, M., Srimuk, P., Chiochan, P., Krittayavathananon, A., Luanwuthi, S., & Limtrakul, J. (2013). High-performance supercapacitor of manganese oxide/reduced graphene oxide nanocomposite coated on flexible carbon fiber paper. *Carbon*, 60: 109–116.
- Sharma, R. K., Karakoti, A., Seal, S., & Zhai, L. (2010). Multiwall carbon nanotube-poly(4-styrenesulfonic acid) supported polypyrrole/manganese oxide nanocomposites for high performance electrochemical electrodes. *Journal of Power Sources*, 195: 1256–1262.
- Sharma, R. K., Rastogi, a. C., & Desu, S. B. (2008a). Manganese oxide embedded polypyrrole nanocomposites for electrochemical supercapacitor. *Electrochimica Acta*, 53: 7690–7695.
- Sharma, R. K., Rastogi, A. C., & Desu, S. B. (2008b). Pulse polymerized polypyrrole electrodes for high energy density electrochemical supercapacitor. *Electrochemistry Communications*, 10: 268–272.
- Shen, J., Yang, C., Li, X., & Wang, G. (2013). High-performance asymmetric supercapacitor based on nanoarchitected polyaniline/graphene/carbon nanotube and activated graphene electrodes. *ACS Applied Materials and Interfaces*, 5: 8467–8476.
- Simon, P., & Gogotsi, Y. (2008). Materials for electrochemical capacitors. *Nature Materials*, 7: 845–854.
- Singh, A., Salmi, Z., Joshi, N., Jha, P., Decorse, P., Lecoq, H., Lau-Truong, S., Jouini, M., Aswal, D. K., & Chehimi, M. M. (2013). Electrochemical investigation of free-standing polypyrrole–silver nanocomposite films: a substrate free electrode material for supercapacitors. *RSC Advances*, 3: 24567–24575.
- Snook, G. A., Kao, P., & Best, A. S. (2011). Conducting-polymer-based supercapacitor devices and electrodes. *Journal of Power Sources*, 196: 1–12.

- Stoller, M. D., Park, S., Zhu, Y., An, J., & Ruoff, R. S. (2008). Graphene-based ultracapacitors. *Nano Letters*, 8: 3498–3502.
- Stoller, M. D., & Ruoff, R. S. (2010). Best practice methods for determining an electrode material's performance for ultracapacitors. *Energy & Environmental Science*, 3: 1294–1301.
- Su, A. D., Zhang, X., Rinaldi, A., Nguyen, S. T., Liu, H., Lei, Z., Lu, L., & Duong, H. M. (2013). Hierarchical porous nickel oxide–carbon nanotubes as advanced pseudocapacitor materials for supercapacitors. *Chemical Physics Letters*, 561-562: 68–73.
- Sudhakar, Y. N., & Selvakumar, M. (2012). Lithium perchlorate doped plasticized chitosan and starch blend as biodegradable polymer electrolyte for supercapacitors. *Electrochimica Acta*, 78: 398–405.
- Sun, F., Pang, X., & Zhitomirsky, I. (2009). Electrophoretic deposition of composite hydroxyapatite-chitosan-heparin coatings. *Journal of Materials Processing Technology*, 209: 1597–1606.
- Sun, G., Li, B., Ran, J., Shen, X., & Tong, H. (2015). Three-dimensional hierarchical porous carbon/graphene composites derived from graphene oxide-chitosan hydrogels for high performance supercapacitors. *Electrochimica Acta*, 171: 13–22.
- Sun, W., Tian, W., Zhang, Y., He, J., Mao, S., & Fang, L. (2012). Effect of novel stabilizers-cationic polymers on the particle size and physical stability of poorly soluble drug nanocrystals. *Nanomedicine: Nanotechnology, Biology, and Medicine*, 8: 460–467.
- Taguchi, A., Inoue, S., Akamaru, S., Hara, M., Watanabe, K., & Abe, T. (2006). Phase transition and electrochemical capacitance of mechanically treated manganese oxides. *Journal of Alloys and Compounds*, 414: 137–141.
- Tallman, D. E., Vang, C., Wallace, G. G., & Bierwagen, G. P. (2002). Direct Electrodeposition of Polypyrrole on Aluminum and Aluminum Alloy by Electron Transfer Mediation. *Journal of The Electrochemical Society*, 149: C173–C179.
- Toupin, M., Brousse, T., & Bélanger, D. (2004). Charge storage mechanism of MnO₂ electrode used in aqueous electrochemical capacitor. *Chemistry of Materials*, 16: 3184–3190.
- Twu, Y.-K., Chen, Y.-W., & Shih, C.-M. (2008). Preparation of silver nanoparticles using chitosan suspensions. *Powder Technology*, 185: 251–257.
- Vidhyadharan, B., Khayyriah, N., Zain, M., Misnon, I. I., Aziz, R. A., Ismail, J., Yusoff, M. M., & Jose, R. (2014). High performance supercapacitor electrodes from electrospun nickel oxide nanowires. *Journal of Alloys and Compounds*, 610: 143–150.
- Wang, G., Zhang, L., & Zhang, J. (2012). A review of electrode materials for electrochemical supercapacitors. *Chemical Society Reviews*, 41: 797–828.

- Wang, H., Peng, C., Peng, F., Yu, H., & Yang, J. (2011). Facile synthesis of MnO₂/CNT nanocomposite and its electrochemical performance for supercapacitors. *Materials Science and Engineering B*, 176: 1073–1078.
- Wang, J., Xu, Y., Zhu, J., & Ren, P. (2012). Electrochemical in situ polymerization of reduced graphene oxide/polypyrrole composite with high power density. *Journal of Power Sources*, 208: 138–143.
- Wang, J.-G., Yang, Y., Huang, Z., & Kang, F. (2014). MnO₂/polypyrrole nanotubular composites: reactive template synthesis, characterization and application as superior electrode materials for high-performance supercapacitors. *Electrochimica Acta*, 130: 642–649.
- Wang, J.-G., Yang, Y., Huang, Z.-H., & Kang, F. (2011). Coaxial carbon nanofibers/MnO₂ nanocomposites as freestanding electrodes for high-performance electrochemical capacitors. *Electrochimica Acta*, 56: 9240–9247.
- Wang, J.-G., Yang, Y., Huang, Z.-H., & Kang, F. (2012a). Incorporation of nanostructured manganese dioxide into carbon nanofibers and its electrochemical performance. *Materials Letters*, 72: 18–21.
- Wang, J.-G., Yang, Y., Huang, Z.-H., & Kang, F. (2012b). Rational synthesis of MnO₂/conducting polypyrrole@carbon nanofiber triaxial nano-cables for high-performance supercapacitors. *Journal of Materials Chemistry*, 22: 16943–16949.
- Wang, Y., Tao, S., & An, Y. (2012). Superwetting monolithic carbon with hierarchical structure as supercapacitor materials. *Microporous and Mesoporous Materials*, 163: 249–258.
- Wang, Y., & Zhitomirsky, I. (2011). Cathodic electrodeposition of Ag-doped manganese dioxide films for electrodes of electrochemical supercapacitors. *Materials Letters*, 65: 1759–1761.
- Wei, D., Sun, W., Qian, W., Ye, Y., & Ma, X. (2009). The synthesis of chitosan-based silver nanoparticles and their antibacterial activity. *Carbohydrate Research*, 344: 2375–2382.
- Wei, J., Xing, G., Gao, L., Suo, H., He, X., Zhao, C., Li, S., & Xing, S. (2013). Nickel foam based polypyrrole–Ag composite film: a new route toward stable electrodes for supercapacitors. *New Journal of Chemistry*, 37: 337–341.
- Wei, L., Sevilla, M., Fuertes, A. B., Mokaya, R., & Yushin, G. (2012). Polypyrrole-derived activated carbons for high-performance electrical double-layer capacitors with ionic liquid electrolyte. *Advanced Functional Materials*, 22: 827–834.
- Wei, W., Cui, X., Chen, W., & Ivey, D. G. (2011). Manganese oxide-based materials as electrochemical supercapacitor electrodes. *Chemical Society Reviews*, 40: 1697–1721.
- World Energy Outlook. (2014) Accessed on 5/10/2015, <http://www.iea.org/textbase/npsum/weo2014sum.pdf>

- Wu, X., Wen, T., Guo, H., Yang, S., Wang, X., & Xu, A. (2013). Biomass-derived sponge-like carbonaceous hydrogels and aerogels for supercapacitors. *ACS Nano*, 3589–3597.
- Wu, Y., Shen, Z., & Yu, T. (2014). Two-dimensional carbon: Fundamental properties, synthesis, characterization, and applications. Boca Raton, FL: Pan Stanford Publishing.
- Wysocka-Żołopa, M., Grądzka, E., Szymański, K., & Winkler, K. (2013). Electrodeposition of nickel, cobalt, and iron on polypyrrole films. *Thin Solid Films*, 548: 44–51.
- Xiao, J., Yang, S., Wan, L., Xiao, F., & Wang, S. (2014). Electrodeposition of manganese oxide nanosheets on a continuous three-dimensional nickel porous scaffold for high performance electrochemical capacitors. *Journal of Power Sources*, 245: 1027–1034.
- Yalçinkaya, S., Demetgül, C., Timur, M., & Çolak, N. (2010). Electrochemical synthesis and characterization of polypyrrole/chitosan composite on platinum electrode: Its electrochemical and thermal behaviors. *Carbohydrate Polymers*, 79: 908–913.
- Yamada, M., & Honma, I. (2005). Anhydrous proton conductive membrane consisting of chitosan. *Electrochimica Acta*, 50: 2837–2841.
- Yamagata, M., Soeda, K., Ikebe, S., Yamazaki, S., & Ishikawa, M. (2013). Chitosan-based gel electrolyte containing an ionic liquid for high-performance nonaqueous supercapacitors. *Electrochimica Acta*, 100: 275–280.
- Yan, J., Liu, J., Fan, Z., Wei, T., & Zhang, L. (2012). High-performance supercapacitor electrodes based on highly corrugated graphene sheets. *Carbon*, 50: 2179–2188.
- Yan, J., Wei, T., Fan, Z., Qian, W., Zhang, M., Shen, X., & Wei, F. (2010). Preparation of graphene nanosheet/carbon nanotube/polyaniline composite as electrode material for supercapacitors. *Journal of Power Sources*, 195: 3041–3045.
- Yan, J., Wei, T., Qiao, W., Fan, Z., Zhang, L., Li, T., & Zhao, Q. (2010). A high-performance carbon derived from polyaniline for supercapacitors. *Electrochemistry Communications*, 12: 1279–1282.
- Yang, X., Li, L., & Yan, F. (2010). Polypyrrole/silver composite nanotubes for gas sensors. *Sensors & Actuators B: Chemical*, 145: 495–500.
- Yao, W., Zhou, H., & Lu, Y. (2013a). Synthesis and property of novel MnO₂@polypyrrole coaxial nanotubes as electrode material for supercapacitors. *Journal of Power Sources*, 241: 359–366.
- Yao, W., Zhou, H., & Lu, Y. (2013b). Synthesis and property of novel MnO₂@polypyrrole coaxial nanotubes as electrode material for supercapacitors. *Journal of Power Sources*, 241: 359–366.

- Yen, H., Horng, Y., Hu, M., Yang, W., Wen, J.-R., Ganguly, A., Tai, Y., Chen, K.-H., & Chen, L.-C. (2014). Vertically aligned epitaxial graphene nanowalls with dominated nitrogen doping for superior supercapacitors. *Carbon*, 82: 124–134.
- Yin, H., Zhou, Y., Ma, Q., Ai, S., Chen, Q., & Zhu, L. (2010). Electrocatalytic oxidation behavior of guanosine at graphene, chitosan and Fe₃O₄ nanoparticles modified glassy carbon electrode and its determination. *Talanta*, 82: 1193–1199.
- Yoo, H., Min, M., Bak, S., Yoon, Y., & Lee, H. (2014). A low ion-transfer resistance and high volumetric supercapacitor using hydrophilic surface modified carbon electrodes. *Journal of Materials Chemistry A*, 2: 6663–6668.
- You, B., Wang, L., Li, N., & Zheng, C. (2014). Improving the Energy Storage Performance of Graphene through Insertion of Pristine CNTs and Ordered Mesoporous Carbon Coating. *ChemElectroChem*, 1: 772–778.
- Yu, C., Gou, L., Zhou, X., Bao, N., & Gu, H. (2011). Chitosan–Fe₃O₄ nanocomposite based electrochemical sensors for the determination of bisphenol A. *Electrochimica Acta*, 56: 9056–9063.
- Yu, G., Xie, X., Pan, L., Bao, Z., & Cui, Y. (2013). Hybrid nanostructured materials for high-performance electrochemical capacitors. *Nano Energy*, 2: 213–234.
- Zang, J., & Li, X. (2011). In situ synthesis of ultrafine β-MnO₂/polypyrrole nanorod composites for high-performance supercapacitors. *Journal of Materials Chemistry*, 21: 10965–10969.
- Zangmeister, R. A., Park, J. J., Rubloff, G. W., & Tarlov, M. J. (2006). Electrochemical study of chitosan films deposited from solution at reducing potentials. *Electrochimica Acta*, 51: 5324–5333.
- Zeng, X., Li, X., Xing, L., Liu, X., Luo, S., Wei, W., Kong, B., & Li, Y. (2009). Electrodeposition of chitosan–ionic liquid–glucose oxidase biocomposite onto nano-gold electrode for amperometric glucose sensing. *Biosensors and Bioelectronics*, 24: 2898–2903.
- Zhang, A., Xiao, Y., Lu, L., Wang, L., & Li, F. (2013). Polypyrrole/MnO₂ composites and their enhanced electrochemical capacitance. *Journal of Applied Polymer Science*, 128: 1327–1331.
- Zhang, D., Zhang, X., Chen, Y., Yu, P., Wang, C., & Ma, Y. (2011). Enhanced capacitance and rate capability of graphene/polypyrrole composite as electrode material for supercapacitors. *Journal of Power Sources*, 196: 5990–5996.
- Zhang, H., Cao, G., Wang, Z., Yang, Y., Shi, Z., & Gu, Z. (2008). Growth of manganese oxide nanoflowers on vertically-aligned carbon nanotube arrays for high-rate electrochemical capacitive energy storage. *Nano Letters*, 8: 2664–2668.
- Zhang, J., & Zhao, X. S. (2012). Conducting Polymers Directly Coated on Reduced Graphene Oxide Sheets as High-Performance Supercapacitor Electrodes. *The Journal of Physical Chemistry C*, 116: 5420–5426.

- Zhang, L. L., & Zhao, X. S. (2009). Carbon-based materials as supercapacitor electrodes. *Chemical Society Reviews*, 38: 2520–2531.
- Zhang, S., Li, Y., & Pan, N. (2012). Graphene based supercapacitor fabricated by vacuum filtration deposition. *Journal of Power Sources*, 206: 476–482.
- Zhang, S. W., & Chen, G. Z. (2009). Manganese oxide based materials for supercapacitors. *Energy Materials*, 3: 186–200.
- Zhang, W., Li, J., Du, X., & Zhang, Z. (2009). Porous manganese oxide synthesized through organic-electrolyte templates and their catalytic applications. *Materials Research Bulletin*, 44: 2072–2080.
- Zhang, X., Sun, X., Zhang, H., Zhang, D., & Ma, Y. (2013). Microwave-assisted reflux rapid synthesis of MnO₂ nanostructures and their application in supercapacitors. *Electrochimica Acta*, 87: 637–644.
- Zhang, Y., Feng, H., Wu, X., Wang, L., Zhang, A., Xia, T., Dong, H., Li, X., & Zhang, L. (2009). Progress of electrochemical capacitor electrode materials: A review. *International Journal of Hydrogen Energy*, 34: 4889–4899.
- Zhang, Z., & Mu, J. (2007). Effect of hydrothermal time, pH, and alkali on crystal phase and morphology of manganese oxides. *Journal of Dispersion Science and Technology*, 28: 793–796.
- Zhao, B., & Nan, Z. (2012). Formation of self-assembled nanofiber-like Ag@PPy core/shell structures induced by SDBS. *Materials Science and Engineering: C*, 32: 1971–1975.
- Zhao, H., Liu, F., Han, G., Liu, Z., Liu, B., Fu, D., Li, Y., & Li, M. (2014). Co-electrodeposition of MnO₂/graphene oxide coating on carbon paper from phosphate buffer and the capacitive properties. *Journal of Solid State Electrochemistry*, 18: 553–559.
- Zhi, J., Zhao, W., Liu, X., Chen, A., Liu, Z., & Huang, F. (2014). Highly Conductive Ordered Mesoporous Carbon Based Electrodes Decorated by 3D Graphene and 1D Silver Nanowire for Flexible Supercapacitor. *Advanced Functional Materials*, 24: 2013–2019.
- Zhi, M., Manivannan, A., Meng, F., & Wu, N. (2012). Highly conductive electrospun carbon nanofiber/MnO₂ coaxial nano-cables for high energy and power density supercapacitors. *Journal of Power Sources*, 208: 345–353.
- Zhou, C., Zhang, Y., Li, Y., & Liu, J. (2013). Construction of high-capacitance 3D CoO@polypyrrole nanowire array electrode for aqueous asymmetric supercapacitor. *Nano Letters*, 13: 2078–2085.

LIST OF PUBLICATIONS AND PAPERS PRESENTED

Publications

1. **Gan, J. K.,** Lim, Y. S., Huang, N. M., & Lim, H. N. (2015). Effect of pH on morphology and supercapacitive properties of manganese oxide/polypyrrole nanocomposite. *Applied Surface Science*, 357: 479-486.
2. **Gan, J. K.,** Lim, Y. S., Huang, N. M., & Lim, H. N. (2015). Hybrid silver nanoparticle/nanocluster-decorated polypyrrole for high-performance supercapacitors. *RSC Advances*, 5: 75442-75450.
3. **Gan, J. K.,** Lim, Y. S., Pandikumar A., Huang, N. M., & Lim, H. N. (2015). Graphene/polypyrrole-coated carbon nanofiber core-shell architecture electrode electrochemical capacitors. *RSC Advances*, 5: 12692-12699.

Paper presented in international conference:

1. **Gan, J. K.,** Lim, Y. S., Huang, N. M., & Lim, H. N. "Hybrid silver nanoparticle/nanocluster-decorated polypyrrole for high-performance supercapacitors." in *International Conference On Recent Advances In Materials And Chemical Sciences*, 14-15 December 2015, Department of Chemistry, Gandhigram Rural Institute, Dindigul District, Tamil Nadu, India. (**Poster presentation**).